Characterization of the Plasma Response to Injector Frequency in the HIT-SI3 Spheromak Experiment

James M. Penna

A dissertation
submitted in partial fulfillment of the
requirements for the degree of

Doctor of Philosophy

University of Washington

2021

Reading Committee:

Brian Nelson, Chair

Uri Shumlak

Chris Hansen

Program Authorized to Offer Degree:
Aeronautics and Astronautics

University of Washington

Abstract

Characterization of the Plasma Response to Injector Frequency
in the HIT-SI3 Spheromak Experiment

James M. Penna

Chair of the Supervisory Committee:
Brian Nelson
Department of Aeronautics and Astronautics

The Helicity Injected Torus - Steady Inductive 3 (HIT-SI3) was a spheromak experiment at the Univeristy of Washington HIT-SI laboratory that used three injectors running in AC to inject magnetic helicity into a copper flux conserver in the form of induced voltage and magnetic flux. This form of spheromak generation and sustainment, known as Steady Inductive Helicity Injection (SIHI), was used on a previous experiment known as HIT-SI (Helicity Injected Torus - Steady Inductive). This method holds promise as a means of sustaining a steady-state spheromak for long enough to generate fusion power, however the properties of SIHI-driven spheromaks are still not well characterized. In particular, studies of the previous experiment HIT-SI revealed the choice of injector frequency f_{inj} could heavily influence spheromak characteristics, and experimental evidence from HIT-SI3 discharges showed a similar dependence. In this work, studies on both experimentally measured data from HIT-SI3 and simulation data have been performed to definitively characterize the differences between spheromaks formed with different injector frequencies. Biorthogonal Decomposition was used as a tool to examine experimental data from HIT-SI3 and helped to distinguish important behavior, in particular the presence of $n = 2$ fluctuations not associated with the spheromak equilibrium or imposed by the injectors. Experimental data from the magnetic probe sets in HIT-SI3 was compared across different injector frequencies and used in the 2D

equilibrium fitting software PSI-Tri to reconstruct the magnetic field profile and estimate β. The 3D xMHD software NIMROD has been used to simulate HIT-SI and HIT-SI3 in past studies, and was used to simulate experimental HIT-SI3 shots at the injector frequency of 58.5 kHz by applying the injector waveform from the experiment as a boundary condition in the simulation. NIMROD was then used in a set of extended simulations at a variety of injector frequencies, including ones not used or used very little on HIT-SI3, to establish trends in calculated quantities such as injector impedance and β, the ratio of plasma pressure to magnetic field pressure and an important parameter for determining the potential power of a fusion reactor configuration. These trends are compared to the previous experiment, HIT-SI, in the hope of finding general behaviors that scale predictably with injector frequency and can be extended to future SIHI devices.

TABLE OF CONTENTS

LIST OF FIGURES

LIST OF TABLES

GLOSSARY

FLUX SURFACE: A surface of constant plasma pressure along which magnetic field lines lay parallel, obeying $B \cdot \nabla p = 0$. In a toroidal, magnetically-confined plasma described by MHD, the plasma can be thought of as forming a series of nested, closed toroidal flux surfaces.

HIT-SI: Helicity Injected Torus - Steady Inductive, a spheromak experiment at the University of Washington that employed two SIHI injectors as the means of spheromak formation and sustainment, followed by experiments HIT-SI3 and HIT-SIU.

INTERFEROMETER: A scientific instrument relying on the interference between a reference and measurement laser beam that is used to make line-averaged measurements as a plasma diagnostic.

MAGNETIC HELICITY: The degree of interlinkage between tubes of magnetic flux oriented in different directions, directly calculable from the integral of the dot product of magnetic potential and field: $K = \int_V \vec{A} \cdot \vec{B} \, \mathrm{d}^3 r$.

MAGNETOHYDRODYNAMICS: A single-fluid model for describing the behavior and evolution of magnetized, collisionless plasmas that uses equations of both fluid dynamics and electrodynamics.

MIRNOV COIL: A type of magnetic probe consisting of a coil through which magnetic fields pass, producing a voltage; the time-integrated voltage is proportional to the magnetic field by an area based on the coil factor.

SAFETY FACTOR: A parameter for helping determine the Ideal-MHD stability of a toroidal plasma, defined s the ratio of toroidal rotations over the number of poloidal rotations on a given poloidal flux surface and usually denoted by q. In a circular, toroidally symmetric 2D system, it can be defined using $q = \frac{d\Psi}{d\Phi}$.

SIHI: Steady Inductive Helicity Injection - method of helicity injection using AC voltage and flux coils, rather than DC pulsed coaxial electrodes used in other spheromaks.

SPHEROMAK: A simply-connected magnetized plasma topology characterized by minimization of external magnetic fields, without magnetic-field generating coils linking the center of the topology.

ACKNOWLEDGMENTS

The author wishes to express sincere appreciation and thanks to a number of people for making this work possible. First, thank you to the HIT-SI group for their years of education and support, in particular to Kyle Morgan who I can name as my second advisor and Chris Hansen, for his patience and attentiveness while stepping up to fill a role in my thesis committee. I also thank and appreciate the members of my committee, all of whom have substantially contributed to my education over the years. My special appreciation goes to my wonderful family for believing in me as I pursued this work: my mother Dianne, my brothers Jonathan, Joseph and Joshua, and my sisters Corrin, Ashley and Cameron. I also thank my mother's partner Thomas, for his aggressive encouragement. My thanks and love go to my own wonderful partner, Lisa Kong, for her support and encouragement as I pursued this work. Finally, thanks be to God, through whom all things are possible.

Chapter 1
INTRODUCTION

1.1 Background on Magnetic Confinement Fusion

The quest for controlled fusion power is an active area of research, with many schemes having been proposed to bring the nuclear reaction powering the sun down to earth. Fusion occurs in the sun's core via the gravitational pressure of the outer mass, which cannot possibly be replicated on earth. Instead plasma, the fourth state of matter consisting of collectively-behaving positive ions and electrons, is contained at extremely high temperature for sufficient periods of time for the ions to fuse together. This can be done via inertial (inertial confinement fusion, or ICF) methods, in which powerful lasers, particle beams or strong electrostatic fields compress fusion fuel together in a target until a sustained fusion reaction occurs, or magnetic confinement fusion (MCF), in which the individually charged plasma particles are confined to (for the most part) magnetic field lines in a closed geometry.[34] It is MCF which shall be the focus of this work; in particular the scope of this thesis will be limited to one concept in MCF known as the spheromak.

1.2 Introduction to Spheromaks

The spheromak is a toroidal plasma confinement concept which is geometrically classified as being simply connected; that is to say, no structures link the plasma torus and the structure is therefore topologically spherical[3]. While being technically "spherical" in geometry, the magnetic fields are still toroidally shaped, having a "toroidal" dimension going along the long dimension of the torus, and a "poloidal" dimension winding around the short dimension. This is more clearly illustrated in Figure 1.1.

An illustration of the spheromak configuration itself can be seen in Figure 1.2. The

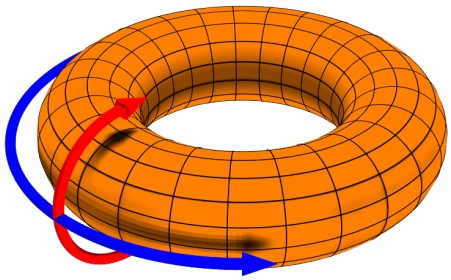

Figure 1.1: Diagram in 3D of a torus highlighting the toroidal (longway) and poloidal (shortways) directions.

plasma is confined by magnetic fields which are generated by plasma currents in the toroidal and poloidal direction. Helical magnetic fields form closed surfaces of constant current and particle pressure, known as flux surfaces. Spheromaks hold significant promise as a concept for magnetic confinement fusion; spheromak plasmas generate their own toroidal fields and do not require toroidal field coils that link the center of the torus necessitating significant shielding to protect them from high temperatures, radiation, and large magnetic fields.The magnetic field geometry of a spheromak enables the construction of relatively simple electricity-generating power plants, as the flux conserver and confinement vessel can be easily enclosed by a blanket without contending with topologically-linked center structures.[26] In addition, the performance of spheromaks may be high compared to other fusion systems, with electron temperatures of hundreds of eV demonstrated in laboratory spheromaks due to Ohmic heating[24]. Ohmic heating allows for spheromaks to heat to their β-limit (the natural limit of confined thermal energy) without the need for auxiliary heating[19]. These factors make spheromaks an attractive choice for economical fusion power, however spheromaks until recently have not been driven in the steady state regimes needed for fusion. Without external

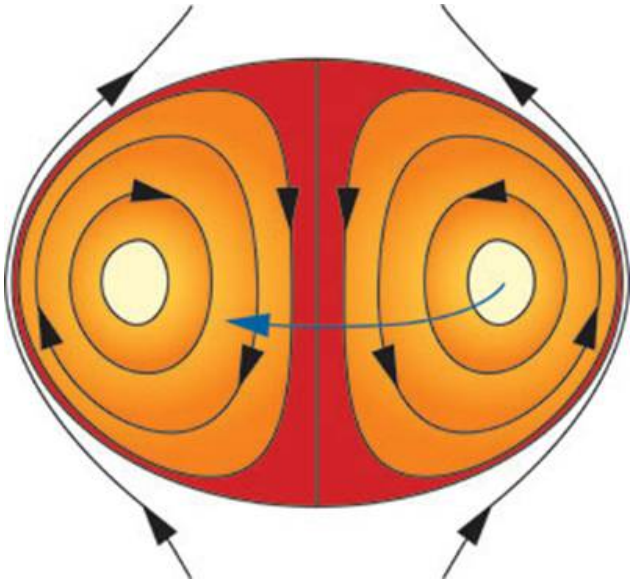

Figure 1.2: Cartoon of a spheromak showing pure toroidal field in the center, pure poloidal/vertical fields at the edge, and nested flux surfaces. Original source: http://www.llnl.gov/str/September05/Hill.html

influence, a spheromak in isolation will begin decaying due to the resistivity in the plasma, necessitating a source of external current drive. Outside of standard methods such as RF current drive or neutral beam injection, current drive in spheromaks can be accomplished via non-axisymmetric magnetic activity transfering injected poloidal flux and current to toroidal. While this method of current drive sustains magnetic helicity, discussed in-depth more in the next section, this form of plasma activity tends to break flux surfaces and can degrade confinement before the plasma can heat to fusion-relevant temperatures. Finding a method to sustain the toroidal current in a spheromak until ignition, without significantly impacting confinement, has been one of the main objectives of spheromak research.

1.3 Helicity Injection and Spheromak formation

The physics of spheromak formation are explained by the conjecture known as the Taylor minimum energy principle, which states that a magnetized plasma will "relax" by dissipating magnetic field energy while conserving the quantity known as magnetic helicity[46] [48]. The relaxation will lower the magnetic energy to the minimum state for a given set of boundaries, which is known as the Taylor state. Magnetic helicity is a measure of the linkage between magnetic flux and can be calculated using the integral:

$$K = \int_V \vec{A} \cdot \vec{B} \mathrm{d}^3 r \tag{1.1}$$

where $\vec{A}$ is the magnetic vector potential and $\vec{B}$ is the magnetic field. A useful assumption for simplicity is that the flux in the system is contained in two flux tubes which are simply linked with each other and not any flux tubes connected to a flux-conserving boundary, as displayed in Figure 1.3. Under this assumption, the helicity can be approximated as:

$$K = 2\psi_1\psi_2 \tag{1.2}$$

where ψ_1 is flux in one direction and ψ_2 is flux in another, "linking" from crossing. Though this is technically an approximation for isolated flux tubes, it allows other concepts to be more simply illustrated and have some applicability to driven spheromaks.

Subject to the constraint that the helicity K be constant, the magnetic energy $W = \int \frac{B^2}{2\mu_o} dV$ can be minimized using a Lagrange multiplier. The Lagrange function L then becomes

$$L = W - \lambda H = \int \frac{(\nabla \times \vec{A})^2}{2\mu_o} dV - \lambda \int \vec{A} \cdot (\nabla \times \vec{A}) dV = 0 \tag{1.3}$$

where $\vec{A}$ is the magnetic vector potential and λ is the Lagrange multiplier constraining the minimization of energy to helicity. Solving the minimization problem yields a relation between the magnetic field of the Taylor minimum energy state and the current density in Ampere's Law:

Figure 1.3: A pair of isolated but linked vacuum flux tubes for which the equation 1.2 is applicable.

$$\nabla \times \vec{B} = \mu_o \vec{j} = \lambda \vec{B} \tag{1.4}$$

where the Lagrange multiplier λ is the eigenvalue of Equation 1.4 above, the spatial variation of the magnetic field and is defined as $\lambda = \frac{\mu_o J}{B}$. The above equation implies that in the minimum energy conserving helicity, lowest eigenvalue (MECH) state, the current is completely parallel with the magnetic field, meaning there are no $\vec{J} \times \vec{B}$ forces and no pressure gradient. In this state λ is uniform and takes on a single value. In an ideal spheromak configuration, the poloidal magnetic fields (generated by toroidal plasma current I_{tor}) have an O-point defining the magnetic axis (the center of the minor radial cross-section) and are maximized at the wall. Conversely, the toroidal magnetic field profile has an O-point at the center of the torus defining the geometric axis. The magnetic fields are entirely self-generated by plasma currents following the same trend as the magnetic field magnitude; the maximum toroidal current is at the poloidal O-point, whereas the maximum poloidal current is at the spheromak outer edge and geometric axis. For stability, the "safety factor" q, the ratio of toroidal field line winding to poloidal field line winding, is below 1 everywhere in a spheromak. This enables the magnetic field to avoid the major instabilities at $q = 1$, as well

as instabilities at major toroidal modes $n = 2, n = 3...$ if the q-profile is properly tailored. [3]

Helicity decays resistively like the magnetic field, and in order to sustain a spheromak, a source of helicity to inject against resistive decay must be used. Taking the derivative of Equation 1.1 and application of Maxwell's equations and resistivity give:

$$\dot{K} = K_{inj} - K_{decay}$$
$$\dot{K} = 2V\psi - \frac{K}{\tau_K}$$

where $\dot{K}$ is the rate of helicity change, V and ψ are voltage and magnetic flux injected into the system, respectively, and τ_K is the rate of decay of helicity. Steady-state implies the two terms balance. Experimentally, spheromaks are formed via an apparatus for injecting voltage along magnetic flux paths into a flux conserver. The voltage source can be electrostatic, as in the case of the Marshall gun and kinked Z-pinch formation methods, or it can be inductive, as in the case of the flux core spheromak and HIT-SI3's Steady Inductive Helicity Injection, which will be explained further below.[40] Spheromak experiments like SSPX (pictured in Figure 1.4) typically operated in a "pulsed" mode in which the electrodes and magnetic stuffing coil were fired, discharging plasma into a flux conserver where a spheromak formed and then heated as it decayed; the decay is due to the lack of helicity injection term to balance the resistive decay term in the equation above. SSPX did operate in "refluxing" mode with periodic pulses from the Marshall gun after the initial formation pulse to sustain the spheromak against helicity decay and drive the spheromak toroidal current. The result of these experiments was less that promising, as the flux surfaces of the spheromak were broken during current drive periods and the energy confinement was dramatically decreased.[38] Sustaining a toroidal current in a spheromak, while steadily injecting helicity, is therefore the most important problem in creating a spheromak-based fusion reactor. The HIT-SI, and later HIT-SI3, experiments were constructed specifically to address this problem.

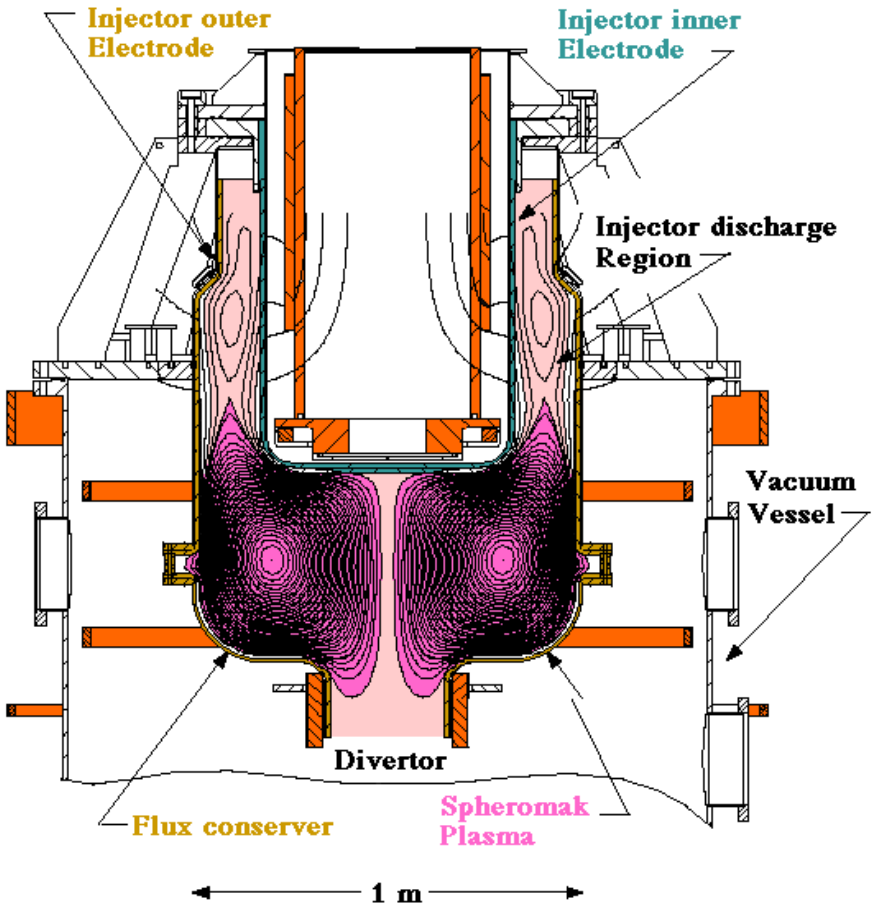

Figure 1.4: Schematic of the SSPX (Sustained Spheromak Physics eXperiment) device at LLNL. The spheromak is produced by a set of coaxial electrodes and a solenoid "stuffing" coil to facilitate flux injection. From [24]

1.4 Overview of the HIT-SI3 Experiment

The HIT-SI3 (Helicity Injected Torus - Steady Inductive 3) experiment is an upgrade of the HIT-SI spheromak current drive experiment[30] that employs a method of current drive known as Imposed Dynamo Current Drive (IDCD)[31]. A 3-D rendering of the experiment's flux conserver can be seen in Figure 1.5. HIT-SI3 differs significantly from other major spheromak experiments in that the spheromak is produced and driven inductively rather than electrostatically, and with steady-state AC sources rather than a pulsed DC source. Three sets of inductive transformers and flux coils are mounted on "plasma injectors" that inject helicity against resistive decay and drive current through IDCD. These helicity injectors use two sets of coils to generate magnetic helicity; the white set seen in Figure 1.6 produces magnetic flux along the length of the injector, whereas the multi-colored set is an air core transformer that inductively drives a loop voltage along the path of the injector. The waveforms for the voltage and flux from the three injectors, summed together, give the total helicity injection:

$$\dot{K} = 2V\psi[\sin^2(\omega_{inj}t) + \sin^2(\omega_{inj}t + \phi_1) + \sin^2(\omega_{inj}t + \phi_2)] \tag{1.5}$$

If the relative time phases between injectors, ϕ_1 and ϕ_2, equal $\frac{2\pi}{3}$ and $\frac{4\pi}{3}$ radians, or $\frac{\pi}{3}$ and $\frac{2\pi}{3}$ radians, the sin terms in the helicity injection will sum to a constant:

$$\dot{K} = 2V\psi(\sin^2(\omega_{inj}t) + \sin^2(\omega_{inj}t + \frac{2\pi}{3}) + \sin^2(\omega_{inj}t + \frac{4\pi}{3}) = \frac{3}{2}V\psi \tag{1.6}$$

therefore constantly injecting helicity over time. Using this method of Steady Inductive Helicity Injection (SIHI), spheromaks have been formed with toroidal currents of greater than 90 kA, while other spheromaks have reached current amplification (defined $\frac{I_{tor}}{I_{inj}}$) records of over 3.5. The AC frequency of the helicity injectors is variable and several values between 5 kHz and 70 kHz have been run experimentally. Analysis on data from the magnetic probe sets on the machine show that there are substantial differences in the magnetic field Fourier spectra between shots with different injector frequencies and different injector phasings ϕ_1

Figure 1.5: A rendering of the HIT-SI3 experiment flux conserver with three half-toroidal ducts for the helicity injectors (coils for injecting voltage and flux not pictured here).

and ϕ_2 [13]. In particular, there seems to be a sharp bifurcation between spheromaks formed at "low" ($f_{inj} < 40kHz$) frequencies and those formed at "high" ($f_{inj} > 40$ kHz) frequencies.

HIT-SI3 has several diagnostic sets which provide information on the magnetic fields, current centroid position, density, and temperature of the spheromak plasma. Discussion here will be limited to the most pertinent diagnostic sets for the proposed research: the surface magnetic probe set, the Internal Magnetic Probe, and the Far-Infrared (FIR) interferometer[12].

1.4.1 Surface Magnetic Probes

HIT-SI3 is equipped with a set of 96 poloidal and toroidal magnetic field Mirnov coil probes mounted within the flux conserver of the experiment and used to measure the edge magnetic fields of the spheromak. These probes are divided into 4 poloidal arrays of 16 probes each at the toroidal angles 0, 45, 180, and 225 degrees. There are two additional arrays of 16 probes arranged toroidally at the top and bottom of the diagnostic gap. Each probe consists of two wound coils. The sets and probes themselves can be seen in Figure 1.7. Measurements

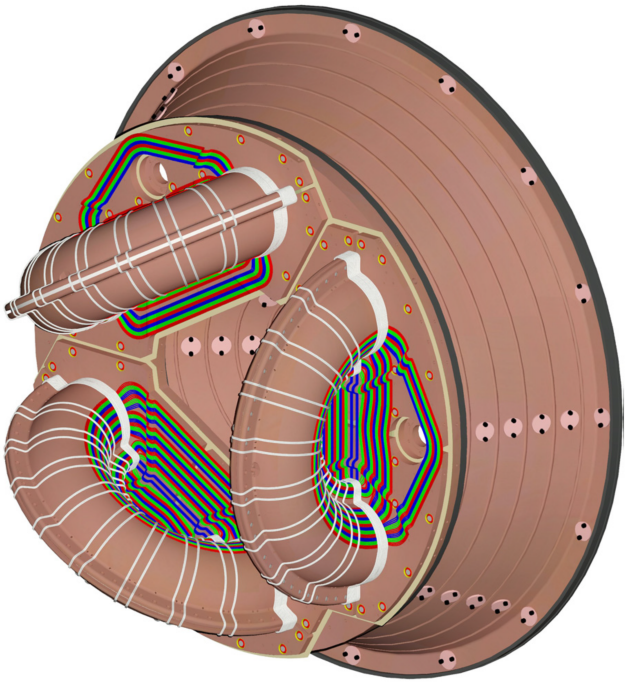

Figure 1.6: Rendering of the HIT-SI3 helicity injectors showing the flux coils (white) and the voltage coils (rainbow). Together these two coils inject helicity $K_{inj} = 2V_o\psi_o$ individually in AC but collectively in DC with proper phases between the injector waveforms.

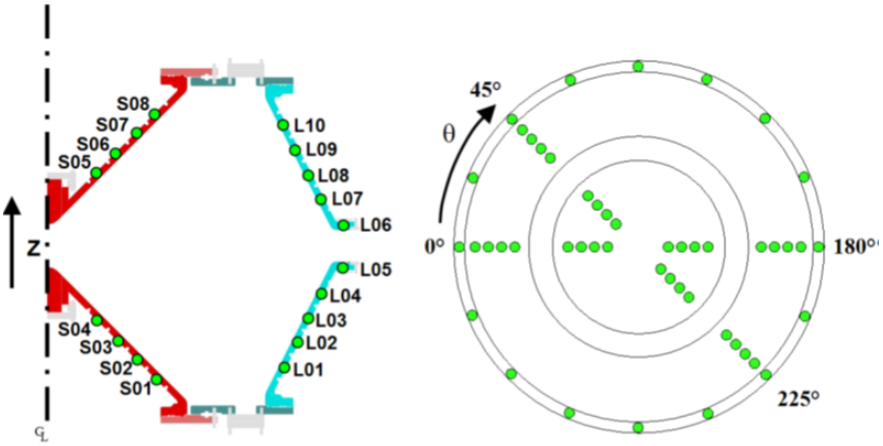

Figure 1.7: Left: Diagram of position of one of the four poloidal arrays of 16 surface probes in the HIT-SI3 flux conserver. Right: Diagram showing the toroidal spacing of the two sets of 16 "gap" surface probes that allow resolution of toroidal modes.

of the fields by the arrays allows the magnetic field data to be decomposed easily via Fourier analysis to characterize the nature of instabilities and fluctuations. In addition, the poloidal surface probes can be used as points along an Amperian loop to calculate the toroidal current and by using a weighted average of the measurements, calculate the rough position of the toroidal current centroid.[49] Data from these probes constitutes the majority of the data set in the Biorthogonal Decomposition analysis elaborated on later.

1.4.2 Internal Magnetic Probe (IMP)

The Internal Magnetic Probe (IMP), or trident probe, consist of three arrays of 17 radial, poloidal, and toroidal magnetic field loop probes.[47] Changing magnetic fields in any of these directions induce a voltage in the loop, and time integrating the voltage signal yields a term proportional to the magnetic field. These are mounted on a fork-like array as the name suggests, with a top, middle, and bottom prong, each of which are shielded with a boron-nitride sheath. These features can all be seen in Figure 1.8, a photograph of the probe

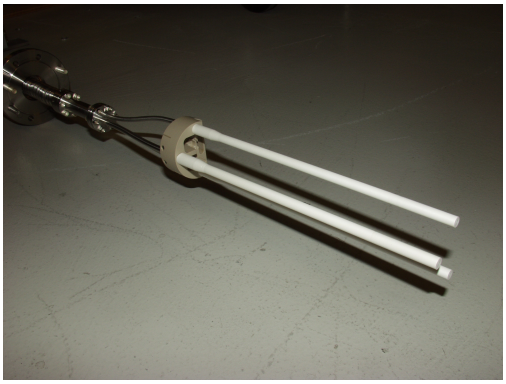

Figure 1.8: A photograph of the Internal Magnetic Probe (IMP), removed from the machine. The three prongs of the probe are clearly displayed.

removed from the machine.The probe is vertically positioned almost at the midplane of the machine, 1.1 cm below the $z = 0$ point of the midplane, and can be inserted for a depth of 23 cm and is 20.3 cm long. This allows probe access from close to the magnetic axis to almost the radial edge of the plasma when fully inserted. While a powerful diagnostic, the downside of the IMP is the tendency for it to disrupt/disturb the plasma around it and heavily affect measurements.

1.4.3 Far Infrared (FIR) Interferometer

An interferometer is a device that splits and then rejoins a beam of light, resulting in a change in the phase of the light due to constructive and destructive interference. Interferometers are exploited in plasma physics to measure electron densities, as there is a simple relation between the electron density and the phase shift of light passing through a plasma:

$$\Delta\theta_l = \frac{-\omega}{2cn_c}\int_0^l n_e dl \tag{1.7}$$

where l is the length of the laser beam chord passing through the plasma, ω is the frequency of the laser, n_c is the cutoff density, and n_e is the desired electron density. As this measurement is line integrated, the local density and density distribution cannot be resolved,

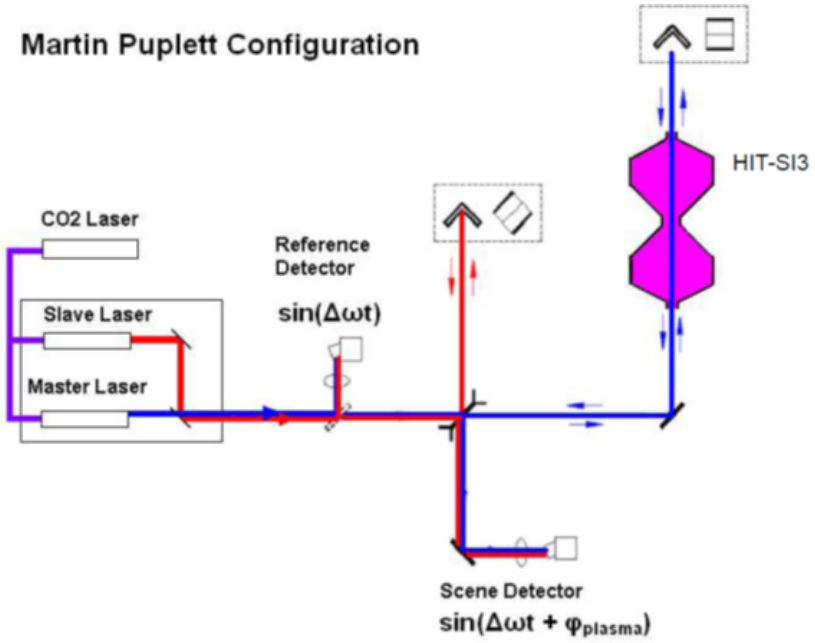

Figure 1.9: Diagram of the HIT-SI3 FIR interferometer showing dual laser set up to create a beat frequency, which resolves ambiguity of phase (ϕ vs $\phi + 2\pi$) as the laser passes through the plasma and creates a phase shift ϕ_{plasma}. This phase shift ϕ_{plasma} contains information about the plasma density. Courtesy of [20].

making it an average quantity.

The FIR on HIT-SI3, seen in Figure 1.9, is a heterodyne CO_2 laser with a master and slave configuration producing a modulation of 3-4 MHz around a THz (1060 nm) frequency. The heterodyne beat allows for less ambiguous phase measurements. The chord of the laser is directed through the diagnostic gap and just above the midplane at a radius of 35 cm, allowing for line-averaged density measurements close to the position of the magnetic axis. As a density diagnostic, the FIR provides a rough idea of the evolution of the core electron density, which provides indirectly information about quantities such as β and pressure. It also has the benefit of being one of the more straightforward diagnostics to compare between experimental shots and simulations.

1.5 Dynamo Theory and Current Drive in HIT-SI3

The electromagnetic activity of a sustained spheromak resemble in many aspects the working of a dynamo; after formation the current in a spheromak is DC, and any driving forces therefore must be capable of driving steady state current. However, this would be in violation of Cowling's theorem: a dynamo with steady state current resisting Ohmic dissipation cannot be driven by axisymmetric forces. The original proof is available in Cowling's work [8], however the relevant implication can be expressed neatly using the resistive Hall MHD Ohm's law. The electromagnetic forces driving a DC current in one direction in a dynamo (in this case the toroidal direction of a spheromak) are:

$$\vec{E_{tor}} = -\vec{v} \times \vec{B} + \eta \vec{j_{tor}} + \frac{\vec{j_{tor}} \times \vec{B}}{ne} \tag{1.8}$$

where $\vec{E_{tor}}$ is the electric field driving a current in the toroidal direction, $\eta \vec{j_{tor}}$ is the current dissipating resistively, and ne is the charge density. Taking the assumption of axisymmetry and steady-state sustainment, the electric field must vanish, meaning

$$\langle \vec{v} \times \vec{B} \rangle_{tor} = \eta \vec{j} + \langle \frac{\vec{j} \times \vec{B}}{ne} \rangle \tag{1.9}$$

However, we observe that only poloidal terms in the magnetic field can contribute to the non-dissipative terms due to the cross product. In the configuration described, current must be driven along the toroidal axis. Spheromaks drive current (in a completely relaxed state) along magnetic field lines, which are closed after formation and (ideally) during sustainment, so along the magnetic axis the field is purely toroidal and B_{pol} goes to 0. This means any sustained dynamo must not be axisymmetric, for if it was, the cross-product terms would go to zero and nothing would balance decay. The solution lies in the fact that, while sustainment in a Taylor-state like configuration necessitates axisymmetry ($n = 0$), the dynamics driving the current and relaxation do not preclude asymmetric processes; in fact, in order to convert poloidal into toroidal flux and drive a spheromak, non-axisymmetric processes are necessary.[32] [11] The way in which these processes occur inform the physics

of the system's sustainment. In coaxial helicity injectors, these asymmetries are the result of instabilities that occur naturally during the formation process, but in the case of HIT-SI and HIT-SI3 the non-axisymmetric modes are imposed by injectors and the mode spectrum or power injection rate can changed by changing the phasing or frequency.

1.6 Dissertation Outline

The next chapter of this thesis will first cover a description of the NIMROD code used to perform MHD simulations of SIHI devices, including how simulations of HIT-SI3 experimental shots are carried out. Chapter 3 will present magnetic field data from HIT-SI3 low and high frequency shots will be presented in order to demonstrate the differences in mode structure between the two operating frequency regimes. In particular, the presence of intermittent non-axisymmetric $n = 2$ modes will be examined, and equilibrium reconstructions from the experimental magnetic field data are performed to determine if the plasma-generated activity has an effect on the overall equilibrium. Initial NIMROD simulations of high-frequency experimental shot 180816020 and comparison to experimental data will also be presented with brief analysis of internal profiles $(\vec{B}, \lambda, P)$. Chapter 4 will present the results of extending both constant pressure and time-evolved pressure ("finite-β") simulations across a range of injector frequencies, including and beyond those used in experimental operation; these results will also include the first detailed two-temperature simulation results for HIT-SI3, demonstrating the effect that separating electron and ion heating have in improving fidelity. The final chapter of this thesis will compare results presented throughout this work and draw general conclusions about the nature of HIT-SI3's behavior as well as discussion about the differences found between computational models (one vs two-temperature evolution). A short discussion of proposed future research will follow the conclusions, including projects for extending the research performed on HIT-SI3 as well as suggestions for research projects on the newest experiment HIT-SIU.

Chapter 2

NUMERICAL TOOLS FOR MODELING, ANALYSIS AND SIMULATION

In order to understand the possible internal dynamics active in SIHI current drive and validate the physics hypotheses tested on HIT-SI3, the NIMROD (Non-Ideal Magnetohydrodynamics with Rotation and Open Discussion) code is used to simulate the experiment[21]. NIMROD is a 3D finite element, non-ideal, non-linear magnetohydrodynamic code which is used to simulate SIHI in a domain modeled after the flux conserver of HIT-SI3. Simulations offer greater choice in range and resolution of parameters such as the injector frequency, power and λ, the ratio of current to magnetic field:

$$\lambda = \frac{\mu_o J}{B} \tag{2.1}$$

Simulations in NIMROD can also vary other parameters that cannot be varied in the experiment, such as number of injectors, the Fourier spectrum of the injected magnetic fields, and even the flux conserver shape and size. The accessibility of NIMROD data, compared to the diagnostics available in a laboratory plasma experiment, allows detailed information about plasma parameters such as $\vec{B}$ and T to be sampled and visualized with much greater ease. The end goal of these simulations is to develop the physics model of spheromak formation and sustainment using SIHI, which can be used in the design and operation of higher performance experiments.

2.1 xMHD Simulations in NIMROD

NIMROD is a finite-element code that solves the equations of extended MHD in a 3D axisymmetric domain. The full extended model used is presented in the equations below:

$$\frac{\partial n}{\partial t} + \vec{\nabla} \cdot (n\vec{V}) = 0$$
$$\rho[\frac{\partial \vec{V}}{\partial t} + (\vec{V} \cdot \vec{\nabla})\vec{V}] = \vec{J} \times \vec{B} - \vec{\nabla} p - \vec{\nabla} \cdot \Pi$$
$$\frac{\partial \vec{B}}{\partial t} = -\vec{\nabla} \times (-\vec{V} \times \vec{B} + \eta \vec{J} + \frac{\vec{J} \times \vec{B} - \vec{\nabla} p_e}{ne} + (f_{me})\frac{m_e \partial \vec{J}}{ne^2 \partial t})$$
$$\frac{n_e}{\gamma - 1}(\frac{\partial T}{\partial t} + \vec{V} \cdot \vec{\nabla} T) = -p(\vec{\nabla} \cdot \vec{V}) + \Pi : \vec{\nabla}\vec{V} - \vec{\nabla} \cdot \vec{q} + \eta J^2$$

NIMROD has been used to model many fusion experiments, due to the ease of using it to model axisymmetric devices such as tokamaks and reverse-field pinches, and has seen extensive development in order to properly model plasmas across the wide parameter space covered by extended MHD. NIMROD models for HIT-SI and HIT-SI3 were first developed by Izzo[39] and later improved by Akcay[1]. The MHD Ohm's law currently employed in NIMROD includes the Hall term as well as the resistive and dynamic terms, as theoretical analysis [32] [11] has shown these terms contribute significantly to the current drive in HIT-SI3. Use of this MHD model has been validated by comparions of key metrics between NIMROD simulations of HIT-SI and HIT-SI3 and experimental measurements, such as toroidal current evolution, magnetic field energy, and phasing of magnetic field oscillations, as well as in the xMHD code PSI-Tet using the same MHD model.[15] [25] [1] [17]

NIMROD simulations of HIT-SI3 can be run in either a zero-β mode or a finite-β mode. In zero-β, the pressure is assumed to be uniform and constant and the equations for temperature and density are not evolved. While an incomplete model, running in zero-β gives a sense of the what the magnetic dynamics of the system would be if the background pressure remained constant. These solutions can be compared to the finite-β solutions to better understand what effects are being driven by changes in pressure, density and temperature, rather than just the evolution of magnetic field and current.

An implicit scheme is used in order to perform the time advance of the equations (from t_{i-1} to t_i), with the solution fields $\vec{B}, \vec{V}, n, T$ (or T_e, T_i) being represented as a vector of weights and the governing equations for the time advance represented as a matrix that is usually pre-conditioned to optimize the solve time. As with most finite-element codes, the spatial domain is broken up into a set of mesh elements geometrically approximating the HIT-SI3 flux conserver's cross-section. This grid is displayed in Figure 2.1. The equations above are discretized and the solution variables solved for along the vertices of the mesh, with a polynomial function approximating the solutions between main grid nodes (the order of which is set by the NIMROD variable *poly_d*). The mesh, however, is only constructed in 2D along the RZ cross-section of the domain, as NIMROD discretizes the toroidal direction (ϕ in the usual cylindrical R, ϕ, Z coordinate system) using a Fourier decomposition - the physical data in the toroidal direction is Fourier transformed to create an effective number of toroidal slices based on the number of modes the user chooses to simulate (specified in the code using the input variable l_{phi}).

NIMROD simulations can be performed in finite-β mode using either the single MHD temperature variable ($T = T_i = T_e$) or using a split-temperature advance to separately evolve T_e and T_i. In this temperature advance model, it is assumed that Ohmic heating is only applied to the electrons, and that viscous heating is only applied to the ions. This modifies the temperature equations to become:

$$\frac{n_i}{\gamma - 1}(\frac{\partial T_i}{\partial t} + \vec{V_i} \cdot \vec{\nabla} T_i) = -p_i(\vec{\nabla} \cdot \vec{V_i}) + \Pi : \vec{\nabla}\vec{V_i} - \vec{\nabla} \cdot \vec{q_i} - Q_{ie}$$
$$\frac{n_e}{\gamma - 1}(\frac{\partial T_e}{\partial t} + \vec{V_e} \cdot \vec{\nabla} T_e) = -p_e(\vec{\nabla} \cdot \vec{V_e}) - \vec{\nabla} \cdot \vec{q_e} + \eta J^2 - Q_{ei}$$

where the species velocity is expressed as:

$$\vec{V_i} = \vec{V} + \frac{\vec{J}\frac{Zm_e}{m_i}}{n_e e \frac{Zm_e}{m_i} + 1}$$
$$\vec{V_e} = \vec{V} - \frac{\vec{J}}{n_e e \frac{Zm_e}{m_i}}$$

Additionally, a Bragrinskii thermal conduction model for ion-ion and electron-electron

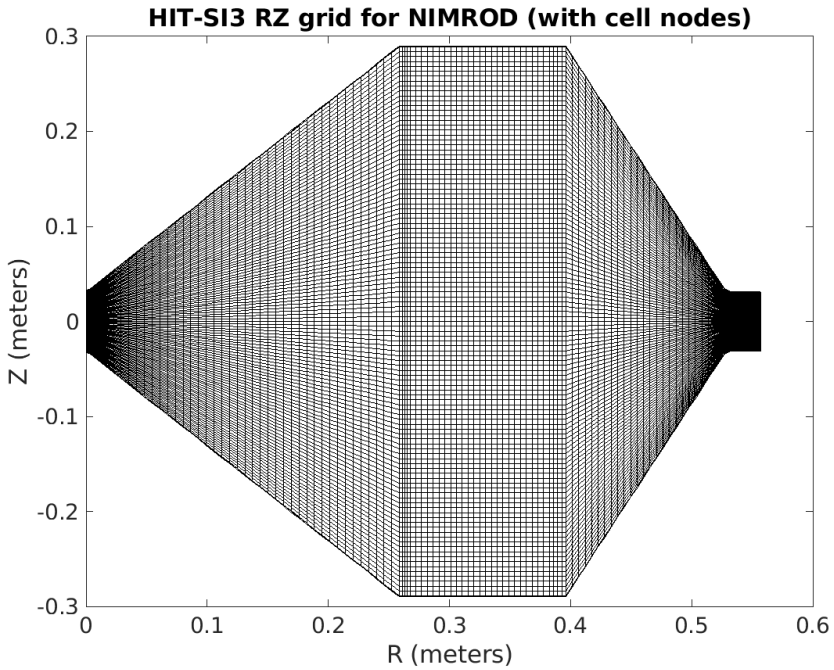

Figure 2.1: Grid used to compose the RZ domain in NIMROD simulations of HIT-SI3. Typical resolutions use anywhere from 100-200 nodal points in either direction, with grid used in this simulation the above having a 121 $\times$ 121 nodal point resolution.

conduction as an option for modelling thermal transport in NIMROD[43] [6]. In both the single and two temperature NIMROD simulations, the heat flux vector was formulated usinf the Braginskii model:

$$\vec{q_s} = (k_{\parallel,s}\hat{b}\hat{b} + k_{\perp,s}(I - \hat{b}\hat{b})) \cdot \vec{\nabla} T_s \tag{2.2}$$

where $k_\parallel$ is the parallel thermal conduction coefficient and $k_\perp$ is the perpendicular thermal conduction coefficient, and the diad tensor $\hat{b}\hat{b}$ is formed using the unit vector of the magnetic field $\hat{b} = \frac{\vec{B}}{|B|}$. The coefficients $k_{\parallel,s}, k_{\perp,s}$ are defined using the Braginskii formulation:

$$k_{\parallel,s} = \frac{\gamma_{0,s} T_s \tau_s}{m_s \delta_{0,s}}$$
$$k_{\perp,s} = \frac{(\gamma_{0,s} + \gamma_{1,s}(\Omega_s \tau_s)^2) T_s \tau_s}{m_s \Delta_s}$$

For a particular species (electron or ion) s, where Ω_s is the cyclotron frequency of the species, τ_s the thermalization time, and $\Delta_s = (\Omega_s \tau_s)^4 + \delta_{1,s}\Delta_s = (\Omega_s \tau_s)^2 + \delta_{0,s}$. In the case of single temperature advance simulations, the largest conduction coefficients in each direction are assumed in order to yield a conservative thermal conduction scenario; electron thermal conduction in the parallel direction, and ion in the perpendicular direction. The values of $\delta_{0,s}, \delta_{1,s}, \gamma_{0,s}\gamma_{1,s}$ used in previous models [1] [42] have been used in the simulations of HIT-SI3 presented in this work and can be seen in Table 1 in Chapter 3.

To numerically stabilize the Hall term solution early on in the simulation, the Grad-Shafranov[36] [44] equation is solved in the simulation domain:

$$\frac{\partial^2 \psi}{\partial r^2} - \frac{1}{r}\frac{\partial \psi}{\partial r} + \frac{\partial^2 \psi}{\partial z^2} + F\frac{d\psi}{dF} = -r^2 \frac{dP}{d\psi} \tag{2.3}$$

The term $-r^2 \frac{dP}{d\psi} = 0$ is set to reflect the constant pressure equilibrium used. The solution is generated using an auxiliary package to NIMROD called NIMEQ, and the equilibrium based on the resulting flux function is written to a binary "dump file" that can be read as an initial condition for NIMROD. Prior simulations have shown that this seed does not affect the equilibrium which is formed, for example the direction of toroidal current. NIMROD

simulations then step through the MHD equations in time, evolving the equilibrium under the influence of the magnetic perturbations applied from the injectors; how these perturbations are applied is discussed in the next section.

2.2 Boundary conditions and simulating experimental shots

2.2.1 Description of the boundary conditions

NIMROD nominally employs the perfect conductor boundary condition ($B_{norm} = 0$ and $E_{tan} = 0$), however HIT-SI3 also features an insulating wall of alumina coating sprayed onto the walls of the flux conserver to protect against voltage arcs. This is simulated in NIMROD using a highly-resistive one millimeter edge layer located around the boundary of the grid. [1] This edge layer has a programmable resistivity that is a large ($\times 1000$) multiple of the resistivity at the plasma edge, both of which are NIMROD input parameters. Another modification to the boundary conditions must be made to accommodate HIT-SI3's helicity injection; NIMROD's spectral decomposition in the toroidal dimension places a constraint of axisymmetry on grid geometries. The injectors on HIT-SI3 are non-axisymmetric and cannot be included in the mesh geometry used for the finite element calculation. Rather than directly advancing the fields in the injectors to solve for the perturbations applied within the flux conserver, the boundary conditions at the toroidal locations of the injectors are modified to apply the perturbation fields. Taking the time derivative of Equation 1.1 gives the condition for "injecting" helicity into a volume

$$\dot{K} = 2 \int \vec{E} \cdot \vec{B} \, \mathrm{dV} \tag{2.4}$$

The voltages and flux needed for sustaining helicity against resistive decay can therefore be applied using electric and magnetic fields. In place of a physical injector "mouth" opening into the volume like in the experiment, an area (roughly) equivalent to the injector mouth area is set with electric and magnetic fields simulating the injection of helicity rather than the normal perfectly conducting boundary conditions. The fields themselves are produced by

solving for the Grad-Shafranov equilibrium fields (using MATLAB code written originally by G. Marklin) within the injector volume and then decomposing the fields into a Fourier series. This allows the fields to be easily integrated into NIMROD's toroidal spectral decomposition, with the toroidal angle ϕ as the spectral variable for N modes (for further details see [1]):

$$B(r,z,\phi) = B_0 + \sum_{n=1}^{N} B_n(r,z)e^{in\phi} + B_n^*(r,z)e^{-in\phi}$$

$$E(r,z,\phi) = E_0 + \sum_{n=1}^{N} E_n(r,z)e^{in\phi} + E_n^*(r,z)e^{-in\phi} + \frac{\partial B_{norm}}{\partial t}$$

To simulate HIT-SI3, fields are applied at six toroidal locations using spacing of $\frac{\pi}{8}$; this can be visualized in Figure 2.2. Code has been introduced by K. Morgan [42] to create boundary conditions for arbitrary numbers of injectors at arbitrary toroidal locations on the top, bottom, and outer midplane of axisymmetric flux conservers. These injectors have allowed exploration of proposed configurations for future SIHI devices, as well as theoretical studies on the effects of different mode structures than the ones we can apply experimentally using the HIT-SI3 injectors.

2.2.2 Simulating experimental shots

Experimental shots can be simulated in NIMROD for physics validation against the experiment using data from experimental shots. Injector waveforms of the magnetic flux ψ, the voltage V and current I are saved for each shot during nominal operations of HIT-SI3. These waveforms are not pure oscillatory functions however, as the circuits of the machine need time to physically ramp up the magntiude of the voltage and current, as well as adjust the waveform phase to maintain the relative phasing of the injector. In order to accurately simulate experimental shots, the magnitude and phase ramp functions of each injector must be captured in the NIMROD boundary conditions. A script written by K. Morgan reads in the experimental injector signals and fits the data points for the experimental phase and amplitude to linear functions with the form:

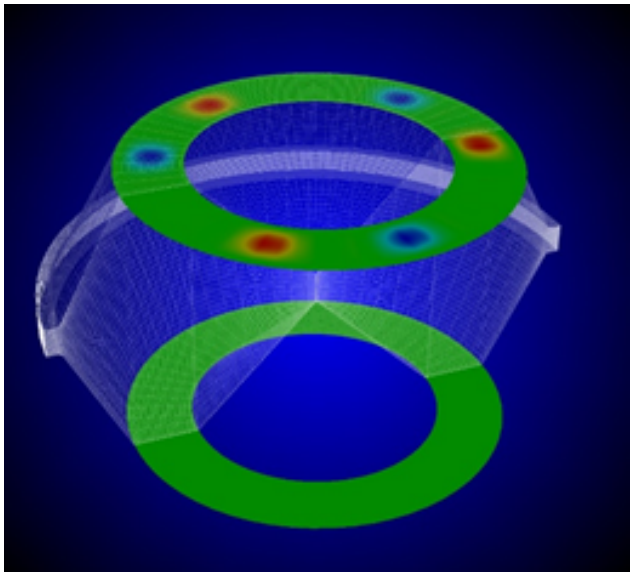

Figure 2.2: Heat map of the normal magnetic field for helicity injection on the top of the simulation domain, where red is highest magnitude positive field and blue is highest magnitude negative field, as seen using the visualization software VISIT.

$$A(t) = A_o + A_c t$$

$$\phi(t) = \phi_o + \phi_c t$$

where A_o, ϕ_o are the initial amplitudes and phase guesses, and A_c, ϕ_c are the linear coefficients multiplied against the timestep. The total injector waveform is constructed as a piecewise-linear function across time as the injector ramps us. The total waveform for the injector quantity becomes: $f(t) = A(t)\sin(\omega_{inj}t + \phi(t))$. The coefficient $A(t)$ and phase $\phi(t)$ are put into a text file output by the script, and used as an input file for NIMROD and used in the waveform ramp functions for the $\vec{E}$ and $\vec{B}$ boundary conditions, which in turn produce currents and fluxes similar to those applied in the experiment. Despite a linear fit seeming unsophisticated, it yields a fairly accurate waveform when compared to experimental injector data as can be seen in the examples in Figure 2.3. A full example of one of these waveform files can be found in Appendix A.

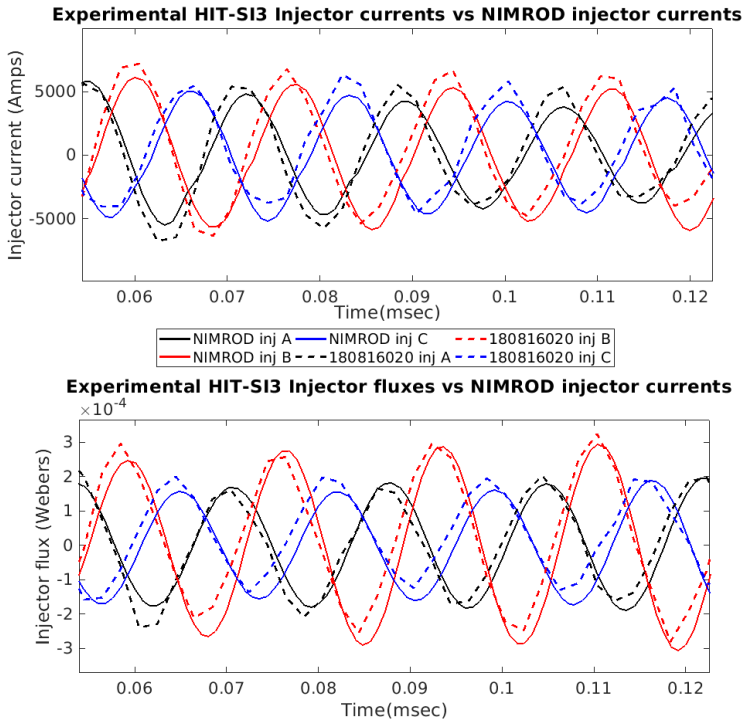

Figure 2.3: Experimental injector currents (top) and fluxes (bottom) with waveforms from NIMROD simulations of that experimental shot. The flux waveform has a better fit compared to the current, as the experiment often has overshoots not well captured by analytical functions.

2.3 Biorthogonal Decomposition as a Validation and Comparison tool

Descriptions of the magnetic structure of HIT-SI3, and magnetic fusion experiments in general, rely on defining the relative magnitudes and orientations of different components of the fields. The most complete description would be the magnitude of the $\vec{B}$-field in each axial direction at every spatial point, and while this is achievable in finite element simulations, it would be untenable in the physical experiment. Thus, field measurements from the relatively small number of spatial locations where there are magnetic probes are usually decomposed into components using some well known basis. One decomposition commonly used is the Fourier transform, which uses a series of sine and cosine functions to approximate more complex functions; each individual component in the series is known as a "mode." Fourier analysis has yielded great results in plasma physics in general, as toroidal devices have an axis of symmmetry which can be easily represented in a Fourier-transformed domain. The strong presence of single Fourier modes signals plasma behavior that deviates from this axis of symmetry and has been found to correspond with ideal MHD instabilities[35]. Fourier analysis also provides convenient comparison to simulations as the finite output data can be decomposed; it is advantageous for NIMROD in particular as the algorithm decomposes the solution fields spectrally for increased solving speed, and natively outputs the volumetric energy fractions of each Fourier component of the field.

Fourier transformation does not always unambiguously render the structure of magnetic fields however, especially in in devices HIT-SI3 with more complex geometry. The three helicity injectors apply a spectrum of magnetic Fourier modes that interact with the spheromak equilibrium non-linearly, and distinguishing plasma-generated instability from injector-generated activity in magnetic field measurements is has proved challenging using Fourier analysis alone. In order to signify the presence of a particular Fourier mode, an additional decomposition method is used that is capable of differentiating the equilibrium, injectors, and instabilities.

Biorthogonal Decomposition (BD) is a mathematical analysis technique that decomposes

a set of data A_{ij} into two orthogonal sets of basis vectors, $u_i \in U$ and $v_j \in V$ such that

$$\langle u_i, v_j \rangle = \delta_{ij} \tag{2.5}$$

for

$$A_{ij} = \sum u_i \otimes v_j \tag{2.6}$$

While there are conceivably other matrix decomposition choices, Biorthogonal Decomposition most commonly refers to Singular Value Decomposition (SVD), which is a matrix decomposition similar in nature to eigenvalue decomposition[41]. The action a matrix A has on a unitary basis vector $v_j \in V$ can mapped to the scaling of a set of vectors $u_i \in U$ by a set of "singular values" $\sigma_i \in \Sigma$, analogous to eigenvalues. If the matrix multiplication operation below is true

$$AV = U\Sigma \tag{2.7}$$

then this implies, as V is unitary,

$$A = U\Sigma V^* \tag{2.8}$$

In practice, the data matrix A is a matrix of magnetic probe measurement readings B, with each row being the signal from one of the surface probes, IMP probe loops, or injector current readings over time.[14] For n magnetic readings and m timesteps, such a matrix would be:

$$B = \begin{bmatrix} B_1(t_1) & B_1(t_2) & \dots & B_1(t_m) \\ B_2(t_1) & B_2(t_2) & \dots & B_2(t_m) \\ \vdots & \vdots & \ddots & \vdots \\ B_n(t_1) & B_n(t_2) & \dots & B_n(t_m) \end{bmatrix}$$

When this matrix is decomposed using singular value decomposition, the result is a matrix of empirical modes U that roughly correlate to the spatial variance of the fields ("topos"), a set of modes V that correlate to the temporal variation ("chronos"), and a set of singular values σ_n that can be interpreted as how heavily each empirical mode $B(x_i, t_j)_k = \sigma_k U_k(x_j) V_k(t_j)$ is weighted in the overall data set. The full decomposition into topos, weights and chronos is:

$$B = \begin{bmatrix} U_1(x_1) & U_1(x_2) & \dots & U_1(x_n) \\ U_2(x_1) & U_2(x_2) & \dots & U_2(x_n) \\ \vdots & \vdots & \ddots & \vdots \\ U_n(x_1) & U_n(x_2) & \dots & U_n(x_n) \end{bmatrix} \begin{bmatrix} \sigma_1 & 0 & \dots & 0 \\ 0 & \sigma_2 & \dots & 0 \\ \vdots & \vdots & \ddots & \vdots \\ 0 & \dots & \sigma_n & 0 \end{bmatrix} \begin{bmatrix} V_1(t_1) & V_1(t_2) & \dots & V_1(t_m) \\ V_2(t_1) & V_2(t_2) & \dots & V_2(t_m) \\ \vdots & \vdots & \ddots & \vdots \\ V_m(t_1) & V_m(t_2) & \dots & V_m(t_m) \end{bmatrix}$$

The matrix of weights Σ has columns of zeros inserted to the right of the principal value containing columns, as the number of probes is always smaller than the number of time steps.

BD (SVD) analysis offers several advantages over Fourier analysis when examining experimental data from HIT-SI3. The first is the ability to isolate features that cannot easily be resolved by the limited toroidal probe set in the experiment - as mentioned above the toroidal set has probes at 16 individual locations, allowing resolution of mode numbers only up to $n = 7$. Another advantage that isolate modes in the BD basis can be composed of several modes in Fourier space or another basis. The fields of the helicity injectors appear in a majority ($n = 1$ and odd harmonics, $n = 2$ and even harmonics) of the Fourier modes that can be resolved by the surface probes, however the same injector fields can be represented in only two distinct modes using BD. The BD anaylsis currently employed ranks the injectors as the second and third most powerful empirical modes by the magnitude of their singular values $\sigma_{k=2}$ and $\sigma_{k=3}$, after the spheromak equilibrium. However, if the singular values for those injector modes were set to zero and the data matrix reconstructed, the resulting set would have no injector activity remaining. This allows the injector fields to be "subtracted" from the overall magnetic field.

$$\sigma_{k=2,3} = 0$$

$$B_{injector} = B(i,t)_{k=2,3} = \sigma_{k=2,3} U(i,j)_{k=2,3} V(i,j)_k = 0$$

This then isolates the fields associated with the equilibrium, i.e. the spheromak, and with instabilities, which often occur with the same toroidal mode numbers that are imposed by the injectors ($n = 1$ ideal kink, $n = 2$ pressure driven kink). The equilibrium can be represented by a single BD mode itself, which is usually the strongest single mode if the injector fields are weighted appropriately. The equilibrium can be subtracted as well, leaving only the fields of plasma-generated instabilities when the data matrices are reconstructed.

Though powerful, BD analysis is still limited by diagnostic resolution when comparing NIMROD to experiment. To begin with, the location of the toroidal probe set is suboptimal; on the physical experiment, they are at the edge of the spheromak volume and wedged in between two conducting planes which cause significant error fields. Their corresponding locations in the simulation grid are in a poorly constructed area of the geometry which can distort the signals from simulations. Aside from these errors, the subtraction is sensitive to the weights chosen for the injector and equilibrium fields, and which empirical modes belong to which object can be ambiguous if the weight is not carefully chosen; in BD analysis of HIT-SI3, the injector current data is weighted using the constant $\mu_o = 4\pi \times 10^{-7} \frac{H}{m}$ to scale the currents, which are recorded, to the strength of magnetic fields. Regardless of these errors and possibilities for errors, the bulk signals from the probes themselves are only the fields at the probe locations, not the whole of the spheromak. The only probes inside of the plasma are the IMP and the Diametric Internal Probe (DIP); practically speaking, the DIP is rarely used due to the significant perturbative effect the probe has on the spheromak. As a result, the magnetic field data predominately reflects the outside of the spheromak and the resulting modes are based on what are essentially edge fields. With so little internal field data, comparisons of the BD subtracted modes between simulation and experiment on their own are not sufficient as they can have similar external structure with differing internal conditions. Despite these drawbacks, Biorthogonal Decomposition still proves to be

a valuable tool for analysis and validation as will be seen in the next section.

2.4 PSI-Tri Equilibrium Fitting Software

The PSI-Tri code is a 2D finite element code written by C. Hansen used to solve for the axisymmetric MHD equilibria on the domain[37] [16]. An unstructured triangular grid is used to discretize the domain and solution fields defined using a Lagrange basis set. Meshes can be imported from either the T3D or CUBIT mesh generation programs, which provides support for parameterizing geometry for sensitivity studies and common definitions for 3D models in PSI-Tet. The PSI-Tri code specifically solves the Grad-Shafranov equation in the cylindrically-approximated toroidal coordinate system (r, ϕ, z). The flux function $F(\psi)$ is a function of the poloidal flux ψ, and in this convention the magnetic field can be re-written in terms of the flux function:

$$B = \nabla\psi \times \nabla\phi + F(\psi)\,\nabla\phi \tag{2.9}$$

This abstraction of the magnetic field facilitates the adjustment of profiles for reconstructing experimental equilibria. Similar to previous reconstruction codes such as EFIT, the coefficients of this profile can be adjusted to minimize the difference between experimental data and equilibrium solutions. This allows "reconstructed" equilibria to be generated based on magnetic field measurements from the Internal Magnetic Probe and the surface Mirnov probe array. Using the solution to the flux function $F(\psi)$ as well as the derived pressure profile $P(\psi)$. The pressure profile is especially useful in finding important quantities that are hard to measure in experiment such as $< \beta >$. The caveat to using this sofware is the fact that is returns a static 2D equilibrium, when HIT-SI3 is a 3D and dynamic system. It is unclear how well at any given time HIT-SI3 can be approximated by a 2D system, but this software has been used to gain insight on past experiment HIT-SI's behavior.[13] In the next Chapter, PSI-Tri will be used to solve for "reconstructed" equilibria from HIT-SI3 at low and high injector frequencies in an attempt to characterize usual observed behavior from the surface probes.

Chapter 3

ANALYSIS OF $N = 2$ MODE FOUND IN HIT-SI3

An important feature for any spheromak-based reactor is the ability to avoid major instabilities, which can disrrupt magnetic fields and cause loss of confinement. Two major classes of instabilities important to spheromak physics include current-driven instabilities (due to excessive imbalances in current causing distorted magnetic fields) or pressure-driven (due to imbalances in the plasma pressure against magnetic field pressure). These instabilities manifest themselves in magnetic field measurements as fluctuations in the non-axisymmetric Fourier components, i.e. increases in the magnitude of major mode components such as $n = 1$, $n = 2$, and so on. The Biorthogonal Decomposition (BD) mode subtraction analysis described in previous Chapters was applied to shots taken at an injector frequency of 58.5 kHz and has identified $n = 2$ fields not imposed by the injectors or part of the spheromak equilibrium. This "plasma-generated" activity could be indicative of an instability forming in the spheromak and have prompted further investigation. This Chapter will begin with an overview of the identified $n = 2$ activity with experimental data presented from HIT-SI3 magnetic and density diagnostics that indicate the detected activity is affecting the entire spheromak. Analysis of equilibrium reconstructions from during periods of increased $n = 2$ using the PSI-Tri Grad-Shafranov equilibrium solver will also be presented and discussed. Finally, this Chapter will review a study done in the xMHD software NIMROD that replicated the current and flux waveforms of the 58.5 kHz shot 180816020, which, despite not exactly capturing the experimental behavior, provides a numerical model that allows insight into mechanisms that could be driving the activity.

3.1 Identification of n=2 Instabilities Associated with Density and Current Fluctuations

Previous research performed on HIT-SI indicated that the spheromaks sustained by SIHI were stable to the $n = 1$ instability, by using the BD subtraction technique discussed in the previous Chapter to show the $n = 1$ energy measured by the surface probes was largely imposed by the injectors. Investigation of HIT-SI3 magnetic field data has shown a similar stability to $n = 1$, but also revealed intermittent increases in the plasma-generated $n = 2$. This section will review the data taken from HIT-SI3 experimental shots and present evidence of the $n = 2$ activity based on edge-field Mirnov probe measurements, as well as evidence that this $n = 2$ activity is occurring alongside internal changes in magnetic field profile and density.

3.1.1 Background: $n = 2$ instability in spheromaks

As previously mentioned, some major instabilities in spheromaks can be classified as current-driven, if the instability originates from a plasma-fluid displacement that generate currents which create an unstable magnetic field, or pressure-driven, if displacements change the plasma pressure in such a way that it forces magnetic fields into undesirable configurations (e.g. interchange instability). The first major instability encountered in spheromak analysis is the $n = 1$ kink, a large asymmetric instability whch can cause the spheromak to tilt if the flux conserver is too prolate in shape. In configurations stable to the $n = 1$ instability such as a decaying, undriven sperhomak in an oblate flux conserver, the next major instability is the $n = 2$ kink instability, which stretches the spheromak into an oblate shape. This is a major instability in spheromaks that results from from current-driven activity peaking the current (and λ) profiles at the magnetic axis, pinching the spheromak into an oblate shape. A sketch of this can be seen in Figure 3.1. In decaying spheromaks this mode is often triggered when the plasma currents cause Ohmic heating, increasing plasma temperature and decreasing the plasma resistance, which has a dependence $\eta\, T^{-3/2}$. The Ohmic heating occurs

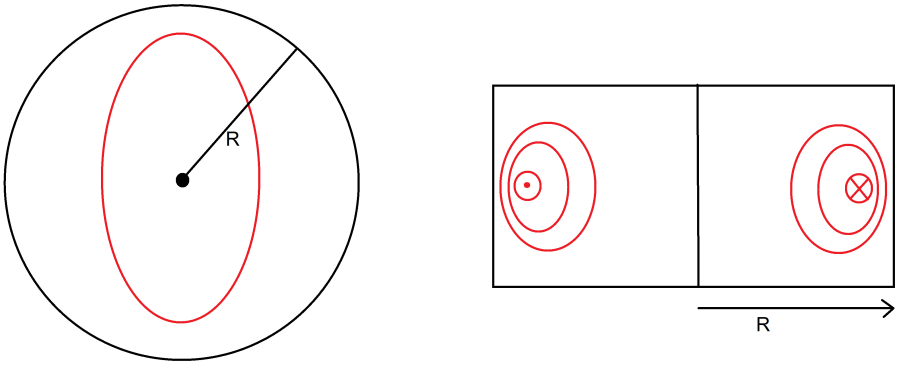

Figure 3.1: A cartoon sketch of the $n = 2$ instability that highlights the distortion in the toroidal direction as viewed from the top-down (left), and the flux surface configuration resulting in the imbalanced forces causing the instability (right).

more strongly in the center of the spheromak than the edge, with this decreased resistance causing the current to peak on the magnetic axis and causing the scenario described above. In particular, the unstable $q = \frac{1}{2}$ value is accessed when the current on the magnetic axis becomes peaks and the q-profile of the spheromak decreases from a region of stability.

This instability may also be triggered from excess pressure that causes instabilities such as interchanges. The presence of a magnetic shear gradient between flux surfaces provides a stabilizing effect against pressure-driven instabilities such as interchange. Bellan provides a (relatively) light analysis for a spheromak that gives a stability criterion on β for the pressure-driven $n = 1$ mode (Bellan Equation 6.81)[3]:

$$\frac{1}{12r^2}\psi_{axis}^3(\frac{q'}{q})^2 - 2\kappa\frac{\mu_o|\nabla P|}{B_\phi^2}\psi_{axis} > 0 \tag{3.1}$$

This criterion provides a stable set of q-values for a given plasma pressure, and can be

thought to set a β limit on a spheromak before the pressure drives it into an unstable region of q. A stability criterion for the q-profile was rigorously derived by Mercier for arbitrary toroidal and poloidal mode numbers n and m, but analytic definition of this criterion is difficult in the spheromak geometry[18]. Numerical anaylsis of ideal MHD models of the spheromak have been useful in further defining the stability requirements, such as those performed by Jardin et. al [29]. Stability analysis was performed on a series of spheromak configurations using numerical stability codes, and it was found that in addition to the Mercier-imposed β limit, internal pressure-driven $n = 2$ modes would develop in high β spheromaks that were within a region of stability according to Mercier. The stability limits to these modes are each labeled in Figure 3.2.

An experimental example of an intermittent pressure-driven mode was detected in SSPX discharges presented by Woodruff et al.[28] A toroidal $n = 2$ mode was observed initially during the spheromak decay, and after a "sustainment" pulse is triggered the dominant toroidal mode becomes $n = 4$, which combined with an $m = 2$ poloidal magnetic field shape created an unstable $q = \frac{1}{2}$ surface. While the spheromak was heating during these periods, the density values were observed to plummet, and the overall pressure remained the same, suggesting a pressure limit. Calculations for the Mercier-stable pressure were performed and plotted against the experimentally-measured pressure, seen in Figure 3.3 taken from Woodruff et al.[28] The calculations very closely tracked the experiment data, suggesting to the experimental team that the SSPX spheromak was encountering a Mercier-imposed pressure limit during these heating and instability periods. Overall, experimental presence of the $n = 2$ can indicate intermittent instabilities or other interesting activity (for instance, pressure fluctuations causing pressure to approach a β limit), and the next sections will focus on the detection and analysis of this toroidal mode in HIT-SI3 experimental discharges.

3.1.2 Presence of persistent n=2 instabilities in HIT-SI3 shots

The plasma response to imposed perturbations on HIT-SI3 was first investigated using the BD subtraction technique described above by Hossack.[10] The first observation drawn

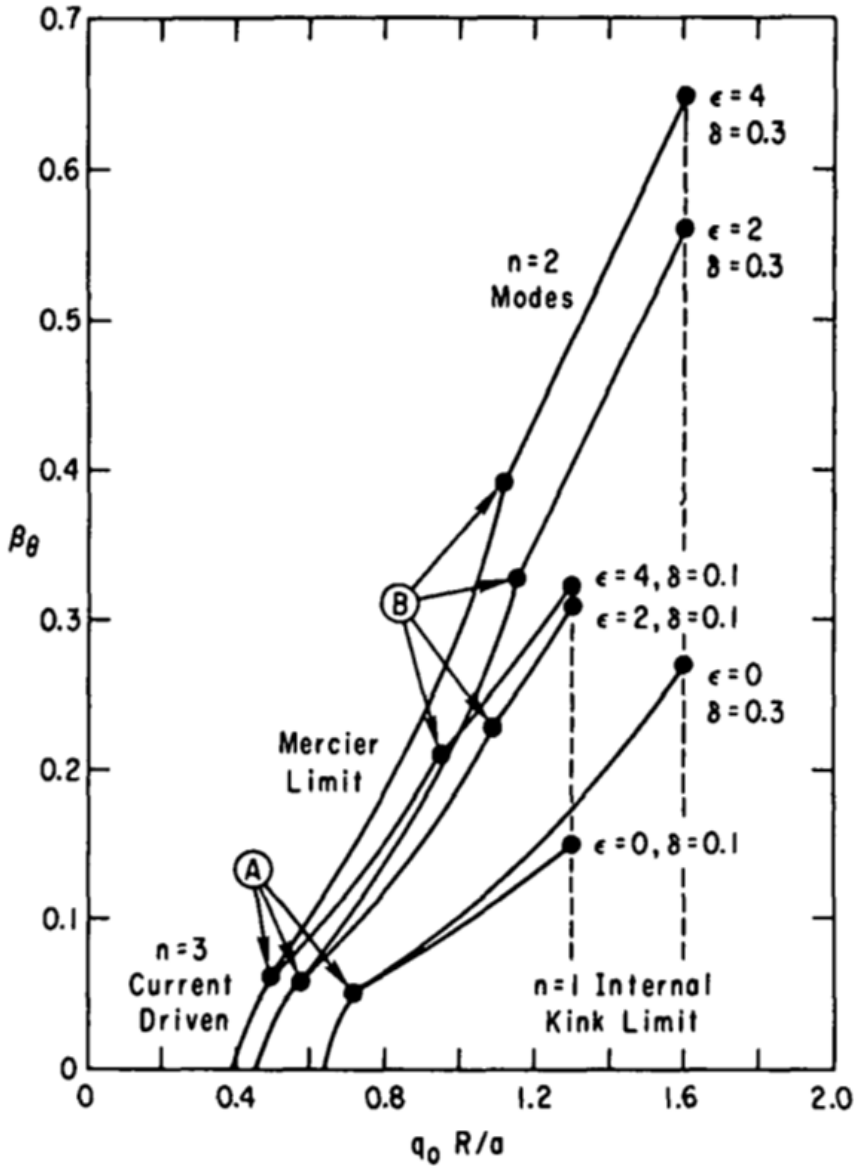

Figure 3.2: A plot taken from [29] charting the β calculated for various values of q_oR/a that are generated from spheromak equilibria with different shaping parameters.

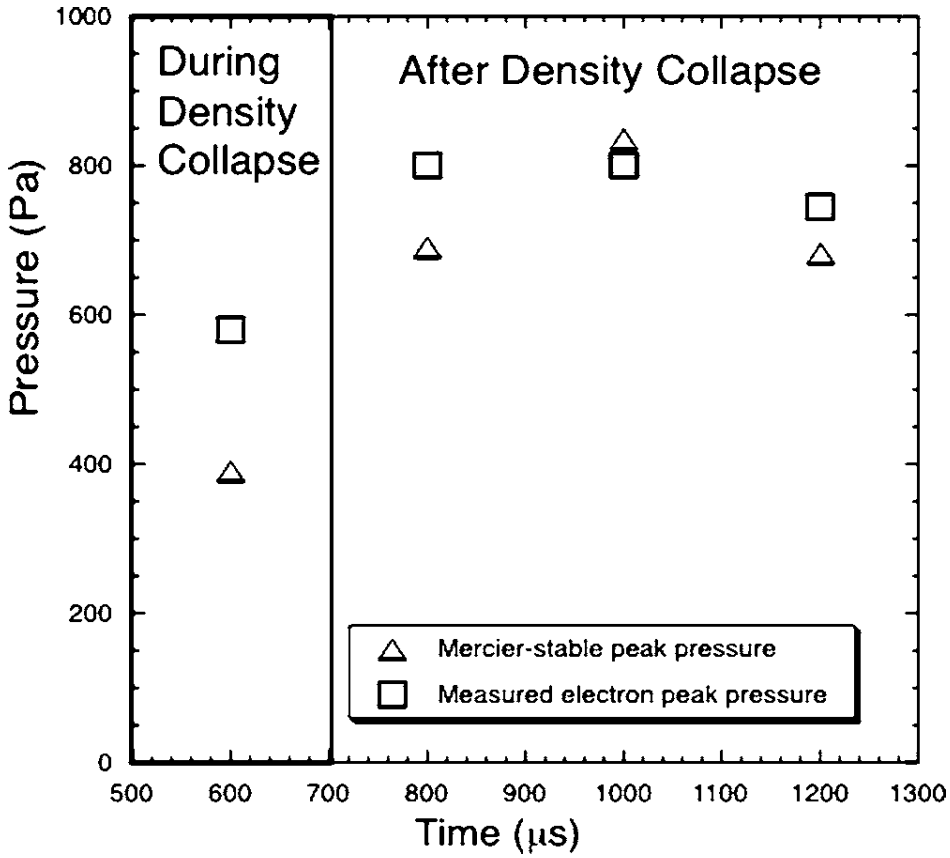

Figure 3.3: A plot of pressure values over time compared to the Mercier-calculated pressure values during and after a density collapse event in SSPX. Taken from Woodruff et al. in [28]

from this study was the stability of spheromaks generated by HIT-SI3 to the $n = 1$ instability similar to HIT-SI's stability; that is to say, the $n = 1$ energy detected by the edge probes is largely imposed by the injectors and does not display the same intermittent behavior consistent with plasma-generated mode activity. After subtraction of the spheromak and injectors the remaining $n = 1$ energy is comparable to other background modes. Additional examination of the plasma-generated modes from HIT-SI3 since the 2017 publication has revealed that while the plasma-generated $n = 1$ energy is within the low-energy spectral background of plasma-generated modes, in certain HIT-SI3 shots the plasma-generated $n = 2$ energy occasionally fluctuates and increases above the level of other modes, sometimes with a magnitude of 10-15% of the spheromak magnetic field. These shots also diplays fluctuations in the toroidal current that occur alongside the brief periods of elevated $n = 2$. These fluctuations were first noted in more detail on high-powered ($I_{gain} > 2$) shots taken during operations in the summer of 2018 using an injector frequency of 58.5 kHz, a "high" injector frequency. In addition to the high magnitude of the fluctuations, these shots were also of note as the FIR diagnostic was used to gather line-averaged density data which displayed similar fluctuations that appeared to coincide with the plasma-generated $n = 2$ and toroidal current fluctuations. Examination of this $n = 2$ energy in various shots will be presented and studied, with possible causes and numerical examinations discussed in following sections.

Observed presence of $n = 2$ activity

The BD subtraction technique was used to analyze high-frequency shots for plasma-generated activity during the summer of 2018, and intermittent $n = 2$ activity was noticed in was 180816020, a shot with injector phasing 240-120-0. A plot displaying the toroidal current and injector current evolution, proportion of magnetic modes measured by the surface probes, the magnetic mode proportions after subracting the injector empirical modes, and finally after subtracting the injector and spheromak empirical modes, can be seen in Figure 3.4.

While this shot was one of the first examples of the activity studied in depth, these

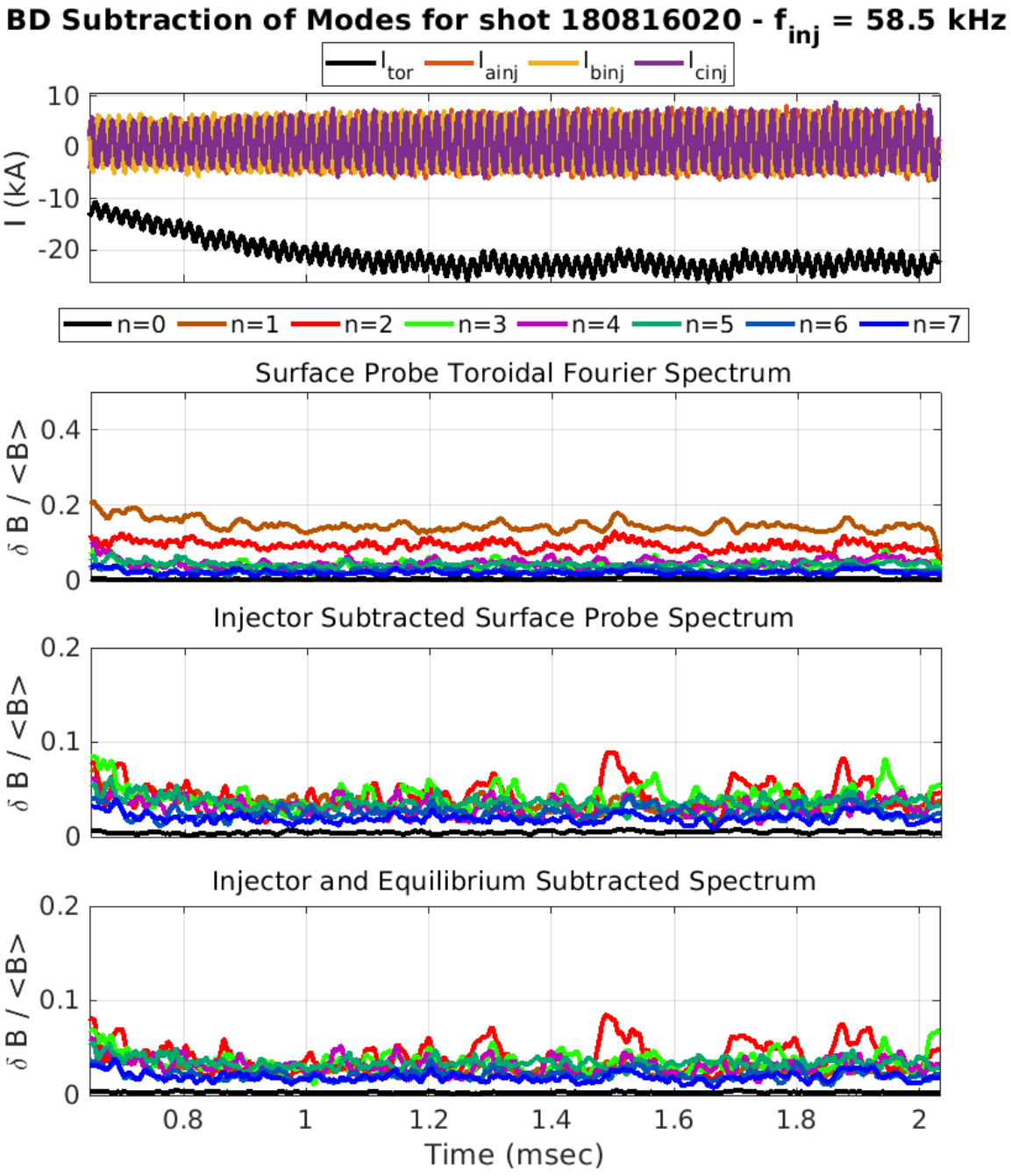

Figure 3.4: A plot of the toroidal and injector currents evolution of negative current 58.5 kHz shot 180816020 (top), along with the full measured, injector BD-mode subtracted, and equilibrium and injector subtracted Fourier mode spectrum (second, third, bottom, respectively). The intermittent plasma-generated $n = 2$ is clearly visible in the bottom plot.

transient increases in plasma-generated $n = 2$ energy can be found in spheromaks across a range of various parameters and operating conditions. One of these parameters is the "sign" of the toroidal current with respect to the toroidal direction defined by the initial labelling of the injectors A,B and C in the counterclockwise direction; the shot 180816020 generated "negative" shot, whereas a shot taken during the same operations day, 180816014, had a "positive" toroidal current. Although this shot used lower injector power, being taken on the same day gives the advantage of possessing similar machine conditions such as wall particle loading density. The currents and BD subtracted modes for the shot can be seen in Figure 3.5. The plasma-generated spectrum of 180816014 shows the presence of $n = 2$ not associated with the injectors or equilibrium, but rather than intermittent fluctuations of increasing and decreasing magnitude, the $n = 2$ is present as a steadily decreasing background as the toroidal current increases, with a transient nature appearing more toward the end of the discharge.

As discussed previously, the temporal phase of each helicity injector relative to one another can affect the mode spectrum of imposed perturbations, and consequently affect the measured mode spectrum. Shot 180904015 was taken at the same 58.5 kHz injector frequency as the previously shown discharges but with $\phi_{inj,0} = 0, \phi_{inj,1} = \frac{\pi}{3}, \phi_{inj,2} = \frac{2\pi}{3}$ and is shown in Figure 3.6. This shot, also possessing a negative toroidal current sign, displays the same intermittent fluctuations as 180816020, with the activity decreasing in magnitude as the shot progresses and the current gain increases.

Finally, while the activity was first noticed and appears to be more present in high-frequency discharges, examination of the BD plots of low-frequency ($f_{inj} = 15.6$kHz) shots taken in 2019 revealed some plasma-generated $n = 2$ activity present. Figure 3.7 shows positive current shot 190509011, and 3.8 shows negative current shot 190509012.

The previously presented data has shown that $n = 2$ fluctuations are present in a wide range of HIT-SI3 shots and are a persistent feature worth deeper investigation. The next sections will examine data that can shed light on the internal dynamics taking place in HIT-SI3 during these $n = 2$ fluctuations.

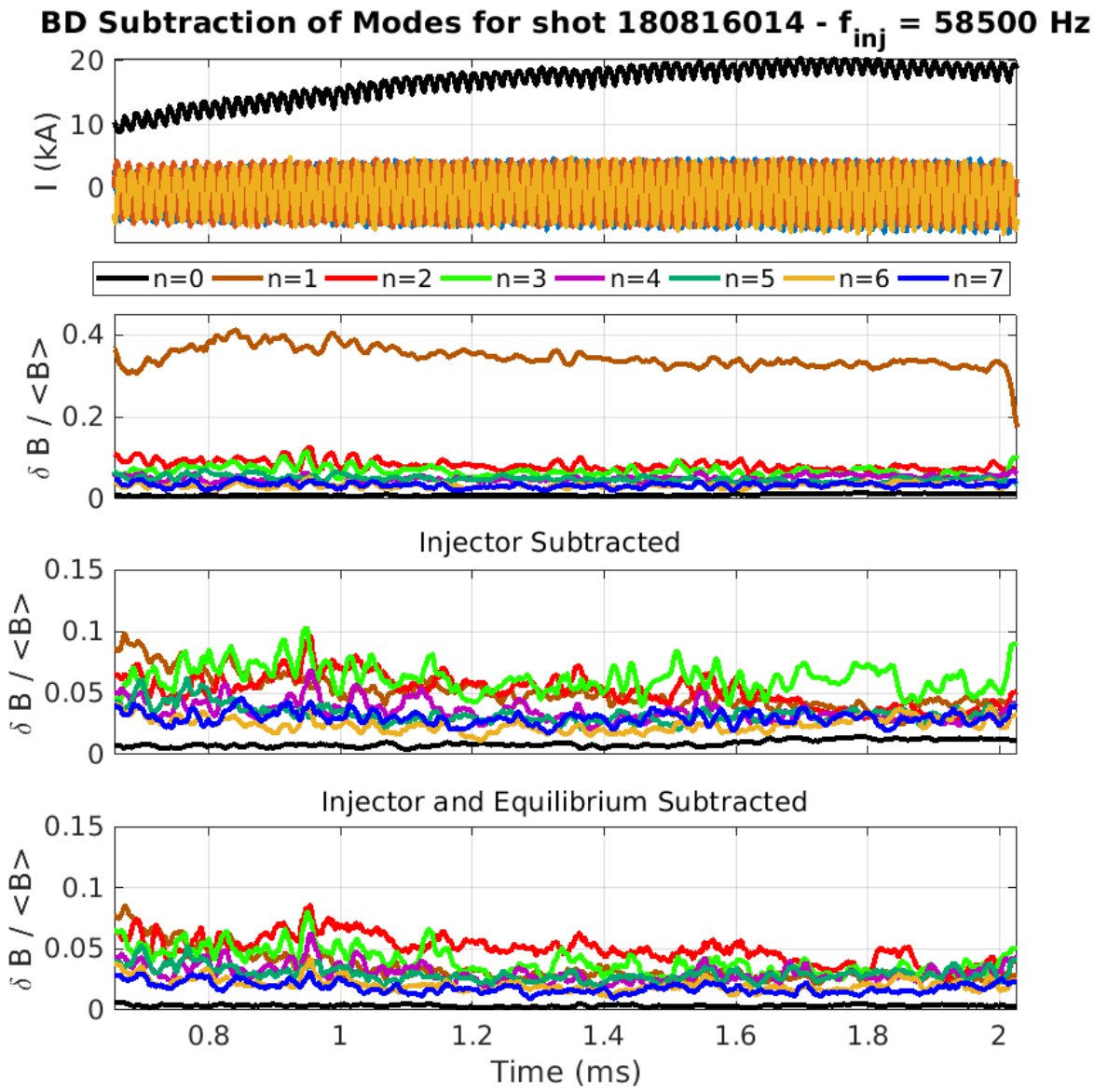

Figure 3.5: A plot of the toroidal and injector currents evolution of positive current 58.5 kHz shot 180816014 (top), along with the full measured, injector BD-mode subtracted, and equilibrium and injector subtracted Fourier mode spectra (second, third, bottom, respectively). The plasma-generated $n = 2$ takes on a more constant nature in this case.

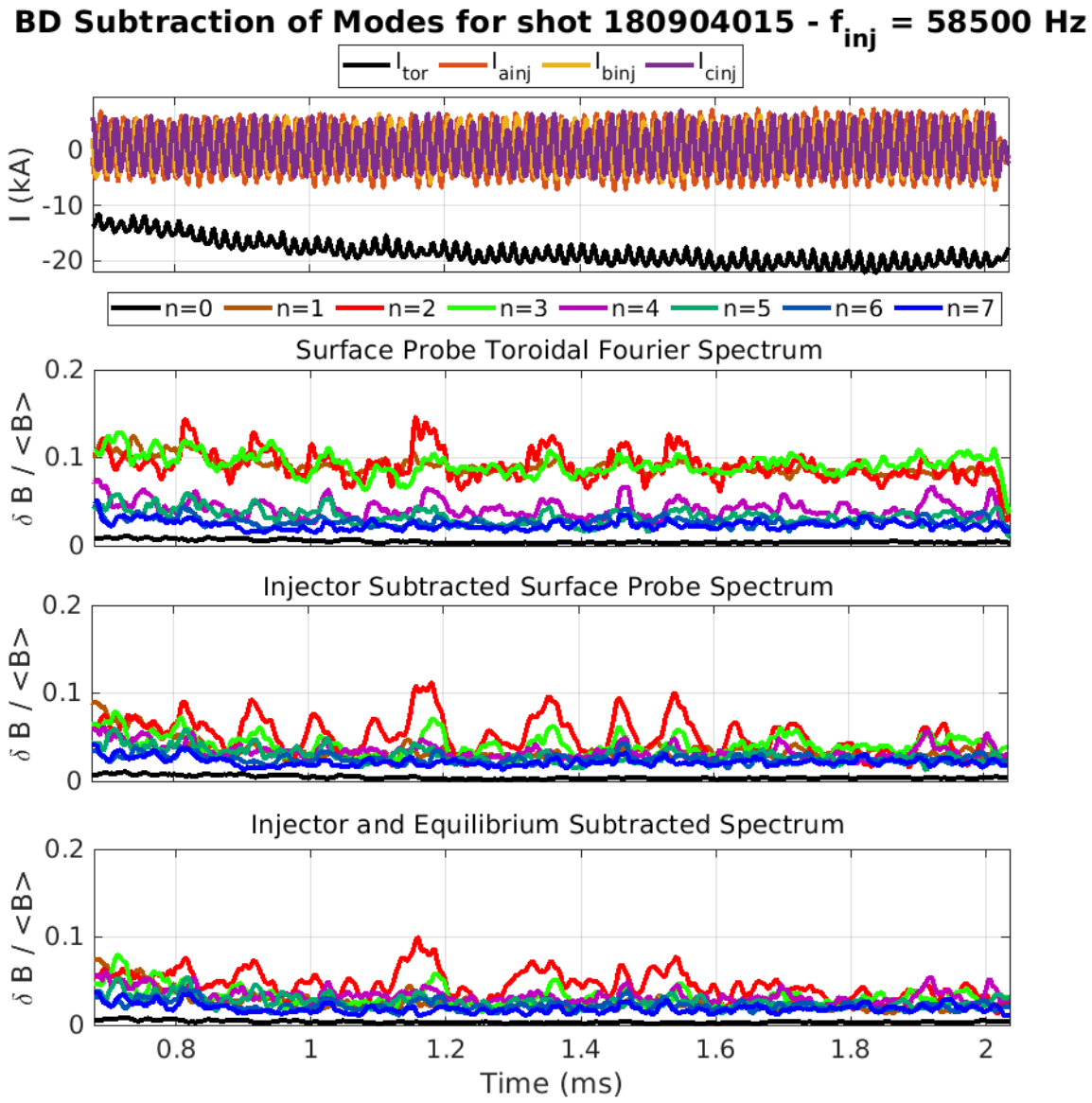

Figure 3.6: The BD summary plot in the same style as presented above for HIT-SI3 shot 180904016 with 60 degree phasing rather than 120. The plasma-generated $n = 2$ in this case resembles the intermittent fluctuations seen in the 120 negative shots.

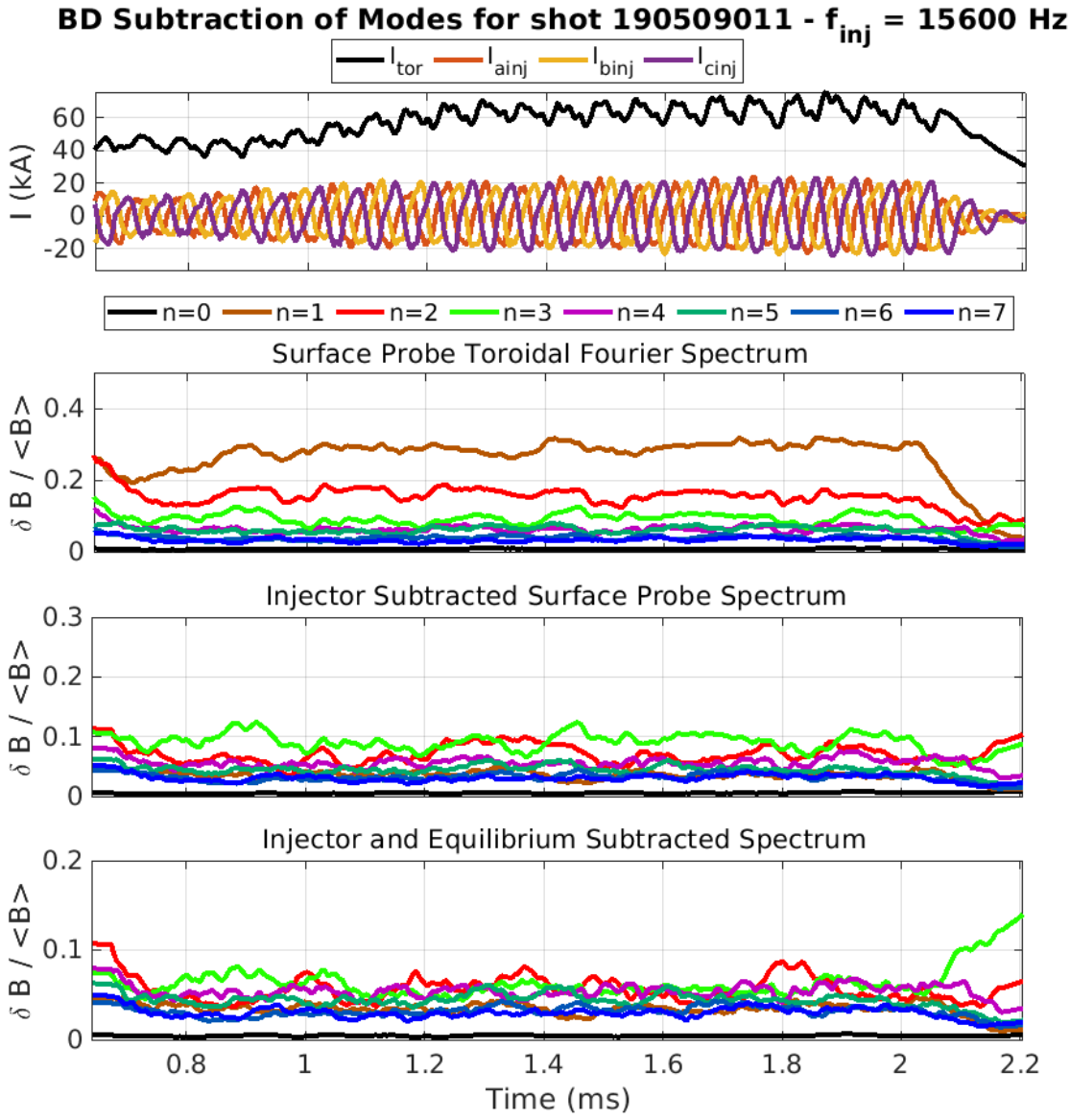

Figure 3.7: BD summary plot for positive toroidal current low frequency 15.6 kHz shot 190509011, displaying little plasma generated $n = 2$ except for a single blip at the end.

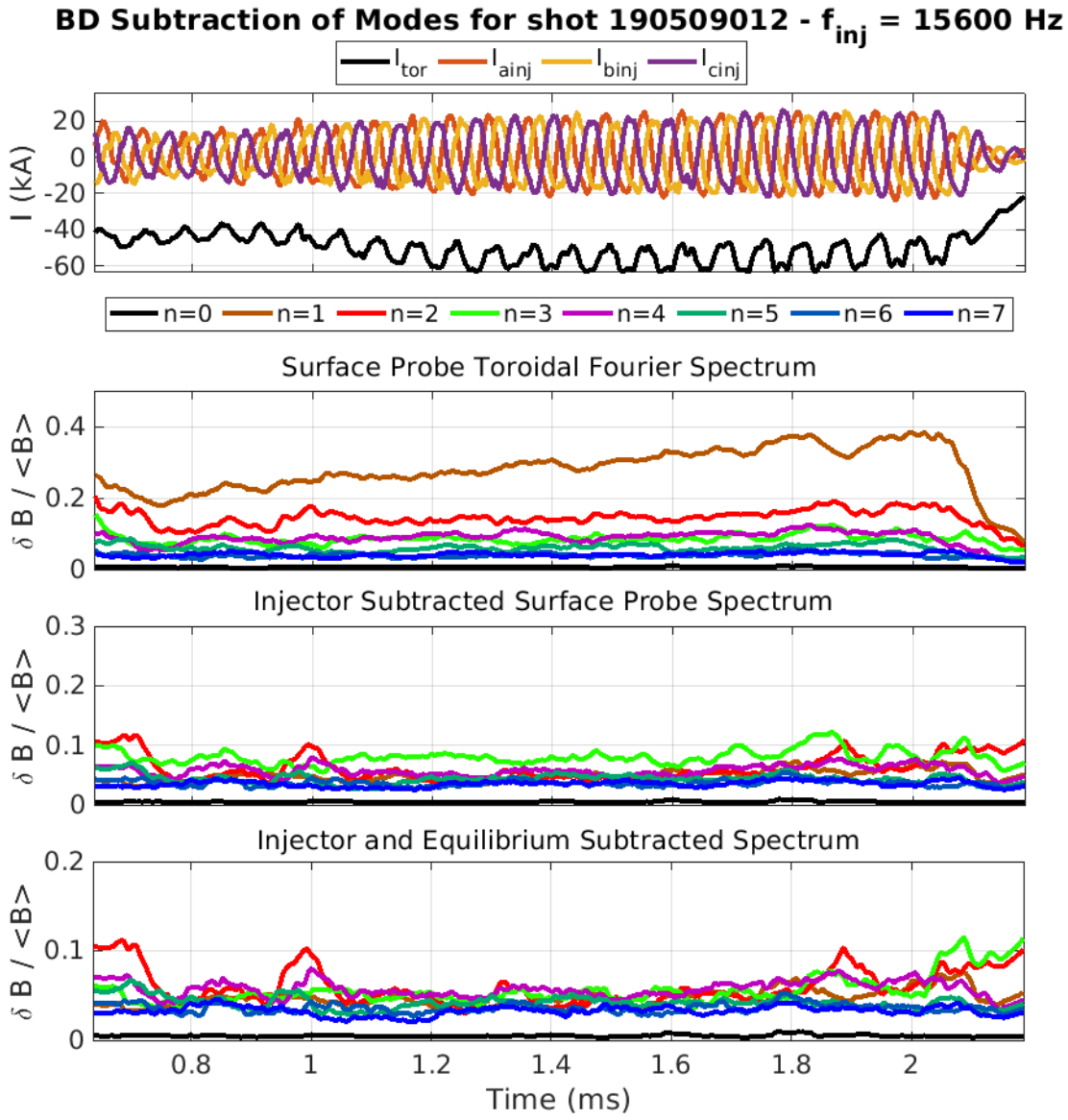

Figure 3.8: BD summary plot for negative toroidal current 15.6 kHz shot 190509012, again showing little $n = 2$ activity in the equilibrium and injector subtracted spectrum except for a small fluctuation towards the end.

Internal magnetic field fluctuations associated with $n = 2$

The three-trident Internal Magnetic Probe (IMP), reviewed in Chapter 1, allows the internal magnetic profile of HIT-SI3 speromaks to be examined in detail across the outer portion of the major radius. During one example of the $n = 2$ fluctuation, between 1.85 and 1.95 msec in shot 180816020, the measurements for the toroidal and poloidal fields from the IMP during that period indicate substantial profile variation, as show in Figure 3.9. In particular, between the beginning and the end of the chosen time window, the poloidal magnetic field profile changes shape, flattening, which suggests similar changes occurring in the toroidal current and λ profiles.

Magnetic field fluctuations from the IMP can be analyzed using the same BD suntraction technique, creating signals that consist of plasma-generated fields at each probe location. Examining the plasma-generated fields on the IMP can shed light on the radial structure and behavior over time of the $n = 2$ activity. Figure 3.10 displays the fluctuations from plasma-generated activity measured by the IMP, with the reconstructed signals at each radial location plotted along the right vertical axis (the left vertical axis showing the offset magnetic field amplitude compared to the previous location, not the total internal magnitude). Examination shows sudden fluctuations occurring across the radial length of the probe at the approximate times of the $n = 2$ fluctuations in the plasma-generated spectrum measured by the surface probes. Tracing a line through the peak of the IMP signal fluctuations (green dashed lines) that appear at the times when the $n = 2$ amplitude increases above background, we see a slight slope indicating this is a feature that is radially propagating outwards, not an instantanteous profile change. The time for this propagation to radially transit from the inner probe to the edge varies but is between 10-30 , which corresponds to the radial sound transit time:

$$\tau_{C_s} = \frac{R}{\sqrt{\frac{\gamma P}{\rho}}} \tag{3.2}$$

This propagating feature is closely followed by a sudden reversal in phase in the magnetic

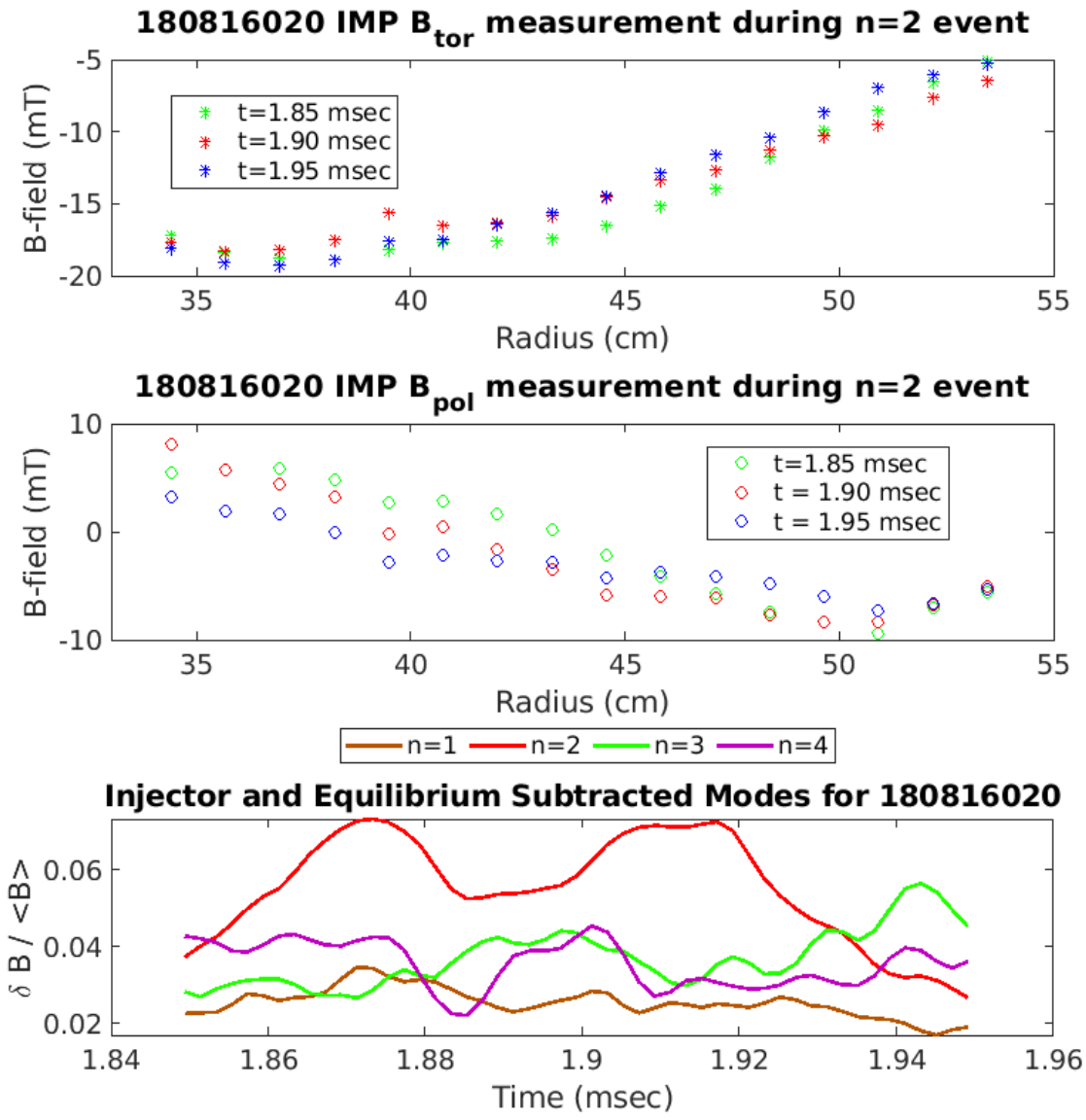

Figure 3.9: Plot of IMP-measured magnetic field in the toroidal (top) and poloidal (bottom) directions at three times across a 100 μsec window around a $n = 2$ fluctuation at 1.9 msec in HIT-SI3 shot 180816020. The field shows substantial variation during this time, indicating λ profile variation as well.

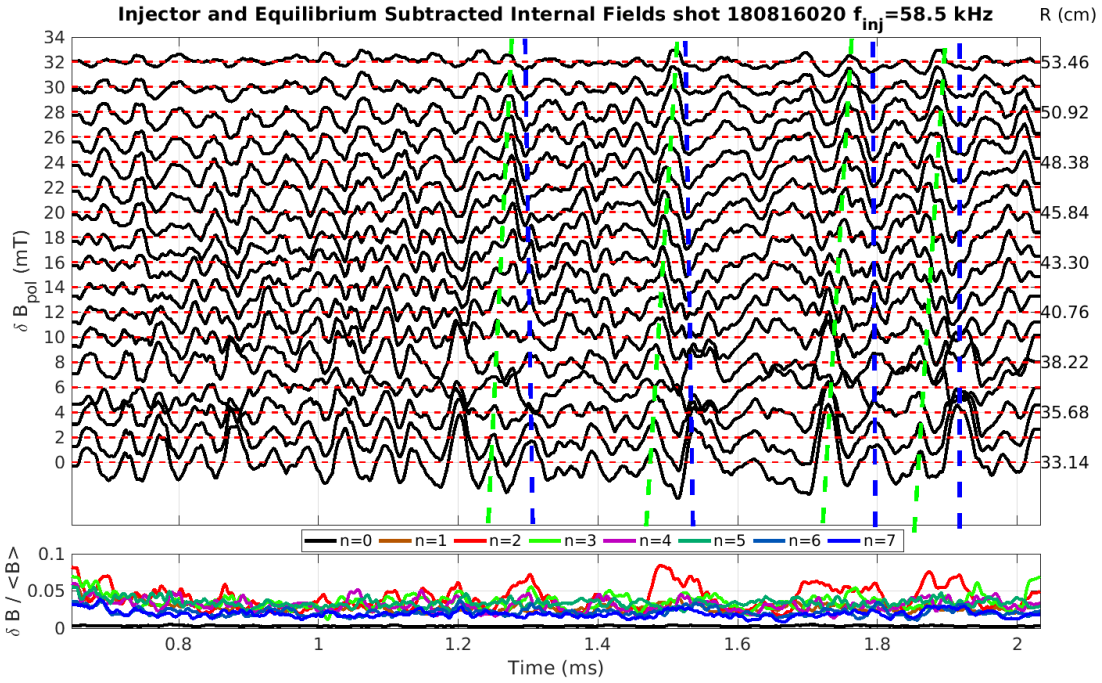

Figure 3.10: A plot of the time trace of the injector and equilibrium BD mode subtracted IMP B_{pol} measurements from shot 180816020, with fluctuations marked with blue and green dashed lines. The blue lines trace through a faster fluctuation, whereas the green lines are visibly sloped intercepting a slower radially-propagating feature.

fluctuations (indicated by the blue dashed lines) that occurs at a scale comparable to the radial Alfvén transit time if not faster:

$$\tau_{R,Alf} = \frac{R}{\frac{B}{\sqrt{\mu_o \rho}}} \tag{3.3}$$

While inconclusive in isolation, the time periods of these plasma-generated instabilities and their spatial structure suggest some type of profile rearrangement occurring that coincides with the observed $n = 2$ fluctuations.

Fluctuations in Chord-Averaged Density

Data from the single-chord FIR interferometer system used on HIT-SI3 between 2015 and 2019 revealed that, in addition to fluctuations in the edge magnetic fields and profile change in the internal field profile, the $n = 2$ events also cause fluctuations in the line-averaged density measurements. While the shot 180816020 did not have the FIR operational, density data is available for shot 180904015 which also displayed similar $n = 2$ fluctuations. Figure 3.11 displays the raw data along with the injector-frequency averaged trace. While the injector-frequency oscillations are quite prominent, there are also oscillations that appear at a much lower frequency. To determine if there is a particular dominant low frequency in the density oscillations, the Fourier transform of the data in time was taken and the magnitude of each frequency was plotted as can be seen in Figure 3.12. The Fourier spectrum in frequency is mostly concentrated on the "1 kHz" component constituting the inverse of the shot period and also shows a large spike at the injector frequency, as expected. The more interesting features are relatively large amount of energy (compared to the background) between 4-6 kHz and 11-15kHz. This indicates there is almost as much contribution to the overall oscillation of the density trace from this lower frequency component, as there is from the injectors, making it a major component of the dynamics of the system.

To help establish any correlation between the oscillations seen in density, the intermittent $n = 2$ activity, and other experimentally-measured quantities, Fourier transforms from a time to a frequency domain were again used to determine if there is a dominant lower frequency in the data. The toroidal current and plasma-generated $n = 2$ magnitude were the two most complimentary choices, and the Fourier transform plots can be seen in Figures 3.13 and 3.14. While the toroidal current has a mostly broad spectrum at lower frequencies (and the obvious spike at the injector frequency), the $n = 2$ data has a very large spike at 5 kHz. This agrees with the examined visual duration of the plasma-generated $n = 2$ peaks seen in the BD subtraction plots.

Dividing the roughly 1 millisecond period of high current gain ($I_{gain} > 2$) in shot

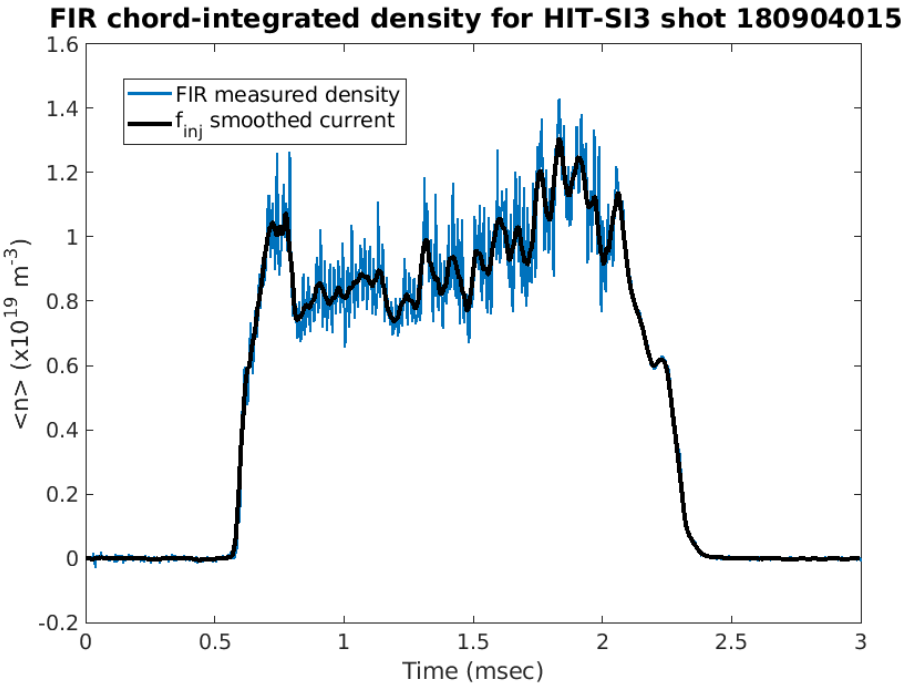

Figure 3.11: The line-averaged electron density $\langle n \rangle$ measured from the FIR on shot 180904015, a 58.5 kHz, 0-60-120 degree phased shot.

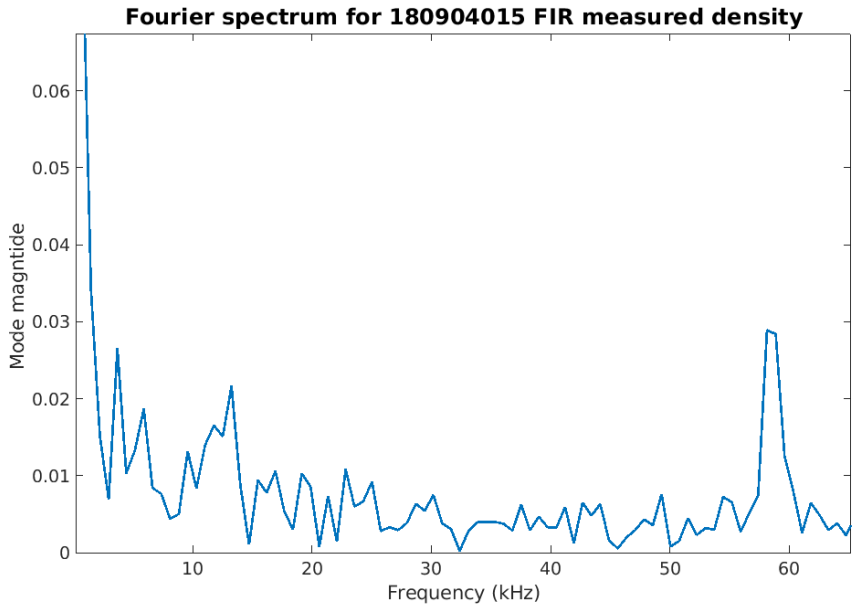

Figure 3.12: The absolute value of the magnitude of the Fourier modes for each frequency after taking the Fourier transform of the FIR-measured density as a function of time. The Fourier mode magnitudes show several large spikes at 4-6 kHz and 11-15 kHz in addition to the injector frequency at 58.5 kHz.

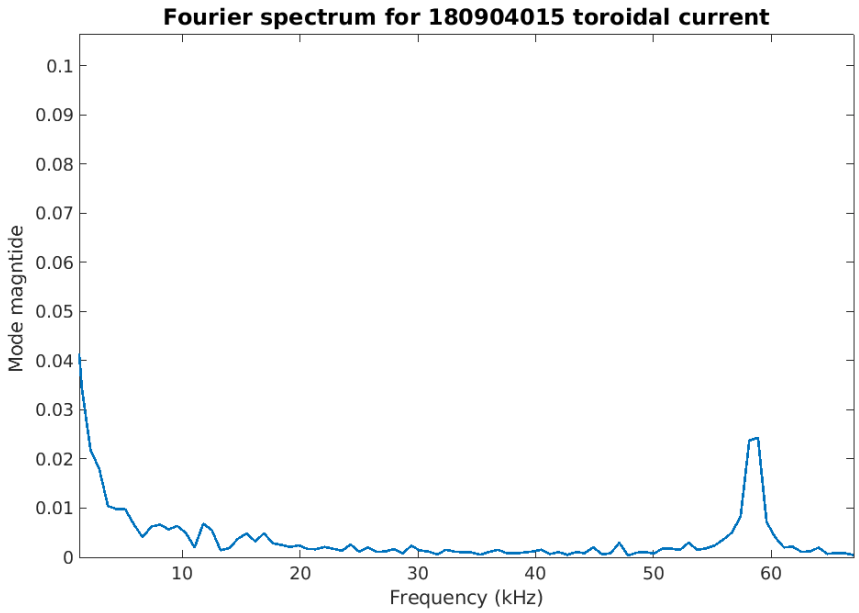

Figure 3.13: Absolute magnitude of the Fourier modes from the Fourier transform of the time evolution of the toroidal current. Other than the injector frequency and frequency corresponding to the 1 msec of the sustainment period, there are no prominent spikes.

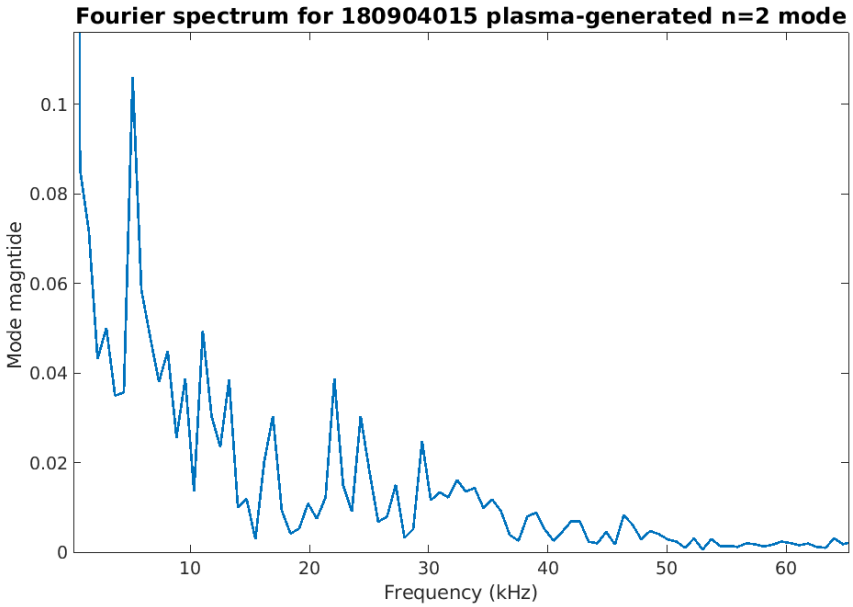

Figure 3.14: Absolute magnitude of the Fourier modes from the Fourier transform of the $n = 2$ plasma-generated field over time. A strong spike at 5 kHz is present.

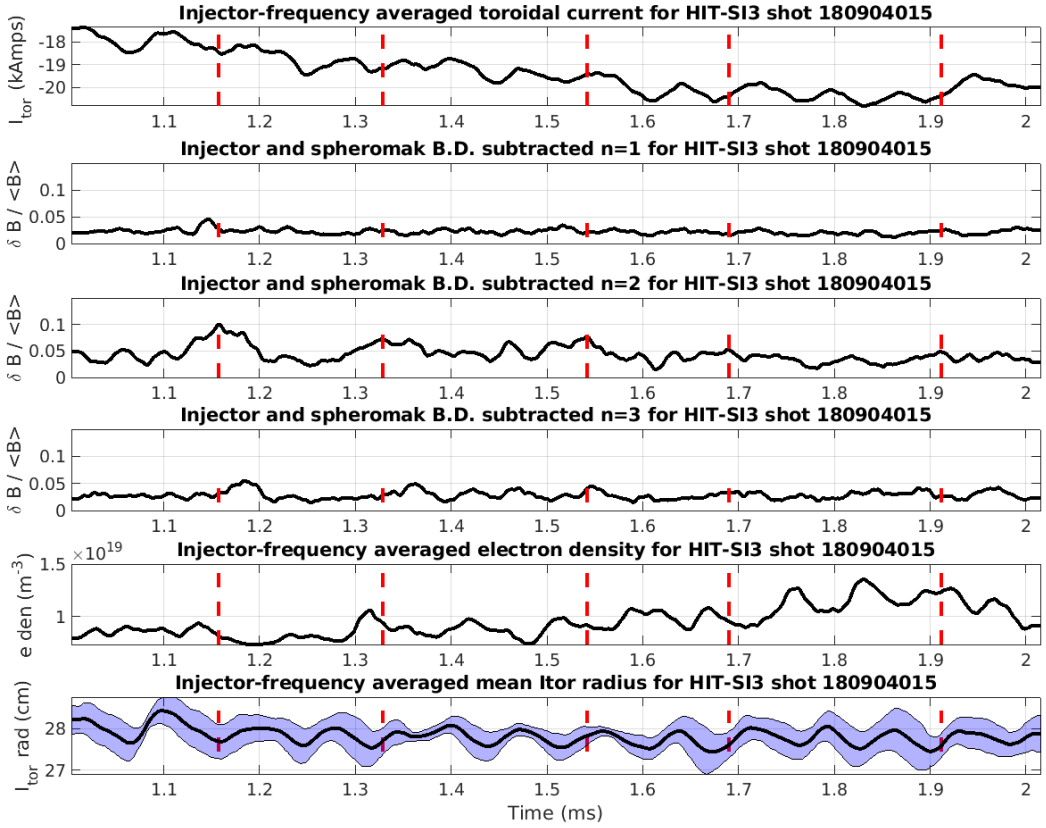

Figure 3.15: Plot of toroidal current, plasma-generated $n = 1$, $n = 2$, $n = 3$ field magnitude, density, and current centroid radius for shot 180904015, with red dashed lines marking the peaks of $n = 2$ field magnitude in every 200 μsec window.

180904015 into 200 μsec windows, the time of the maximum plasma-generated $n = 2$ magntiude in each time window was determined and marked with a red dashed line in Figure 3.15; those times were also marked in the time traces of other quantities such as toroidal current, the $n = 1$ and $n = 3$ energies, the FIR-measured density, and centroid radius. This was done to see how these other quantities behave as the $n = 2$ peaks in magntiude and gain insight on the nature and possible origin of those fluctuations.

Times of maximum $n = 2$ magnitude appear to coincide with minor crashes in the

magnitude of the toroidal current and the line-integrated density. The radial position of the current centroid appears to be oscillating in position with a 50-100 μsec time period, and the marked times of maximum $n = 2$ coincide with the radial position moving outward from the troughs of these oscillations. Interesting as well, the other two non-axisymmetric modes plotted do not show much major activity, indicating these dynamics may be driven almost entirely from the activity of the $n = 2$ mode. The variations in global quantities that accompany the plasma-generated $n = 2$ detected on the surface probes have proven to be an interesting indication of some sort of internal rearrangement or even instability, but the experimental data available are too limited to draw definitive conclusions. The next section will examine this possibility using software to fit the reconstruct equilibria from experimental data and track their evolution.

3.2 Equilibrium Reconstruction using PSI-Tri and Experimental Data

The PSI-Tri code was used to generate equilibrium reconstructions, solutions to the Grad-Shafranov equation using experimental HIT-SI3 data. Magnetic probe data from HIT-SI3 experimental shots can be used to reconstruct a magnetic equilibrium by minimizing the difference between the measurements from the IMP and surface probes with the computed 2D axisymmetric equilibrium. Functional forms are chosen for the flux function F profile and pressure profile, but otherwise are evolved to solutions that minimize the probe data. This method only provides a static equilibrium solution in a 2D axisymmetric domain, and while the reconstructed mean fields of HIT-SI3 are expected to have some degree of axisymmetry, the true nature of HIT-SI3 over time is dynamic and highly 3D. It follows the PSI-Tri solutions are limited in the extent to which they can be compared to experimental data, but when equilibrium fits are taken using data over a series of time points, they are useful for estimating the evolution of quantities that cannot be easily measured from the experiment. PSI-Tri fits were performed using HIT-SI data with good agreement and contributed to evidence of pressure confinement and stability to the $n = 1$ mode.[13][37] The following attempts using HIT-SI3 data do not provide as clear a picture as the HIT-SI study, but

nonetheless suggest interesting behavior that may occur during the periods experiencing plasma-generated $n = 2$ fluctuations.

3.2.1 Low-frequency equilibrium reconstructions

After the discovery of the $n = 2$ activity in low-frequency HIT-SI3 shots, these shots were used first for reconstruction on the assumption that the reduced level of fluctuations, compared to high frequency shots, might yield more accurate fits. The PSI-Tri fits were specifically taken at 10 μsec intervals during the 200 μsec window in which the $n = 2$ fluctuation occurred. A linear flux function was chosen for the fits:

$$F(\hat{\psi}) = 1 + \alpha(2\hat{\psi} - 1) \tag{3.4}$$

where $\hat{\psi}$ is the normalized poloidal flux and the constant α sets the slope and is adjusted as the error between the fit and data is minimized. Figure 3.16 displays the toroidal current, β, and λ generated by the PSI-Tri reconstruction of shot 190509011, a positive toroidal current shot taken using $f_{inj} = 15.6$ kHz, presented in the previous section. The reconstruction covers the period between 1.7 and 1.9 msec, during which a plasma-generated $n = 2$ fluctuation can be observed in the lowest plot in Figure 3.7. The reconstructed IMP toroidal (B_ϕ) and poloidal (B_θ) magnetic profiles profile (blue) and experimental data (red) are displayed at in the leftmost plots in the figure, taken at time 1.78 msec. The dashed black line in the time-varying trace plots marks this time on those quantities for reference.

The reconstructed internal magnetic profiles indicate this fit is somewhat inaccurate, with the profile shape and magnitude of the experimental fields not matching the reconstructed fields from PSI-Tri. This is a clue that the fits may not be as useful as initial hoped based on past experience with HIT-SI data. The reconstructed volume-averaged β during the $n = 2$ event appears to rise to nearly double its value just after the peak of the non-equilibrium fluctuation at around 1.8 msec. The measured edge λ does not show much variation, being predominately the imposed injector λ, but the core λ from the reconstruction drops in value at the time of the plasma-generated $n = 2$ peak, after having elevated slightly just prior.

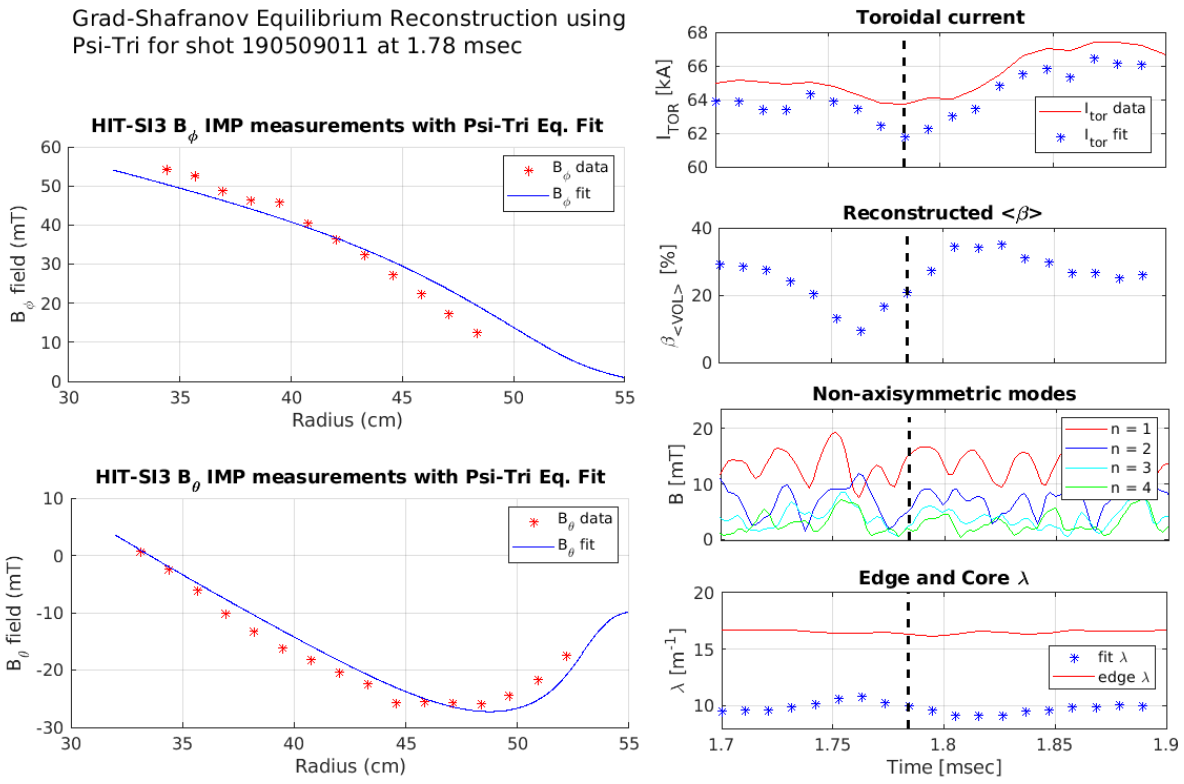

Figure 3.16: PSI-Tri outputs for B_{tor}, B_{pol}, I_{tor}, β, magnetic modes (from experiment) and λ for HIT-SI3 shot 190509011 at time t=1.78 msec, during the $n = 2$ fluctuation observed in Figure 3.7.

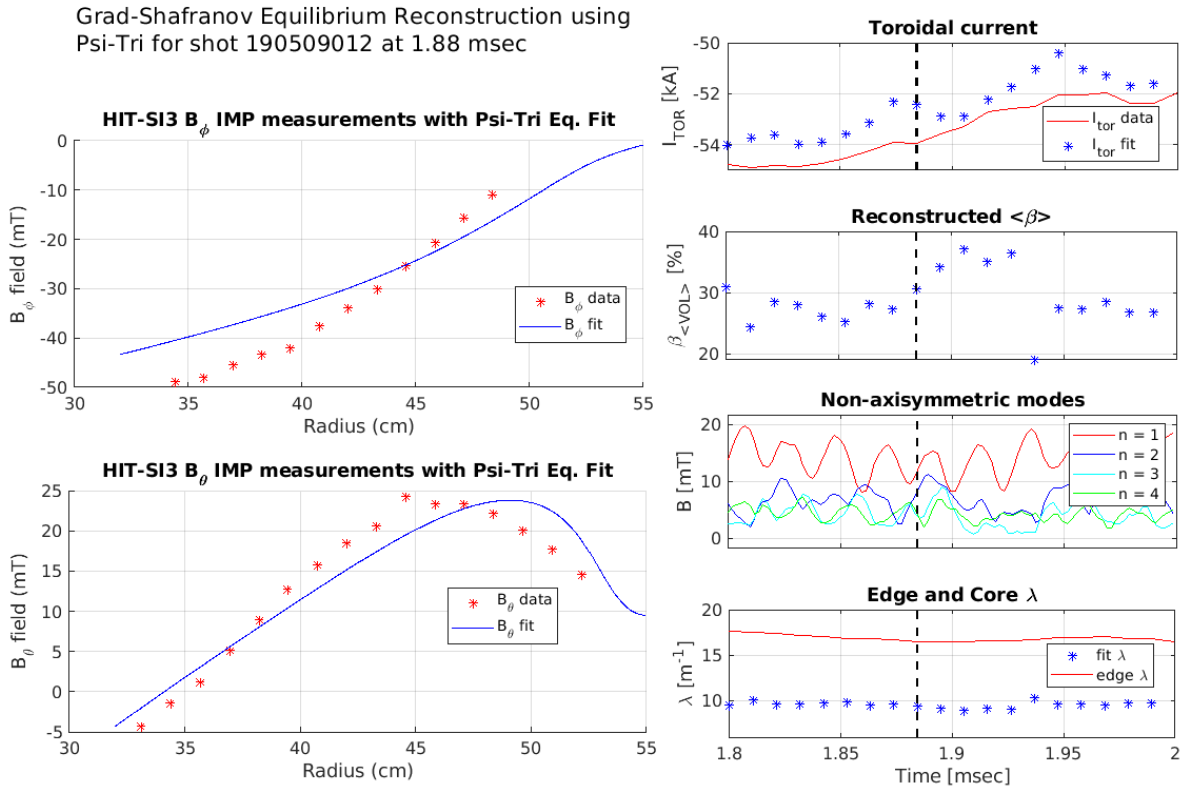

Figure 3.17: PSI-Tri outputs for B_{tor},B_{pol}, I_{tor}, β, magnetic modes (from experiment) and λ for HIT-SI3 shot 190509012 at time t=1.88msec, during the $n = 2$ fluctuation observed in Figure 3.8.

The negative current shot, 190509012, showed substantially worse fit, with the shape and values of the calculated magnetic field even further off from the previously fit positive current shot. Again, at the peak of the plasma-generated $n = 2$ just after 1.9 milliseconds, the reconstructed β rises and then crashes in value. The core λ value from the reconstruction also varies, but interestingly increases after the peak rather than decreasing.

It is immediately apparent that compared to previous works with HIT-SI, the PSI-Tri solutions for HIT-SI3 have worse agreement. While this can be due to a variety of factors, a large contribution to the disagreement may come from the lack of vertical symmetry in HIT-SI3. The $\vec{J} \times \vec{B}$ forces from the injectors firing are approximately vertically balanced in HIT-SI, but the injectors in HIT-SI3 are only located on one side, creating an average downward force on the spheromak that has been observed to push the spheromak center downwards from the midplane. Therefore, the magnetic field profiles from the equilibrium reconstruction are likely offset to a degree from the vertical displacement of the experimental mean fields. Regardless, the result of increasing $< \beta >$ and shifting core λ are both interesting in light of the previous discussion of $n = 2$ instabilities driven by spheromaks reaching β limits and the changes in current/λ that occur as a spheromak enters a region of instability.

3.2.2 High-frequency equilibrium reconstructions

Reconstruction data of the shot originally investigated for the behavior, 180816020, is displayed in Figure 3.18. Both the toroidal and poloidal field measurements from the Grad-Shafranov solution are skewed both in the overall magntiude and shape; the profile shape is already compromised due to the use of a linear λ profile when the magnetic profile suggests a more convoluted shape. The reconstructed volume-averaged β undergoes substantial variation during the $n = 2$ event like that observed in the low frequency shots, possibly havling in value from a peak of 60% just before the $n = 2$ mode increases in magnitude to 30%; however judging from the quality of the internal profile fit, these β values are highly unreliable. A more complicated λ profile than the linear profile used as a guess may imply more subtle changes to β than the reconstructions can capture.

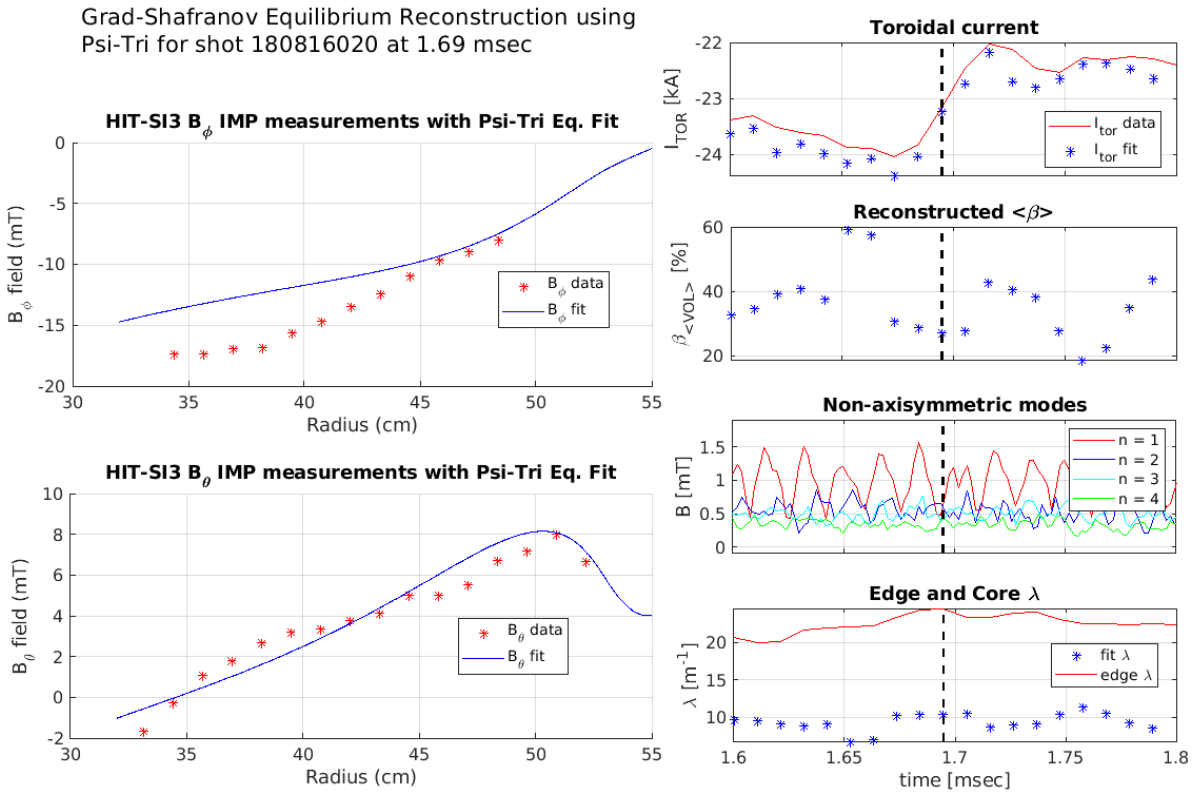

Figure 3.18: PSI-Tri outpit plot of B_{tor} and B_{pol} profiles as well as I_{tor}, magnetic modes, β, and λ for high frequency shot 180816020.

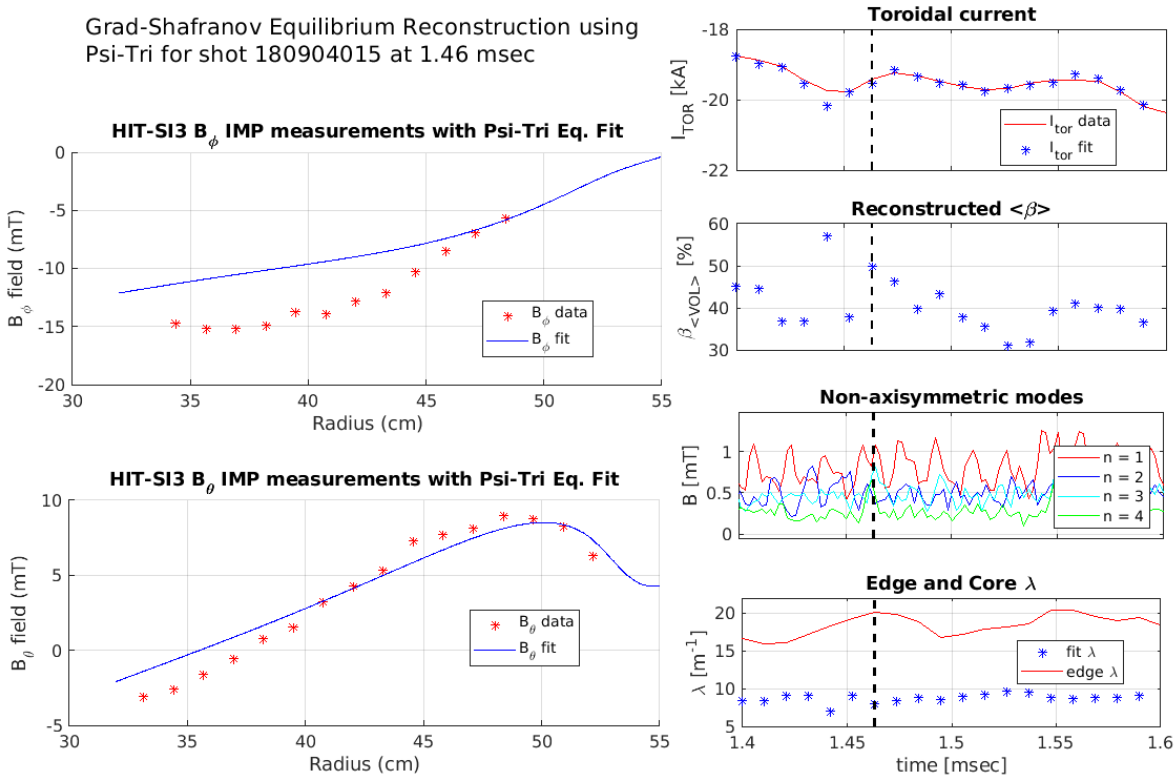

Figure 3.19: PSI-Tri outpit plot of B_{tor} and B_{pol} profiles as well as I_{tor}, magnetic modes, β, and λ for 58.5 kHz and 0-60-120 phased HIT-SI3 shot 180904015.

While 180904015 was taken at a different phasing (0-60-120), the Grad-Shafranov reconstruction from PSI-Tri is of similarly poor quality, and fails to fit the experimentally measured profiles. The toroidal field profile in particular is severely mismatched, and while we again see an increase in β during the $n = 2$ event, this again cannot be taken at face value due to the disagreement in the fit.

The high-frequency reconstructions have substaintially worse agreement than the already poor low-frequency reconstructions; this may be due to a variety of factors but the two most likely candidates are: 1) Increased downward shift of the spheromak current centroid at higher injector frequencies 2) average field measurements appear more discontinuous over

time as high frequency has more non-axisymmetric activity distorting the axisymmetric equilibrium (explained further in the next section). Some attempts were made to use profiles such as a more complicated piecewise-linear function, as well as the two-step IDCD profile originally theorized by Jarboe in [31]. The end results of these attempts, however, did not yield better results than the displayed reconstructions using a simple linear profile. If there had been more time to dedicate to this segment of the study, methods to make the fitting more sophisticated would and been tried. This will be discussed in depth more in Chapter 5, in suggestions for future studies.

3.3 Investigation of $n = 2$ activity using NIMROD

Intensive study of the presence of these $n = 2$ fluctuations in HIT-SI3's high frequency shots was initiated during the 58.5 kHz shot campaign performed in 2018 after this activity was observed, as noted above. To see if the fluctuations would be replicated in NIMROD, and to create a numerical analogue for analysis, the process outlined in Chapter 2 was applied to create an injector boundary waveform file for the 0-120-240 degree phased shot 180816020. This waveform was then used to drive spheromaks from formation in three simulations using zero-β (no temperature or density evolution), single-temperature, and two-temperature MHD models. The use of three models was hoped to clarify what observed effects might be due to magnetic field activity alone, and which effects could be attributed to changes in temperature and pressure. The three simulations will be analyzed both using synthetic diagnostics and examination of data not accessible in experiment and compared against one another for the above purpose, as well as briefly compared with simulations of HIT-SI. The results will be compared to the experimental measurements from HIT-SI3 to determine the how relatable the observed simulation results really are to the experimental phenomena. Due to the constraints of available diagnostic data and the results of the simulation, several high frequency shots from summer of 2018 will be used as a basis for comparison in addition to 180816020. While this might decrease the validity of a strict comparison to the original experimental shot and its behavior, all the shots used for comparison were taken during

similar machine conditions and exhibited the same $n = 2$ presence, which still makes the NIMROD simulations useful as a computational model of such behavior.

3.3.1 Summary of results

Simulation evolution

The toroidal currents, magnetic energy spectra (plotted using a logarithmic y-axis), and kinetic energy spectra for zero-β, single-temperature, and two-temperature NIMROD simulations of 180816020 can be examined in Figures 3.20, 3.21, and 3.22. In each of the toroidal current traces produced from synthetic magnetic probe data (as in the experiment), the fluctuation events similar to those seen experimentally are apparent, and their associated changes in magnetic energy are also displayed. In all three models, the fluctuations in toroidal current appear to occur with fluctuations in the magnitude of the volumetrically-integrated $n = 1$ energy. The $n = 2$ energy appears to increase slightly in magntiude during these periods, however the volumetric $n = 2$ activity primarily manifests as a slight increase in the injector-frequency oscillations. The higher-order modes displayed reflect this activity to a lesser extent, with small fluctuations in the $n = 3$, $n = 4$, etc. occurring with the $n = 1$ and current fluctuations. The kinetic energy spectra shows more variation between simulation models, with the $n = 1$ kinetic energy in the zero-β simulations increasing and decreasing with the fluctuation in the toroidal current; in the finite-β simulations, the fluctuations in the kinetic energy are substantially suppressed, with brief $n = 1$ spikes in both finite-β simulations occurring with the fluctuations in the $n = 1$ magnetic energy. This may suggest the increased influence of pressure and temperature effects in the finite-β simulations; whereas the primary force on the particles in the zero-β simulation are due to magnetic fields, pressure-driven forces play a role on the fluid flows and kinetic energy when density and temperature are allowed to evolve.

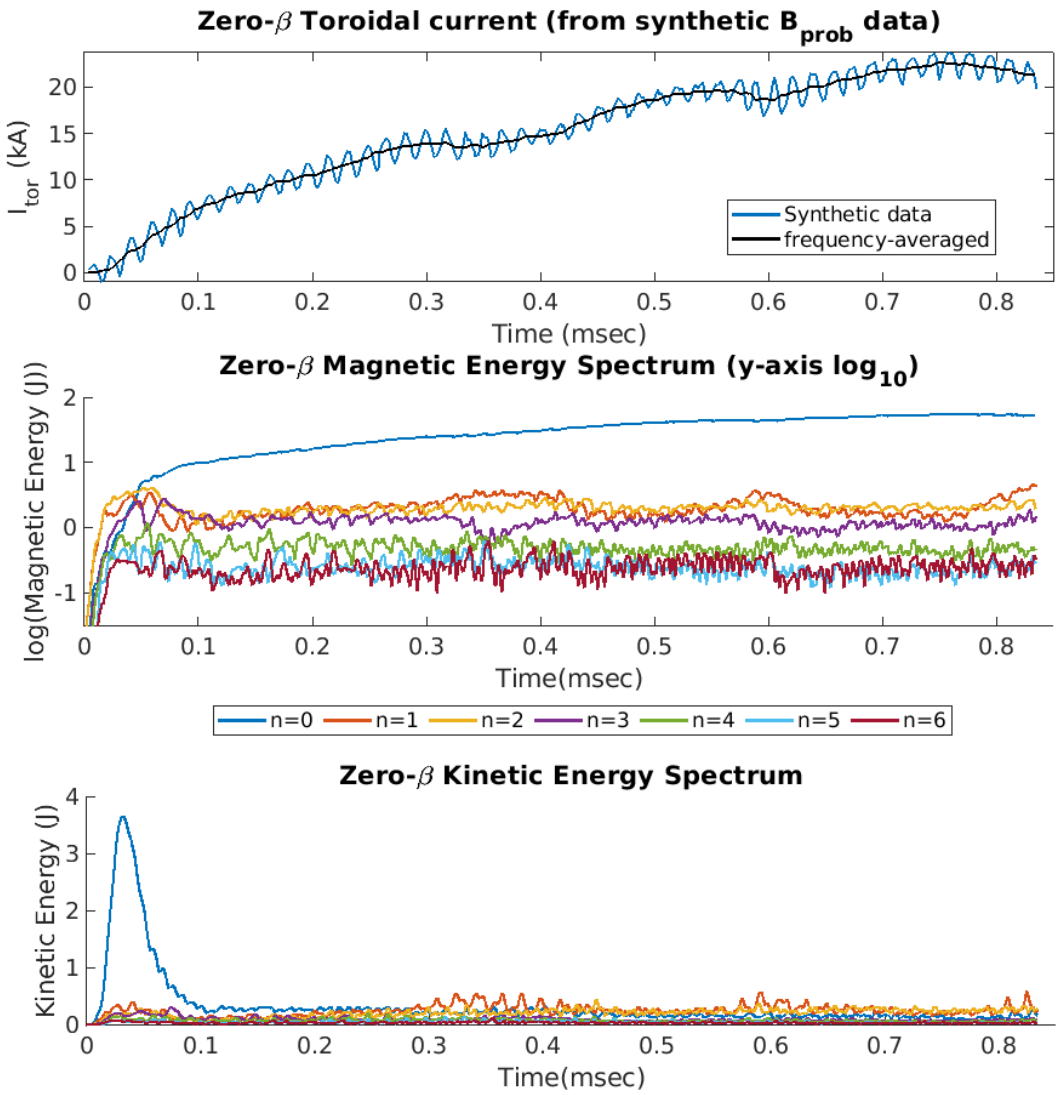

Figure 3.20: Toroidal current evolution and volume-integrated magnetic field Fourier mode energies for the zero-β simulation of shot 180816020.

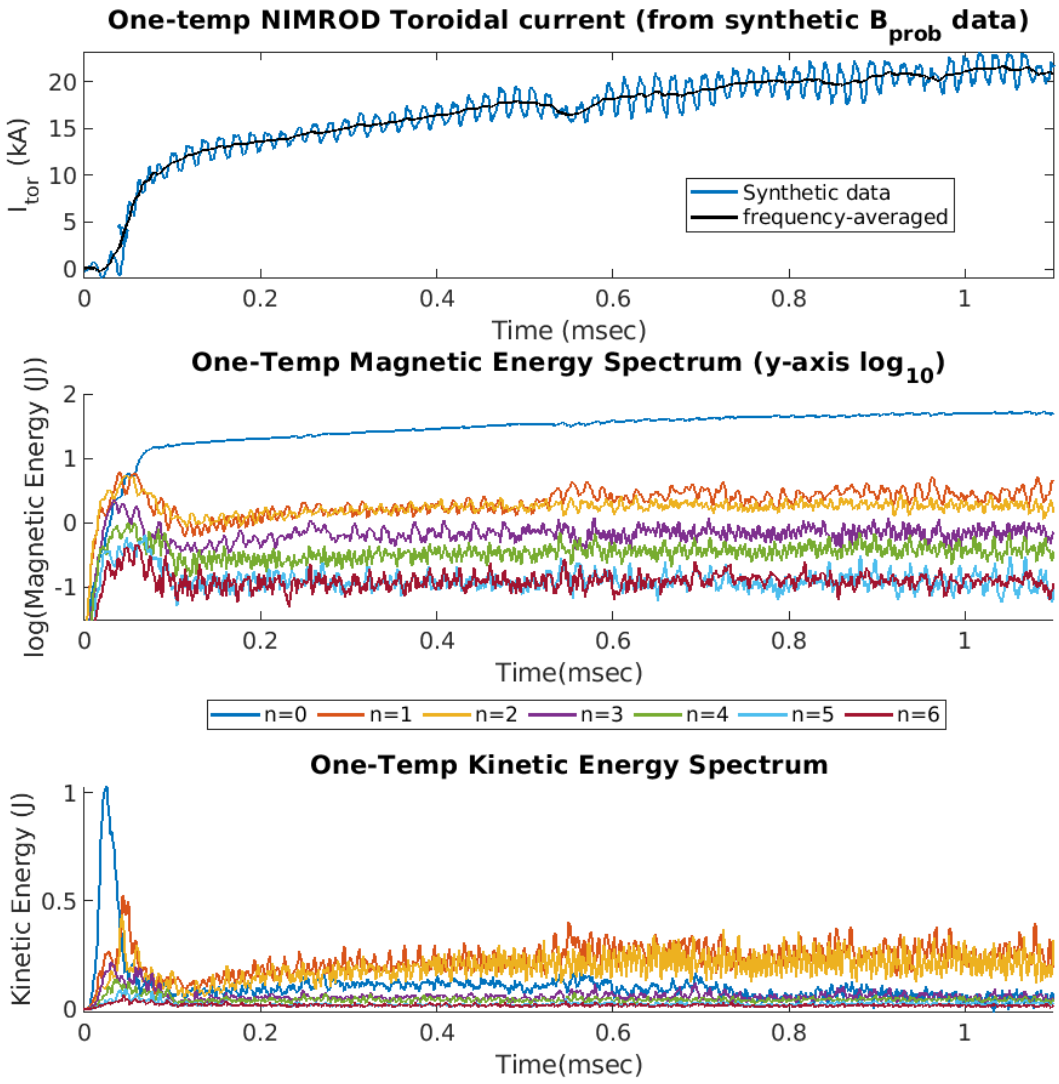

Figure 3.21: Toroidal current evolution and volume-integrated magnetic field Fourier mode energies for the single-temperature simulation of shot 180816020.

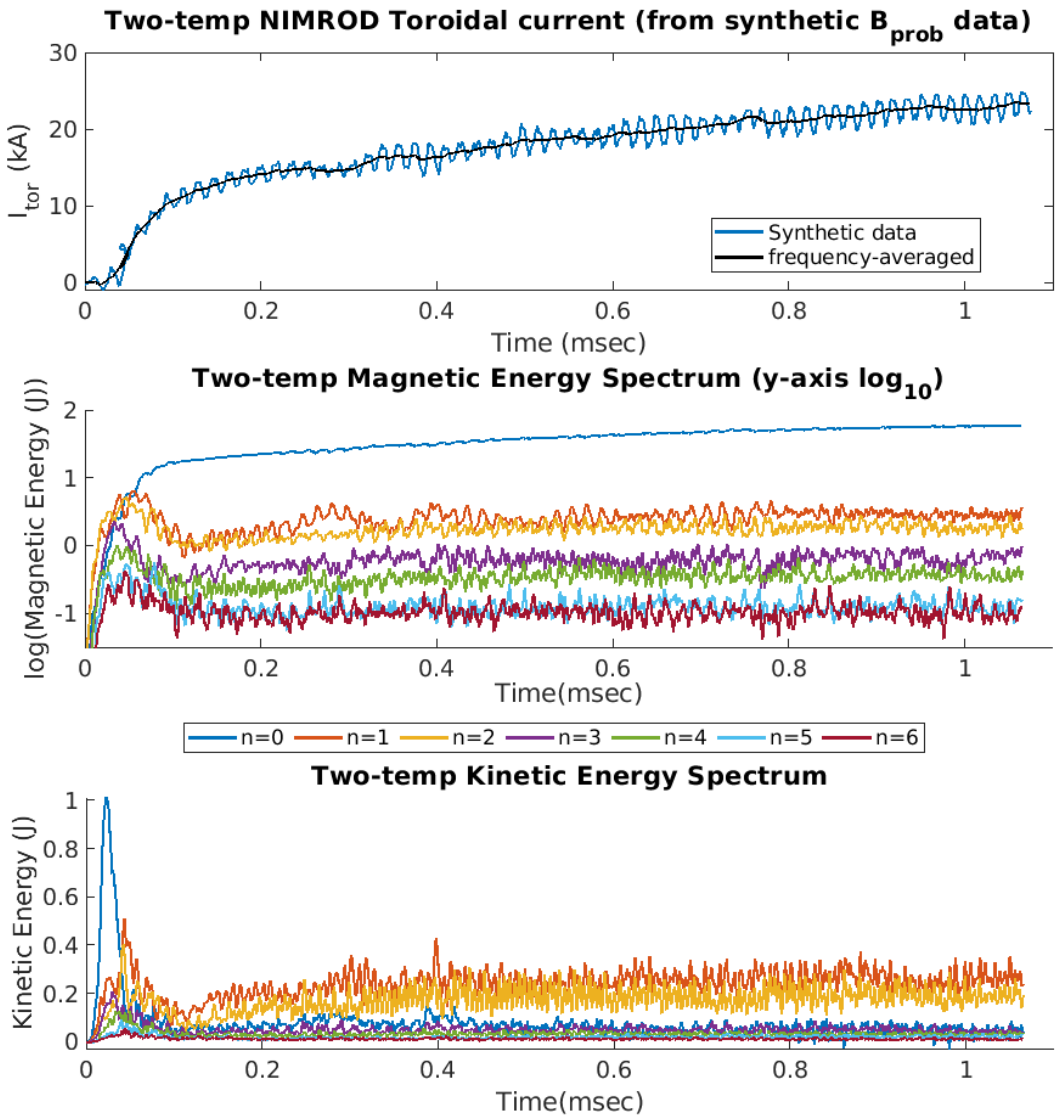

Figure 3.22: Toroidal current evolution and volume-integrated magnetic field Fourier mode energies for the two-temperature simulation of shot 180816020.

BD Analysis of simulations

NIMROD natively provides the volume-integrated energy of each Fourier mode of the magnetic field, however these are measurements of the total magnetic fields, internal and external. The experimental surface probes are limited to measuring the magnetic field of the spheromak edge, and to get comparable measurements the field measurements from equivalent positions in the simulation must be used, a "synthetic" measurement. Synthetic surface probe and IMP data from simulations of shot 180816020 were examined using the biorthogonal decomposition analysis. This provides both a means of comparison to the activity actually observed and calculated in the experiment as well as correlating that observed activity to either pure magnetic instabilities or pressure and magnetic influences.

The equilibrium and injector subtracted activity of the zero-β simulation as seen in Figure 3.21 does not reveal any low frequency intermittent $n = 2$ activity, nor does it show the elevated $n = 2$ background that positive shots reveal. Though there is some intermittent activity, it is broadband spectrally and does not elevate beyond the background level at many places. In both the single and two temperature simulations, an elevated $n = 2$ δB not associated with the equilibrium or injectors is observed, consistent with the non-equilibrium $n = 2$ observed in data from positive toroidal current shots, such as 180816014. The $n = 2$ energy in the single temperature subtracted spectra seen in Figure 3.22 have superficially more activity than in the two-temperature simulation seen in Figure 3.23; this may be indicative of the activity being tied more to ion fluid effects than electron as the noisy features in the single temperature may due to Ohmic heating fluctuations. All the simulations, including the zero-β, show a large amount of $n = 3$ in the equilibrium after the injector energy is subtracted off. During the periods of oscillating current activity, in both single and two-temperature simulations, the plasma generated $n = 1$ energy will briefly spike or broadband magnetic activity in general will also spike indicating that these events may be associated with the conversion of poloidal flux to toroidal flux.

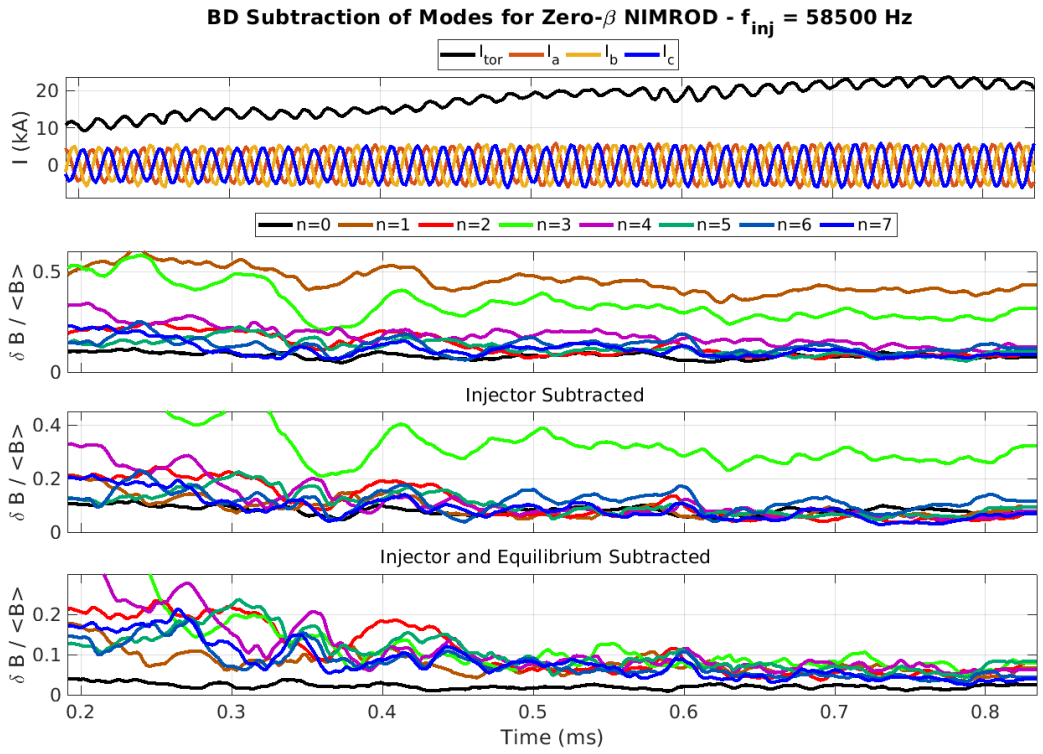

Figure 3.23: BD analysis plot for the zero-β simulation, made using magnetic field data from probe locations in the simulation domain and performing the same subtraction of the biorthogonal modes for injector and equilibrium fields.

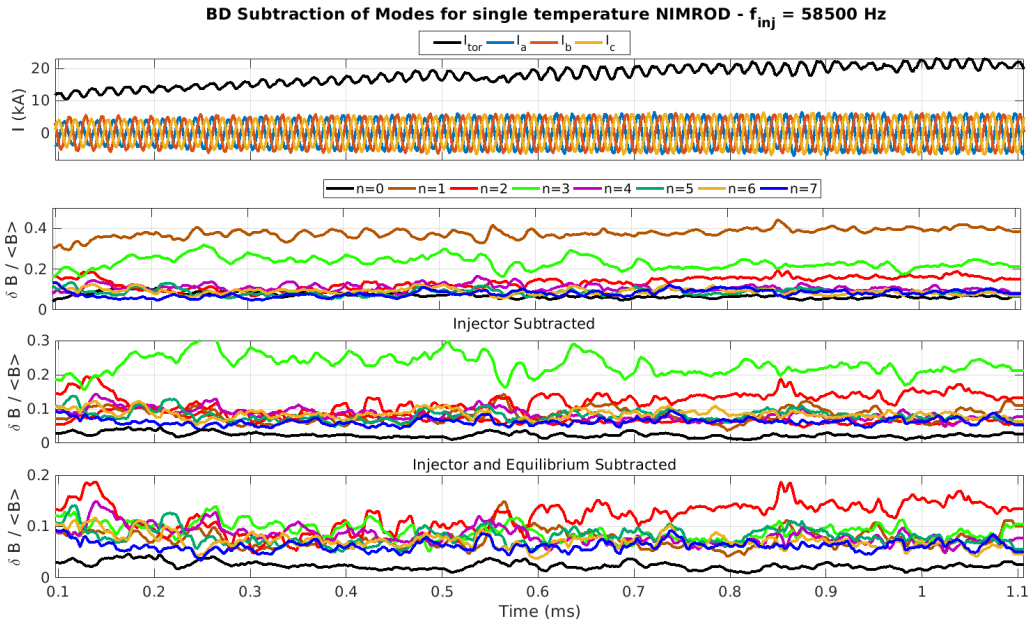

Figure 3.24: BD analysis plot for the low diffusivity single temperature simulation, made using magnetic field data from probe locations in the simulation domain and performing the same subtraction of the biorthogonal modes for injector and equilibrium fields.

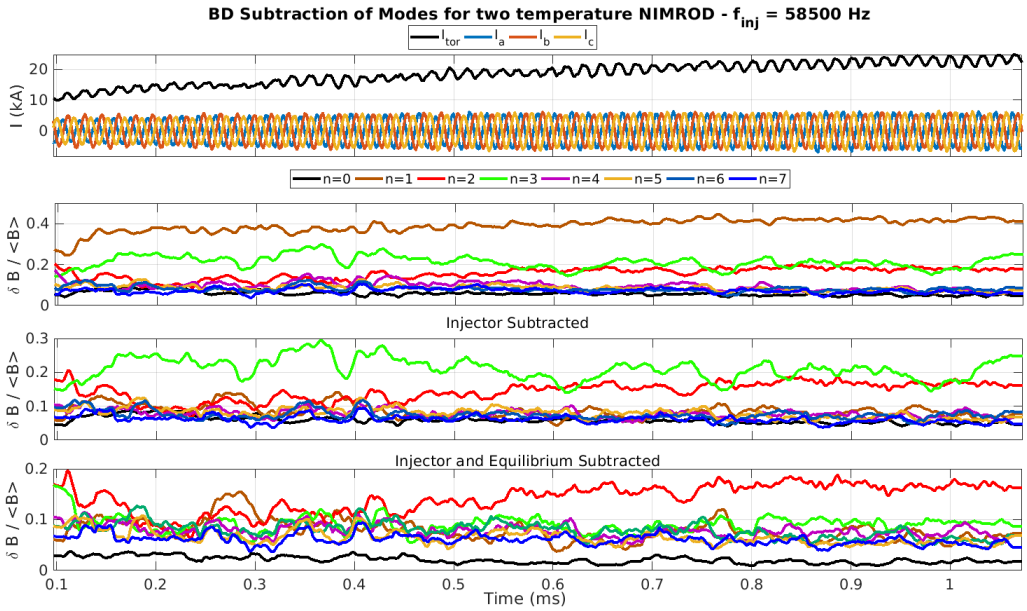

Figure 3.25: BD analysis plot for the low diffusivity two temperature simulation, made using magnetic field data from probe locations in the simulation domain and performing the same subtraction of the biorthogonal modes for injector and equilibrium fields.

Finite-β density evolution

The single and two-temperature models allow the evolution of density and temperature, and with the previously discussed importance of β limits in diagnosing $n = 2$ instabilities, it is important to examine the evolution of those quantities. In the HIT-SI3 experiment, the single-chord Far-Infrered interferometer (FIR) was used to measure the average density. The synthetic FIR traces, the line-averaged measurements of density in the computational domain along the same path as the experimental FIR chord for the single temperature simulation can be seen in Figure 3.26, and for the two temperature simulation in Figure 3.27. Also displayed in the plots are the volume-averaged $< \beta > \equiv \frac{2\mu_0 \int_V nkT}{\int_V B^2}$, for both of the density and temperature-evolving simulations. In addition to injector-frequency oscillations, lower frequency oscillations in which the line-integrated density varies by as much as 20-25% can be observed in the synthetic FIR signals in both finite-β simulations. The $< \beta >$ in both simulations settles decreases steadily after the relaxation event as the spheromak fields build and seem to tend towards steady-state values. Interestingly, the two-temperature simulation exhibits a higher $< \beta >$, indicating the adjustment to the heat conduction from including the electron physics may be at play (using the individually-calculated species heat fluxes rather than the more pessimistic quantity from either species for the single-temperature). While the $< \beta >$ from each simulation does not vary drastically after a certain time, the low-frequency density oscillations persist throughout the simulation. This interesting signal warrants investigating the internal activity of the spheromak during those periods for possible explanations for the experimental behavior.

3.3.2 Investigation of simulated internal profiles

The changes to internal profiles such as pressure and λ are key for determining the nature and evolution of instabilities, but obtaining a complete picture of these profiles from experimental measurements is usually impossible. One benefit of simulations is that the data sets within the domain are complete and allow investigation of quantities not easily

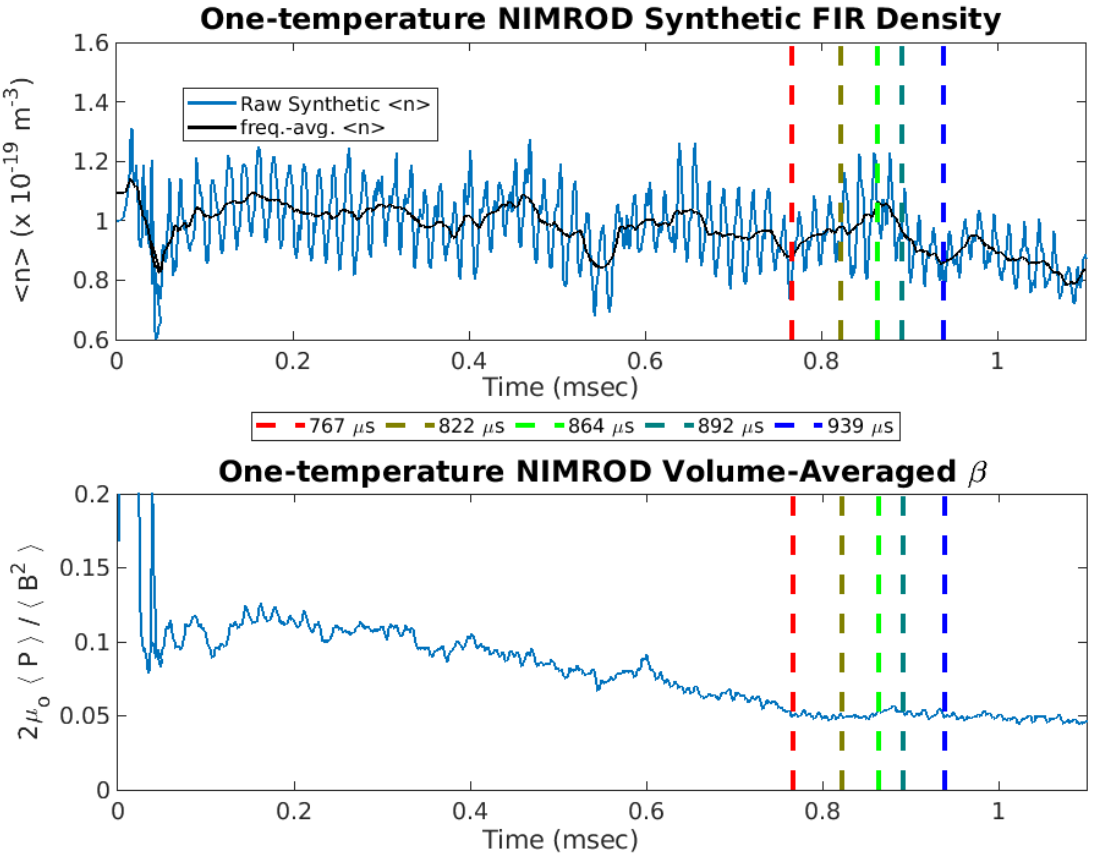

Figure 3.26: Time evolution of synthetic chord-averaged FIR density from single temperature simulation with injector-period smoothed trace to better visualize low-frequency oscillation. Colored vertical lines represent different times chosen along different phases of a single density oscillation used to generate the profiles seen in Figure 3.28

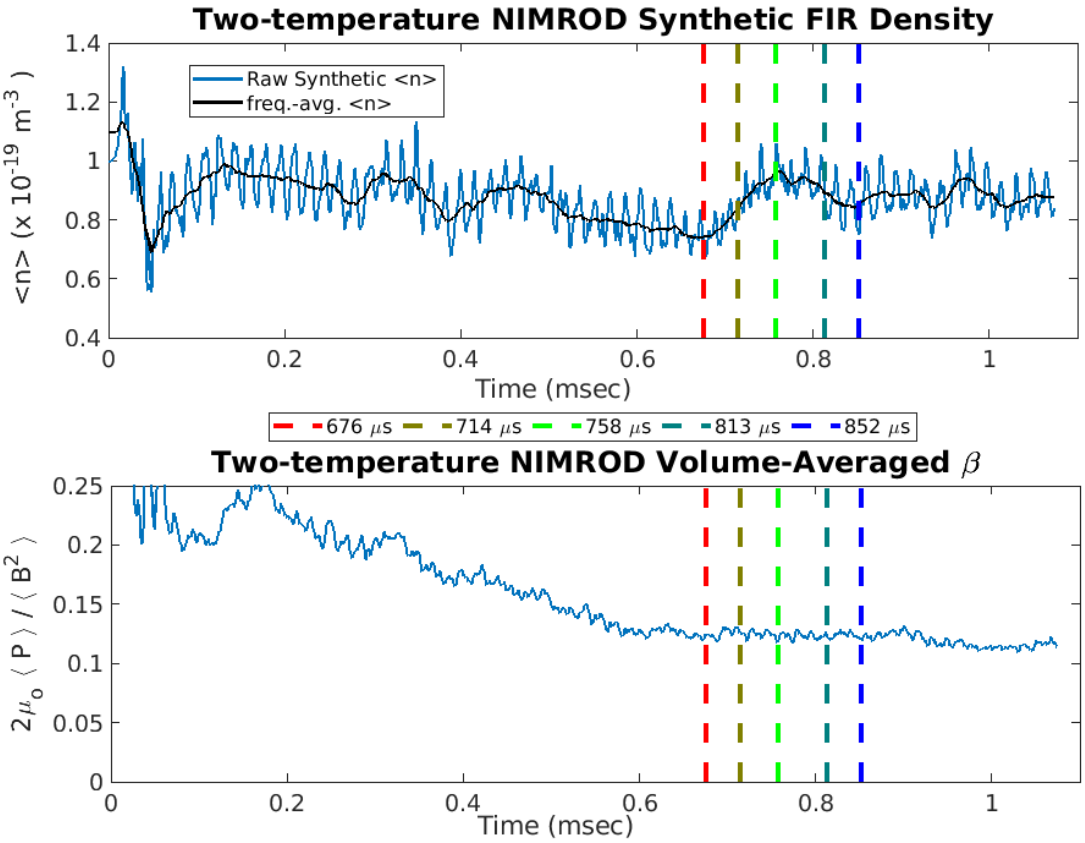

Figure 3.27: Time evolution of synthetic chord-averaged FIR density from two temperature simulation with injector-period smoothed trace to better visualize low-frequency oscillation. Colored vertical lines represent different times chosen along different phases of a single density oscillation used to generate the profiles seen in Figure 3.29

measured in experiment. The toroidally-averaged profiles and volume-averaged quantities that will be presented next were taken from several time points (as marked in Figures 3.26 and 3.27) during which the density and $n = 2$ energy underwent a low-frequency fluctuation event. Examining the variation in quantities such as toroidally-averaged λ, pressure, and volume-averaged β may shed light on the origin and evolution of the plasma-generated $n = 2$ events.

Pressure, λ, and β variation

HIT-SI3 is a 3D dynamic system, so a complete description of the internal activity would require careful analysis inside the entire domain. While this is feasible it is inconvenient, and instead averaged profiles and quantities can be used to gather information about physical trends. Two 3D quantities, pressure (knT) and λ, are both time-averaged at the injector frequency and then averaged over the toroidal direction in order to get what could be considered a profile in the RZ plane. Values from these averaged profiles are then taken at radial points along the vertical position of the spheromak's current centroid to make the profiles for λ and pressure seen in Figure 3.28 and Figure 3.29. Several time points along an FIR density oscillation in the single and two temperature simulations are chosen (as seen by the colored lines in Figure 3.17 and Figure 3.18), and at each time point the averaged profile discussed above is plotted. In this way, a general idea of the current and pressure profile evolution of the spheromak can be evaluated. These profiles are also compared against the time traces of the volume-averaged β and the non-axisymmetric magnetic mode energy within the time window of the chosen oscillation.

The single temperature simulation seems to have a straightforward evolution during one of these oscillations, with the λ profile starting relatively hollow, flattening, peaking, and hollowing out again as the pressure peaks with the FIR-measured density and the β along with it. Magnetic energy seems to first excite primarily in the $n = 1$ mode and towards the end of the event $n = 2$ gets excited. The order of this energy cascade is suggestive of a profile rearrangement converting axisymmetric to non-axisymmetric energy, followed by a period of

heating and increased β which could trigger $n = 2$ pressure-related instabilities as the current peaks. The behavior in the two temperature simulation is slightly different, with the λ profile fluctuating and magnetic energy fluctuations being seen in the $n = 1, n = 2$ and $n = 3$ modes with a period of quiescence around the time of falling FIR density from the peak. During this time volume-averaged β fluctuates rather than peaks and falls as the FIR-measured density does. Though the pressure profile peaks later in time, the β does not significantly increase during this time which suggests increased field strength to lower the value of β. A possible explanation for the behavior seen in both shots is reconnection-driven activity, converting a buildup of non-axisymmetric magnetic energy to spheromak energy. During the conversion of non-axisymmetric ($n = 1, 2, 3$) energy to the $n = 0$ spheromak energy, the λ profile would try to arrange closer to the flat profile of the Taylor state and increased toroidal current would lead to a buildup of pressure and β due to Ohmic heating and increased confinement. To verify this explanation will require more simulations at different conditions to establish if this behavior is specific to 120-degree phased shots at this frequency, or is reproducible in other shots under other conditions. Additional comparisons to experimental density-measuring diagnostics aside from the FIR - namely Ion Doppler Spectroscopy (IDS) and Langmuir probe measurements - will also be needed to verify that this behavior is indeed being reproduced in the experiment.

Profile variation compared to HIT-SI high-frequency simulation

High frequency, single-temperature simulations of HIT-SI were carried out by K. Morgan as part of the investigation of the $n = 2$ activity. This simulation used the highest operational injector frequency from HIT-SI, 68 kHz, and reached a current gain of 3.8, which is roughly within the same parameter space as the previously exanimed HIT-SI3 shots and simulations.

Profiles plots similar to the ones generated in the previous subsection are displayed in Figures 3.30 and 3.31, however both are take from different times during the same single-temperature simulation. These are posited to represent two different events involving $n = 2$ activity.[42] In Figure 3.30, a spike in $n = 2$ activity occurs. The plotted profiles suggest

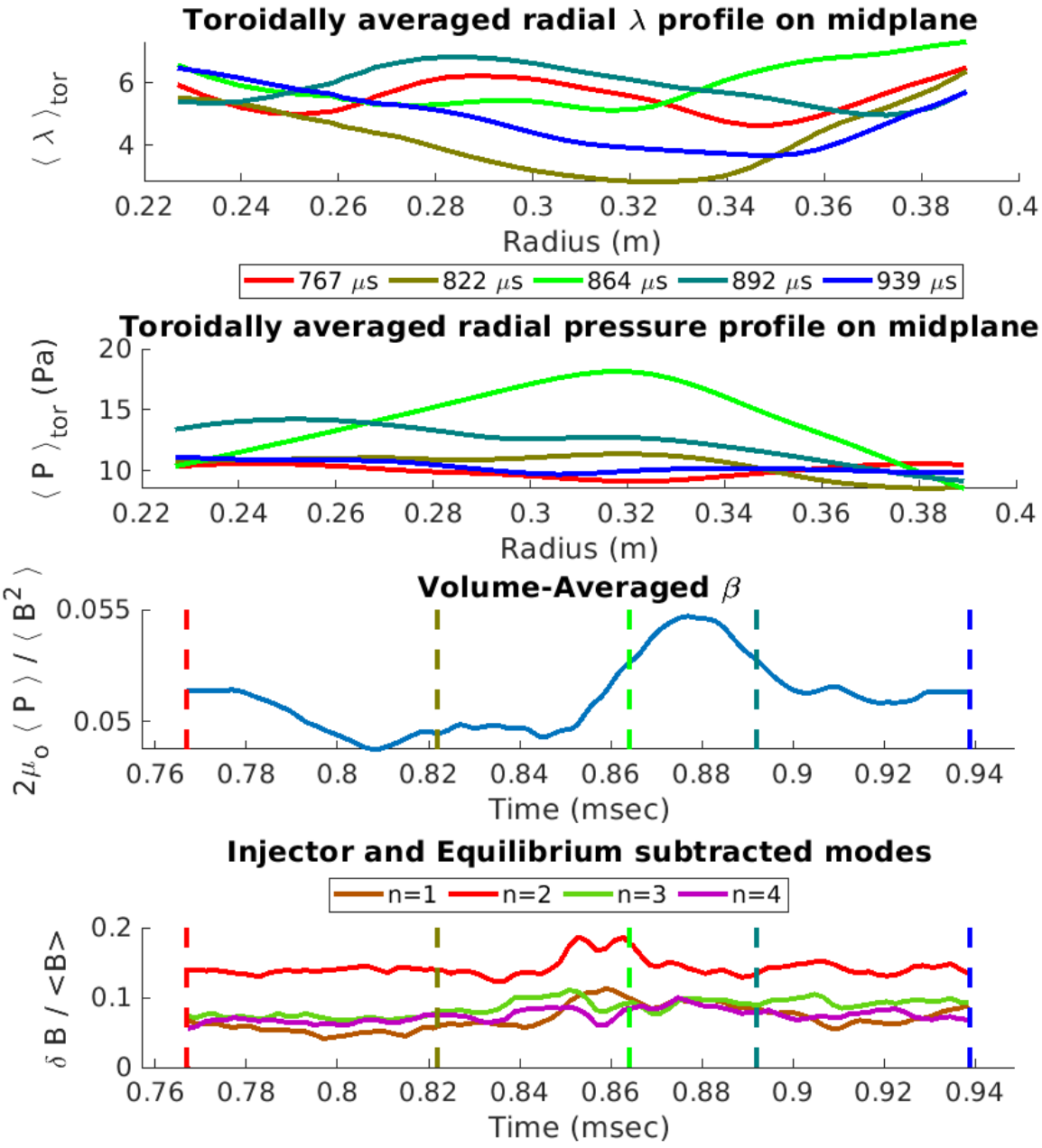

Figure 3.28: The ordinate of top two plots display profiles of the 3D scalars λ and pressure for the single temperature 180816020 simulation, first toroidally averaged and then taken at the z location of the magnetic axis, plotted as a function of radius, with each color representing a different moment in the simulation. The bottom two plots are time traces of the volume-averaged β and plasma-generated mode magnitude of selected top modes, plotted during the time period between the first and last time steps chosen for the profiles.

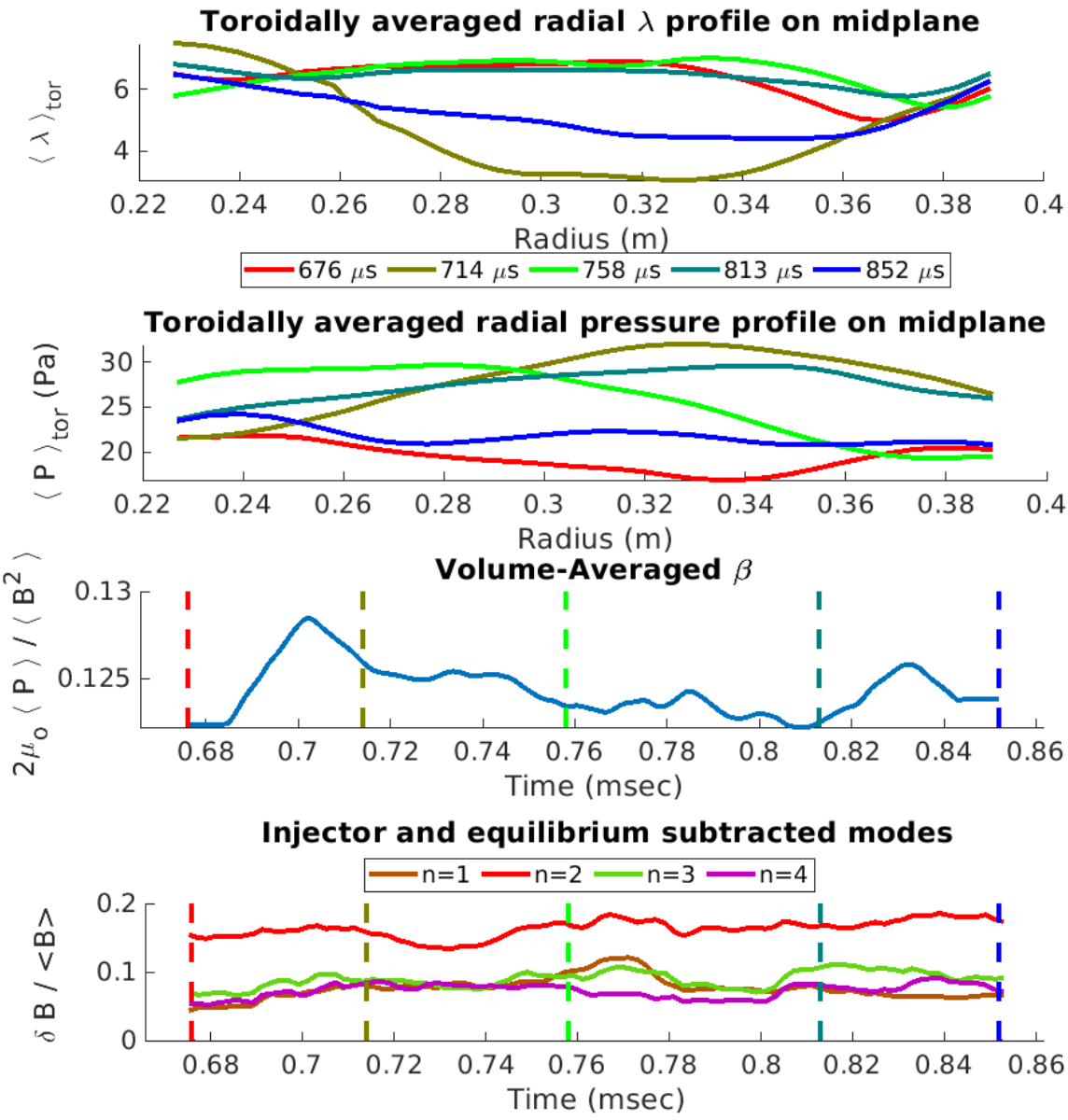

Figure 3.29: The ordinate of top two plots display profiles of the 3D scalars λ and pressure for the two temperature 180816020, first toroidally averaged and then taken at the z location of the magnetic axis, plotted as a function of radius, with each color representing a different moment in the simulation. The bottom two plots are time traces of the volume-averaged β and the plasma-generated mode magnitude of selected top modes, plotted during the time period between the first and last time steps chosen for the profiles.

this event seems to be a kind of current rearrangement. Before the event the plasma has a hollow lambda and peaked pressure profile, then following the event this has reversed, with a peaked λ and hollow pressure profile. However, the volume averaged β changes little overall due to the pressure on the magnetic axis reducing while pressure 5-10 cm outboard from magnetic axis was increasing. While not conclusive, this type of behavior is present in pressure-driven interchanges, and bears some resemblance to the behavior seen in the two-temperature HIT-SI3 simulation's $n = 2$ event, the only prominent difference being the flattening of the λ profile that occurs on HIT-SI3.

In Figure 3.31 a different behavior is displayed. Instead of preaking, the pressure has built up and is released. Before the event the spheromak λ profile is hollow and the pressure profile is peaked, during the event the pressure flattens, and lambda has a second flat region inboard of the magnetic axis. During this period, the volume-averaged β increases slightly before decreasing. The overall λ is hollow during the event. This behavior, curiously, resembles the single-temperature simulation $n = 2$ event in Figure 3.28, which also shows a spike in volume-averaged β and a peaking of the pressure profile; again the only substantial difference is in the λ variation. The appearance of similar behavior in HIT-SI simulations using a high f_{inj} close the the 58.5 kHz of the high-frequency HIT-SI3 campaign is encouraging, as it shows some consistency in the physics of the model. If in both HIT-SI and HIT-SI3, there is profile rearrangement and heating activity causing elevated pressure and β which triggers these $n = 2$ modes, their presence in both devices means NIMROD is capturing some aspect of the spheromak dynamics that has been documented experimentally. It must be again noted, however, that the presented data did not solidly indicate the presence of pressure-driven $n = 2$ modes, and that these is substantial disagreement between the simulation and experiment, as the next subsection will cover.

3.3.3 Comparison to experimentally-measured quantities

Inspection of the results from the NIMROD simulations presented so far readily present several areas of disagreement between all of the simulated shots and the experimental shot

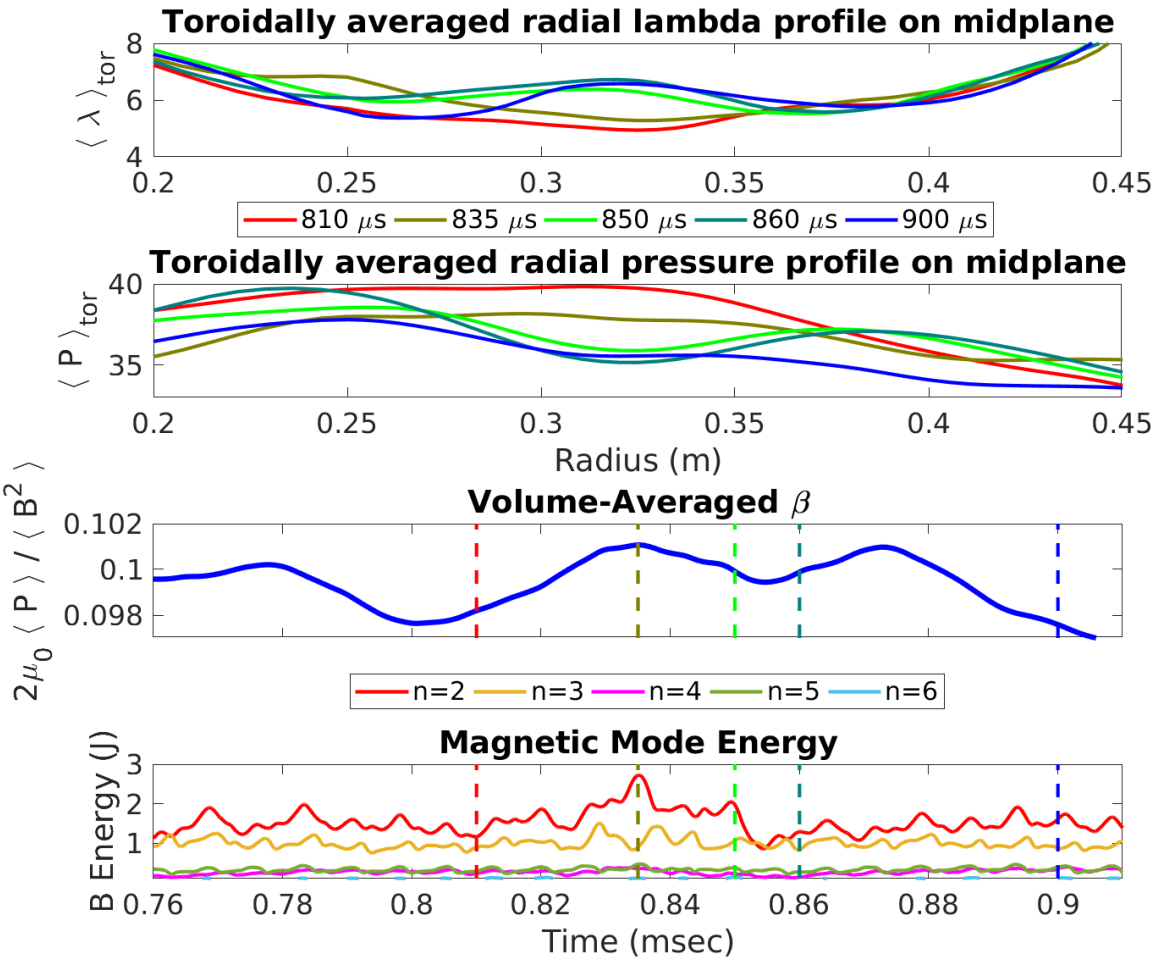

Figure 3.30: Pressure and λ profile variation with β evolution for the spike in $n = 2$ activity observed in the single-temperature NIMROD simulation of HIT-SI done by K. Morgan.

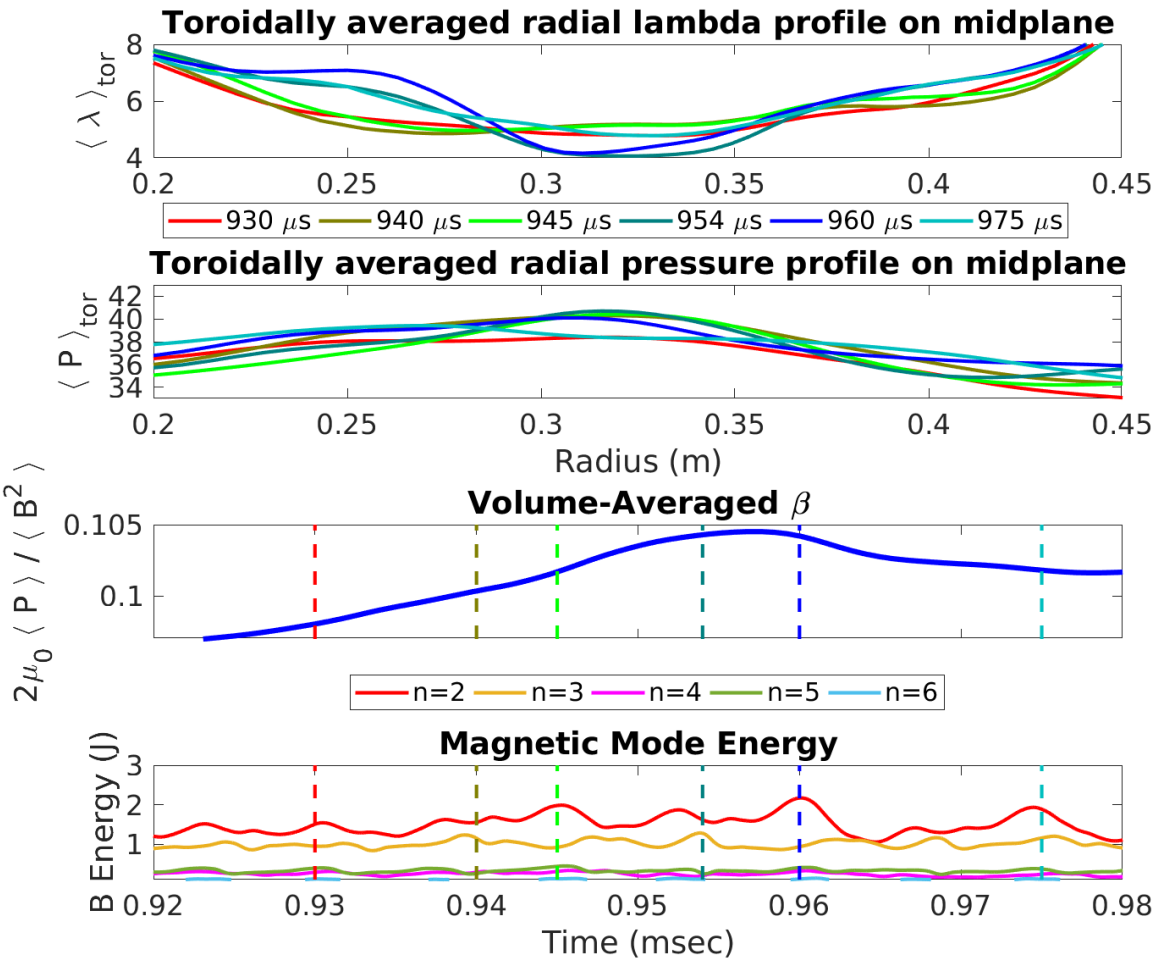

Figure 3.31: Pressure and λ profile variation with β evolution during a second type of magnetic activity, with mixed $n = 1$ and $n = 2$ fluctuations, observed in the single-temperature NIMROD simulation of HIT-SI done by K. Morgan.

180816020; the NIMROD simulations have a positively-oriented toroidal current whereas the experimental discharge was negative current, and the equilibrium and injector-subtracted Fourier spectra do not have the same intermittent $n = 2$ events, but but rather a fluctuating background. To understand exactly the extent of disagreement and how applicable the simulation results may be to understanding the experiment, several diagnostic and sythetic signals will be compared. Due to incomplete data sets from some diagnostics such as the FIR, shots from that same experimental campaign such as 180904015 will also be used for comparison.

I_{tor} and current centroid position

Direct comparison of the toroidal current evolution between the zero-β, single temperature, and two temperature simulations of 180816020 against the absolute value of the experimental toroidal current (time-shifted to match the experimental formation time) can be seen in Figure 3.32. All three traces display some sort of low-frequency activity, however the oscillations in the zero-β current are much more pronounced than in the experiment or in the finite-β simulations, indicating that there may be some pressure-related effects in the dynamics of these current sawteeth.

An area of disagreement between experiment and simulation is the position of the current centroid as calculated by the surface probes. The current centroid, an experimentally-derived quantity closely related to the poloidal O-point (the magnetic axis), is the location of the maximum toroidal current magnitude as calculated by the weighted averaged between the $N = 16$ discrete surface probe measurements:

$$R_{centroid} = \frac{\Sigma_N B_{pol,n} R_n}{\Sigma_N B_{pol,n}} \tag{3.5}$$

This formula yields the radial position, whereas the vertical position is calculated in a similar fashion. The calculated centroid position, averaged between the four sets of poloidal arrays, is plotted over time for shot 180816020, the zero-β, single temperature and two

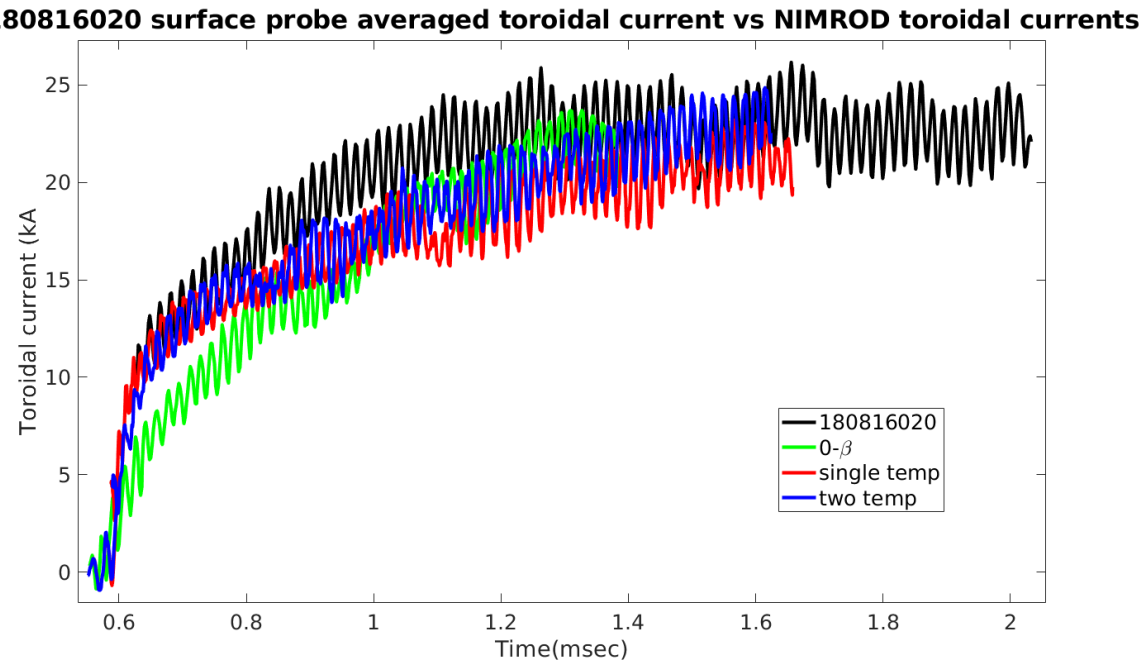

Figure 3.32: The magnitude of the toroidal current evolution from HIT-SI3 58.5 kHz shot 180816020 compared to the zero-β, single and two temperature NIMROD simulations of the shot, time-shifted to match the experimental discharge's evolution. The convergence of the two-temperature simulation to the experimental current value is noted.

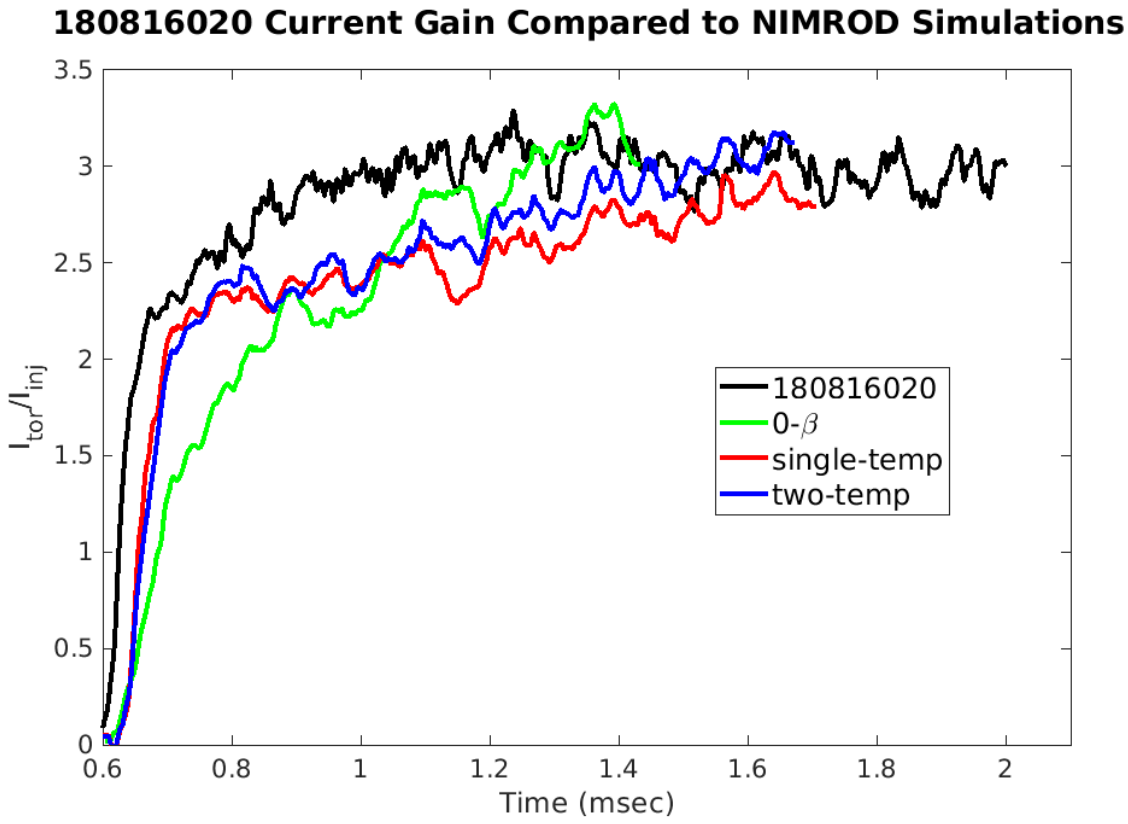

Figure 3.33: The current gain over time from HIT-SI3 58.5 kHz shot 180816020 compared to the zero-β, single and two temperature NIMROD simulations of the shot. The convergence of the two-temperature simulation to the experimental current value is noted.

temperature NIMROD simulations in Figure 3.34. The synthetic data from all simulations show the centroid shifted inwards by several centimeters compared to its position in the experiment. This is indicative of a physical disagreement between the experimental and simulated sustained equilibrium, which could be due to incorrect boundary conditions or incorrect/missing physics in the evolution. Specific model changes that could improve physical agreement will be discussed further in Chapter 5. Closer inspection shows that the oscillation magnitude of the two temperature simulation matches the experiment better than the single temperature or zero-β simulations in the same parameter space, in addition to the two temperature being shifted farthest outward and closest in position to the experiment. This is an encouraging sign that the two temperature model of HIT-SI3 in NIMROD is a model with improved agreement, and that further development and adjustments to the model can yield even more accurate results. One interesting feature captured in the two temperature model, and not in others, is the presence of periods of sudden and brief outward shift followed by an extended retreat of the centroid radially inward. This is also seen, though comparatively later in time, in the experimental trace. These shifts in the centroid position correspond roughly with the periods of non-equilibrium mode activity as well as the current and density oscillations, in both the two temperature model and the experimental shot, and will be investigated more thoroughly. The vertical positions of the current centroids measured from simulation are substantially more downward-shifted compared to the experimentally-derived position. The zero-β and single-temperature simulations are both displaced downards by up to 10% of the minor radius (2-3 cm), whereas the two-temperature simulation's vertical postion appears to be converging with the experimentally-derived quantity; this is another indication of the contribution accurately including the two-temperature dynamics can make towards better agreement. It is important to note that in every case, including experiment, the vertical centroid positions are shifted downwards from the flux conserver midplane, a factor that is likely affecting the quality of reconstructions from PSI-Tri as seen in Section 3.2 and will need to be taken into account in future equilibrium reconstruction work.

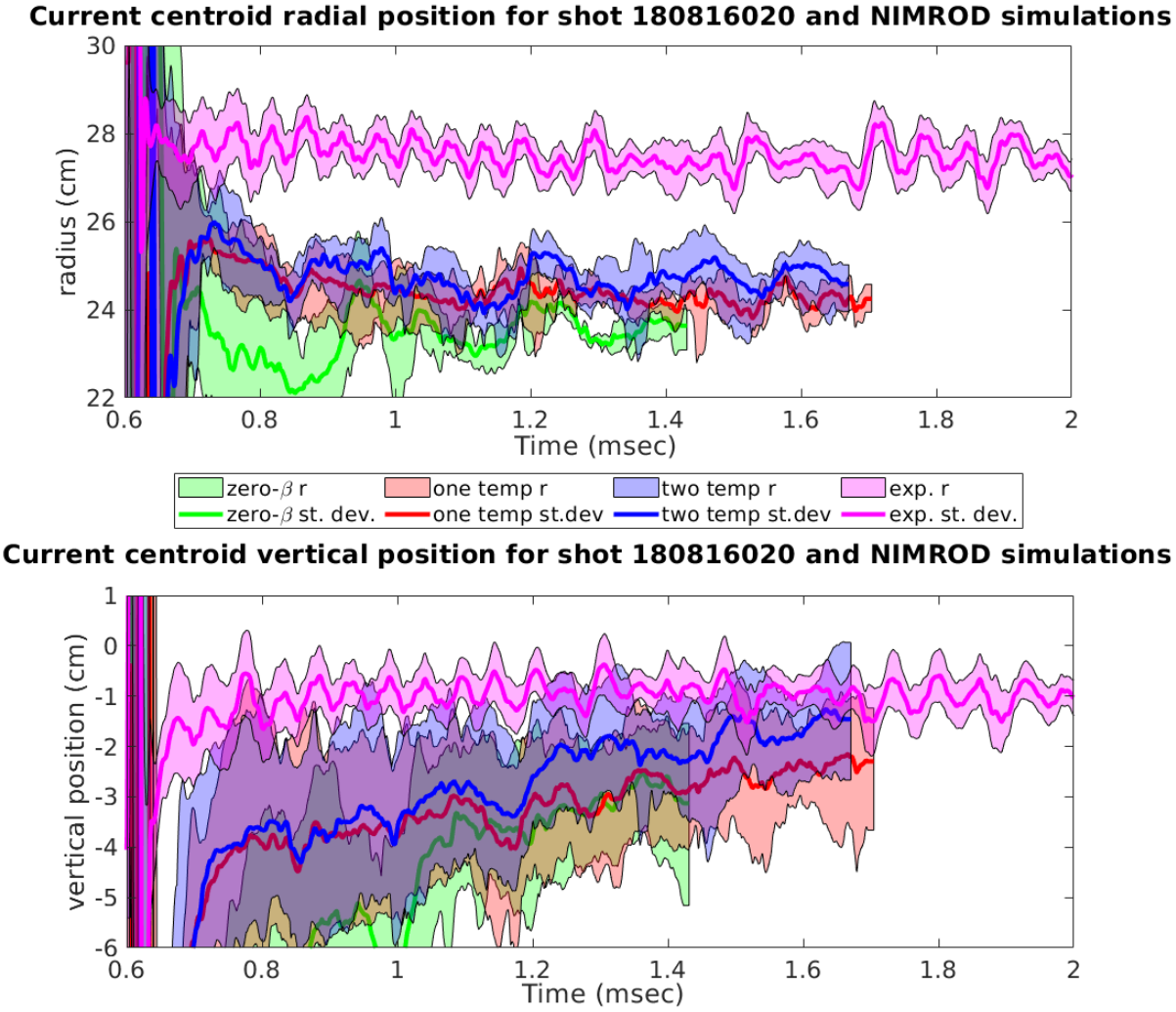

Figure 3.34: The current centroid radial (top) and vertical (bottom) position of shot 180816020 as calculated by Equation 3.5 for shot 180816020 and the zero-β, single, and two temperature NIMROD simulations of the shot.

Comparison of measured δB

Comparing the edge-measured mode spectra of the experimental shot 180816020 and the NIMROD simulations is necessary to understand how applicable any behavior observed in the "synthetic" probe measurements, and other simulation quantities, is to the observed behavior from experimental quantities. While the BD-subtracted spectra from the simulations are qualitatively different by inspection, the directly-measured quantities might show more agreement and are worth examining. The top plots of Figure 3.35, Figure 3.36, and Figure 3.37 compare the first four measure modes ($n = 0$ through $n = 3$) from shot 180816020 to the synthetic probe-measured modes from the zero-β, single-temperature, and two-temperature simulations. None of the three models replicated the spectra measured from experiment, with noticeably higher edge $\frac{\delta B}{B}$ in the simulations; this is attributed to higher edge currents in the simulations due to the increased wall temperature. Also interesting is the increased proportion of $n = 3$ energy in the simulations compared to the experiment, which has higher $n = 1$ and $n = 2$ than $n = 3$. The $n = 3$ mode is not directly imposed by the injectors, but can arise from non-linear interactions between the injectors and spheromaks. It is only in the two-temperature simulation that the synthetic $n = 2$ and $n = 3$ approach similar levels, which is still not the same as the higher magnitude of $n = 2$ than $n = 3$ in experiment.

The surface probe measurements are predominately of the edge fields of the spheromak, so it is unclear whether the probe-measured mode magnitudes reflect the overall proportion of the mode within the internal spheromak fields or are local to the edge. To gain insight on this, the bottom plots of Figure 3.35, Figure 3.36, and Figure 3.37 compare the synthetic surface probe-derived edge modes (for the first three non-axisymmetric modes $n = 1$, $n = 2$, $n = 3$) to the total proportion of the mode in the full simulation volume; this is simply derived by taking the mode energy, which is output natively from NIMROD, and taking the square root to find the magnitude of the field ($|B_n| = \sqrt{2\mu W_{B,n}}$). The $n = 0$ energy is omitted from this plot due to the overwhelming dominance of the $n = 0$ energy within the spheromak volume compared to the edge. All three models show the total proportion of

each mode within the volume differs substantially from the modes calculated using synthetic surface probe measurements, the biggest point of differentiation being the lower $n = 3$ presence according the the volume-integrated energy compared to the proportion detected. While in the zero-β simulation all three modes converge to roughly the same δB, the single and two-temperature simulation show the $n = 1$ and $n = 2$ are present at nearly twice the levels of the $n = 3$. This unexpected result raises questions about the efficacy of using surface measurements to try and record activity influenced by internal dynamics, but this will be discussed in later Chapters.

Comparison of FIR measured density

Comparisons of the FIR trace of shot 180904015 with the single temperature NIMROD simulation is seen in Figure 3.38a, and with the two-temperature simulation in Figure 3.38b. In the previous section, it was apparent the line-integrated density in experimental shot not only oscillated at the injector frequency, also at lower frequencies with Fourier power spectrum spikes at 4-6 and 10-15kHz. When plotted against the experimental trace, despite using a different phasing it is clear the sythetic FIR density from both simulations exhibits similar behavior. The continuous fluctuation of density as measured using the FIR chord is both a good sign of NIMROD capturing experimentally-accurate dynamics and evidence that these lower frequency oscillations are may be the result of the profile rearrangement and other behaviors observed in simulation.

3.4 Conclusion

The BD mode subtraction analysis that was useful in proving stability to the $n = 1$ mode in HIT-SI was used to discover and characterize plasma-generated $n = 2$ modes in high-frequency HIT-SI3 shots from the summer of 2018. Further investigation using this technique revealed these $n = 2$ fluctuations were a persistent feature of many HIT-SI3 shots, even at lower injector frequencies. Experimental evidence of global variation in HIT-SI3 spheromaks due to the plasma-generated $n = 2$, from diagnostics such at the Internal Mag-

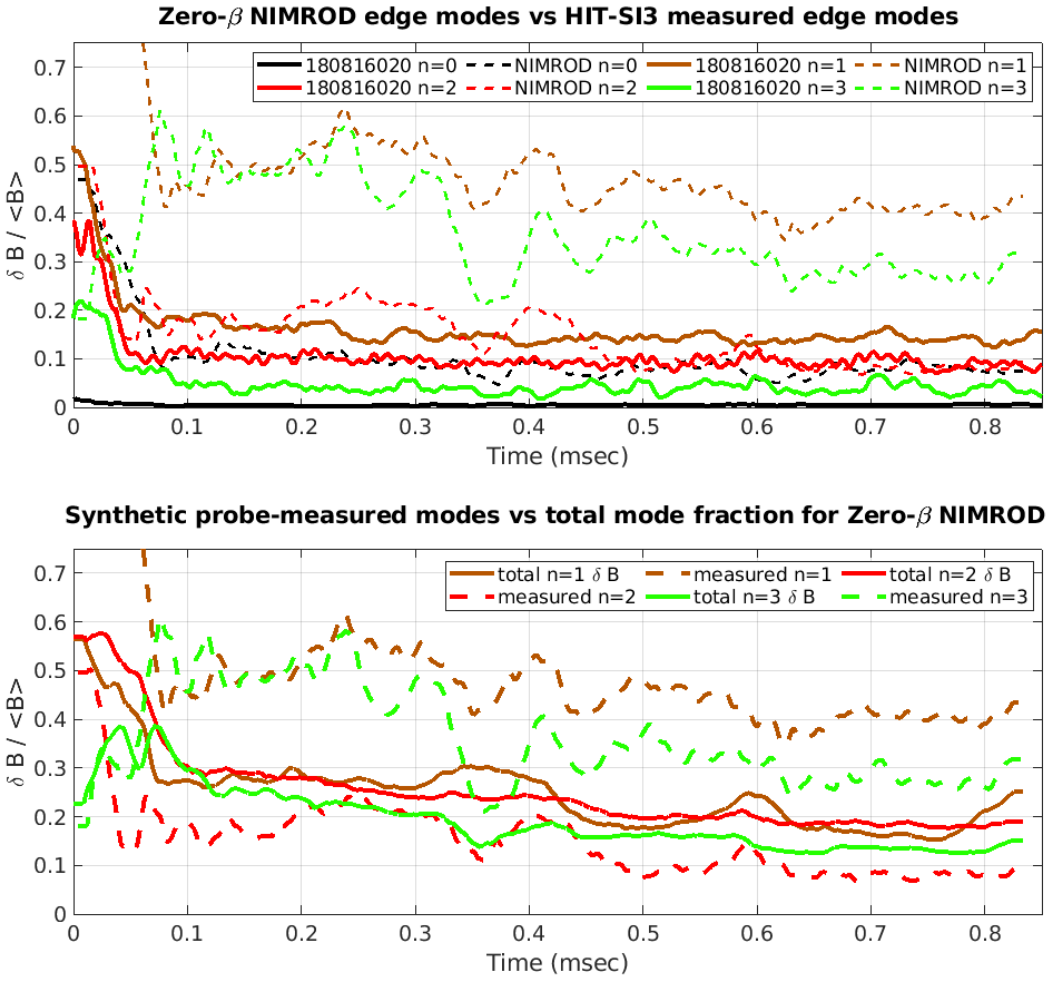

Figure 3.35: Measured modes $n = 0$ through $n = 3$ from synthetic probes in the zero-β NIMROD simulation of 180816020 compared to the experimental measurements (top), and edge-measured modes $n = 1$ through $n = 3$ compared to volume-integrated mode magnitudes.

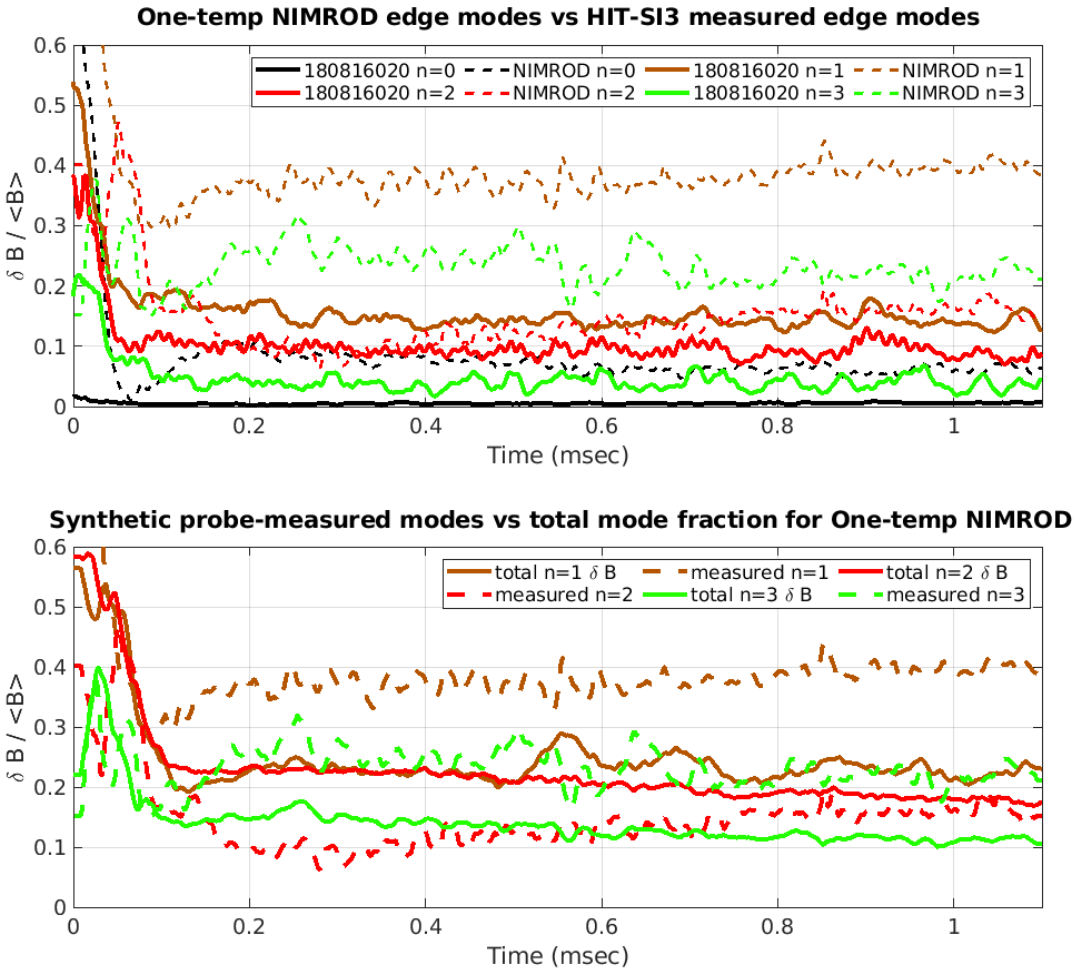

Figure 3.36: Measured modes $n = 0$ through $n = 3$ from synthetic probes in the single-temperature NIMROD simulation of 180816020 compared to the experimental measurements (top), and edge-measured modes $n = 1$ through $n = 3$ compared to volume-integrated mode magnitudes.

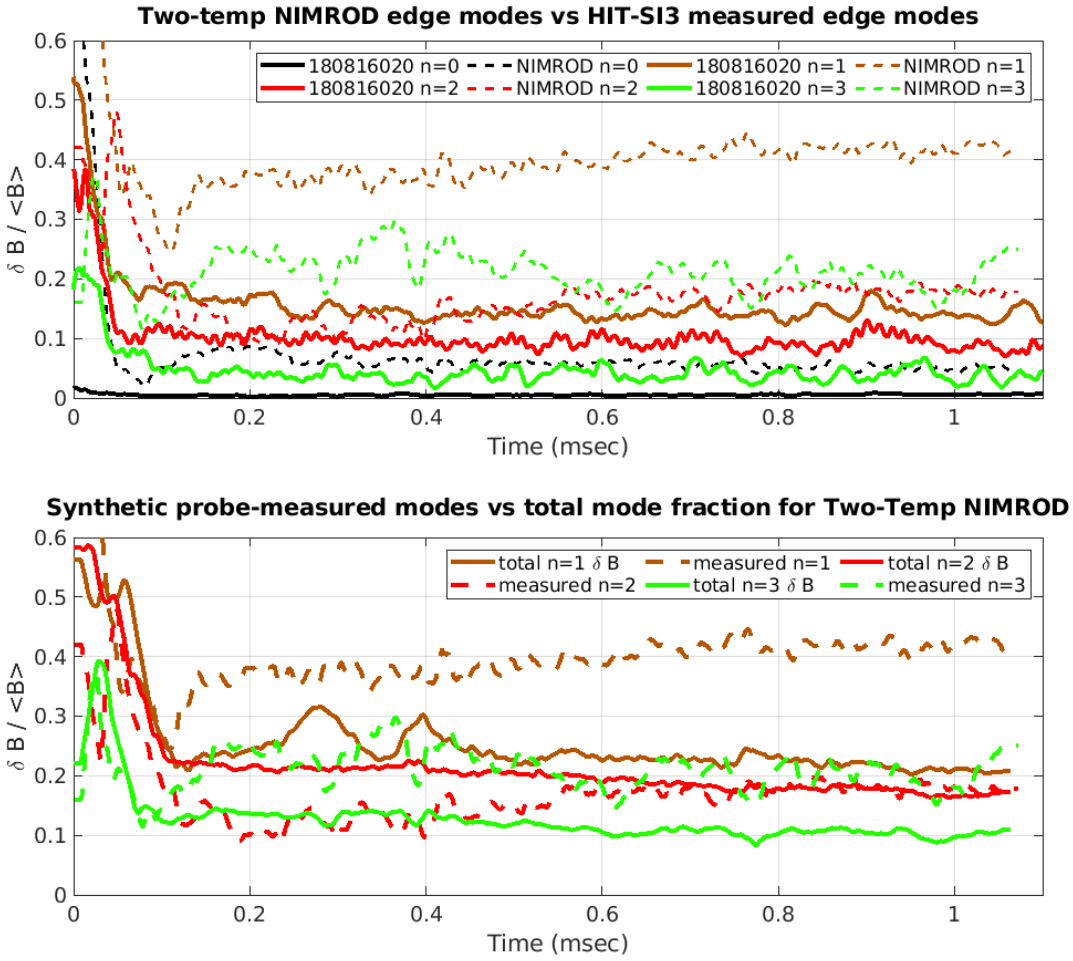

Figure 3.37: Measured modes $n = 0$ through $n = 3$ from synthetic probes in the two-temperature NIMROD simulation of 180816020 compared to the experimental measurements (top), and edge-measured modes $n = 1$ through $n = 3$ compared to volume-integrated mode magnitudes.

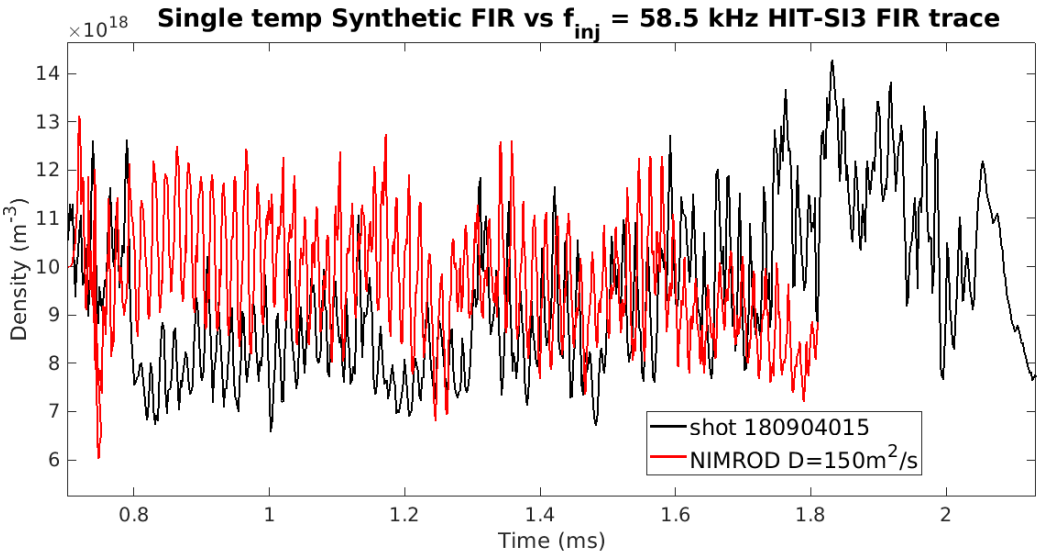

(a) FIR trace of shot 180904015 (black) compared to $D = 150\frac{m^2}{s}$ single temperature NIMROD synthetic FIR data (red). 180904015 is used due to a lack of FIR data from shots on the day of 180816020.

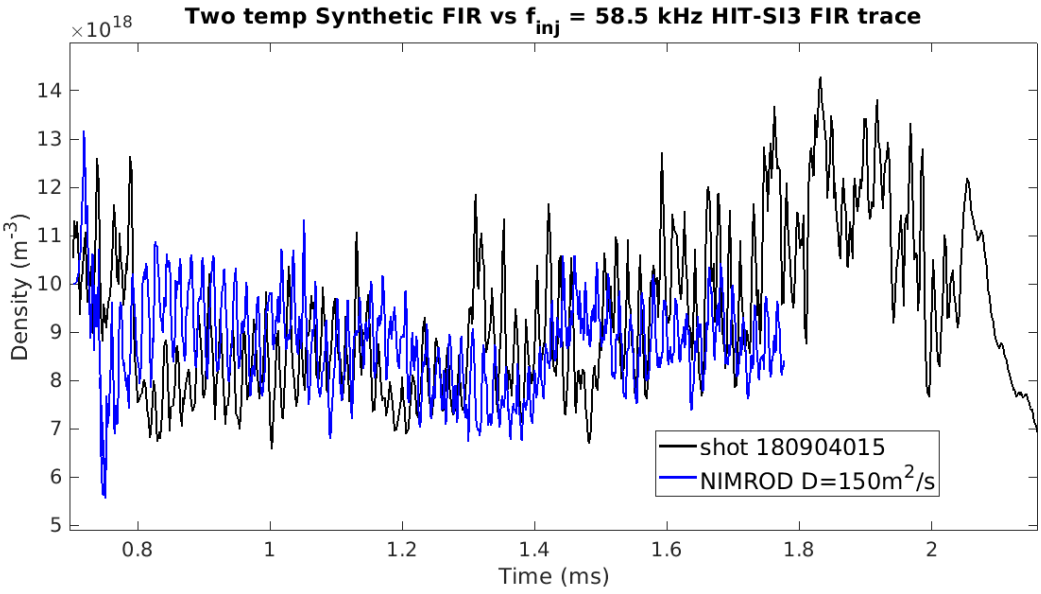

(b) FIR trace of shot 180904015 (black) compared to $D = 150\frac{m^2}{s}$ two temperature NIMROD synthetic FIR data (blue).

Figure 3.38: The experimental FIR trace of shot 180904015, a 58.5 kHz HIT-SI3 shot, compared to the synthetic FIR trace from the single-temperature NIMROD simulation of HIT-SI3 (a), and the two-temperature simulation (b).

netic Probe and the Far-Infrared Interferometer, prompted investigation of this phenomena using numerical tools. Attempts to perform equilibrium reconstruction using the PSI-Tri code with a linear flux function yielded poor results compared to the attempts made previously with HIT-SI data. A further step was simulating shot 180816020, a typical example of a shot displaying the $n = 2$ fluctuation, with the xMHD software NIMROD and using the experimental injector waveforms as inputs. The results of the simulations differed from the experimental shot in several important respects, but displayed several relevant characteristics such as elevated plasma-generated $n = 2$ and low frequency oscillations in line-averaged density. Examination of the internal profiles of the the single and two-temperature simulations revealed the toroidally-averaged λ and pressure profiles undergoing rearrangement during one of the density fluctuations coinciding with $n = 2$ activity, and some behavior (peaking of pressure, hollowing of λ) similar to that seen in HIT-SI simulations was observed. The preceeding analysis is not yet enough to make a definite conclusion on the origin of the plasma-generated $n = 2$, nor does it provide enough evidence to characterize the $n = 2$ energy as any particular instability, but factors such as elevated β and density fluctuation do suggest it. The study provides several interesting directions for investigation of this possible instability that will be discussed in more detail in Chapter 5, but the disparity in the presence of the $n = 2$ energy in low frequency simulations vs. high frequency simulations was notable, among other trends with increasing injector frequency that have been noticed in both HIT-SI and HIT-SI3. Identifying and characterizing these trends, including the proportion of plasma-generated $n = 2$, serves as the motivation for the work that will be presented in the next Chapter.

Chapter 4

FREQUENCY SCAN OF HIT-SI3 IN FINITE-β NIMROD SIMULATIONS

The injectors of HIT devices are run as inductive loads in an RLC circuit that has a resonant frequency tuned to the chosen driving frequency, for minimal reactive power losses in the injector circuits during operation. A disadvantage to this approach is that the driving frequencies are not set at the operator's discretion, but by the physical components available to create the RLC circuit for the injector (large tank capacitors and hand-wound inductors). In practice, this has limited the injector frequencies that have been used on HIT-SI3 to approximately 15kHz (between 14-16 depending on exact settings), 47.5 kHz, and 58.5 kHz. The preceeding HIT-SI experiment utilizing a top and bottom injector scheme was run using injector frequencies of 5 kH, 14.5 kHZ, 36.8 kHz, 53.5 kHz, and 68.5 kHz. This allowed trends to be derived from experiment using a large sampling of experimental data gathered at a range of injector frequencies. Similar studies could not be easily performed with the HIT-SI3 experiment given the limitations on the injector circuits; rather than using experimental results, the xMHD code NIMROD (covered in Chapter 2) was used to simulate formation and sustainment of HIT-SI3 spheromaks at six different injector frequencies. "Frequency scan" simulations such as this are an important tool for understanding the potential interaction between the spheromak and the injectors under different conditions and can be used to help understand the experimental results gathered from diagnostics.

4.1 Motivation

Past studies of HIT-SI (briefly covered in this section) showed signifcant differences in spheromaks formed with different injector frequencies, such as injector impedance and es-

timated current centroid position. This not only included the sampled experimental data, but also computational work in NIMROD to explore the differences in quantities that could not be directly measured by experiment as the injector frequency changed. After observing similar phenomena to HIT-SI in HIT-SI3 experimental data, an analagous NIMROD study for HIT-SI3 was initiated in the hopes that more trends for HIT devices could be deduced and that the computational data would provide potential explanations for some observed experimental behavior.

4.1.1 Experimentally observed differences

One primary motivation for investigating different injector frequencies in simulation is the observed differences between so-called "low frequency" discharges and "high frequency" discharges. High frequency HIT-SI3 discharges are empirically defined as those spheromaks formed with a SIHI injector frequency of over roughly 40-50 kHz. A more precise and physically based delineation is where the period of an injector is shorter than the toroidal Alfvén transit time, as well as the toroidal sound transit time. These periods are simply defined as the time it takes for a signal traveling at the Alfvén velocity ($\frac{B}{\sqrt{\mu_o \rho}}$)[2] or sound wave velocity to travel the path toroidally around the spheromak at the magnetic axis. These particular times represent important timescales, as the fastest physical times in which profile variation in magnetic field and pressure can occur. For the parameters of the low density spheromaks formed at 58.5 kHz analyzed in NIMROD later in this Chapter, the time scales work out as such:

$$v_{Alfvén} = \frac{B}{\sqrt{\mu_o \rho}} = \frac{0.02\ T}{6.34 \times 10^{-17}\sqrt{10^{19}}} \approx 98\ \frac{km}{s}$$
$$\tau_{Alfvén} = \frac{2\pi \times 0.3\ m}{v_{Alfvén}} \approx 19\ \mu s$$
$$c_s = \sqrt{\frac{P}{\rho}} = \sqrt{\frac{30\ torr}{3.2 \times 10^{-27} kg \times 10^{19} m^{-3}}} \approx 31\ \frac{km}{s}$$
$$\tau_{c_s} = \frac{2\pi \times 0.3m}{c_s} \approx 60.8\mu s$$
$$\tau_{c_s} > \tau_{Alfvén} > \frac{1}{58500Hz} \approx 17\mu s$$

For the selected magnetic field value of 20 mT, the transit time at the magnetic axis works out to 17 μsecs, approximately the injector period of the 58.5 kHz frequency. There is strong experimental evidence that spheromaks formed using injector frequencies above these toroidal transit times have substantially different properties from spheromaks formed at lower frequencies. These properties include but are not limited to: higher current gain ($\frac{I_{tor}}{I_{inj}}$), a more pronounced outward radial shift of the magnetic axis, higher injector impedance[31], and intermittent oscillation activity present in the toroidal current and FIR traces of some high frequency shots. These differences between several high performance low frequency (f_{inj} = 14.5 kHz -16.6 kHz) and high frequency (f_{inj} = 58.5 kHz) shots can be seen in Figure 4.1a and 4.1b, respectively. The high frequency experimental shots all display higher current gain and greater outward radial displacement than the low frequency shots as they evolve through time. This intruiging experimental evidence and the possibility of two separate regimes in injector frequency due to a physical reason provided more than enough impetus to perform a frequency scan, however similar results from HIT-SI also provided motivation and another data set for comparison as will be briefly covered in the next section.

4.1.2 Previous computational work

Experimental results prompted computational investigation by K. Morgan, who performed a series of simulations at frequencies between 5 and 100 kHz in zero and finite-β models in NIMROD.[42] An important result presented from this scan is the trend of increas-

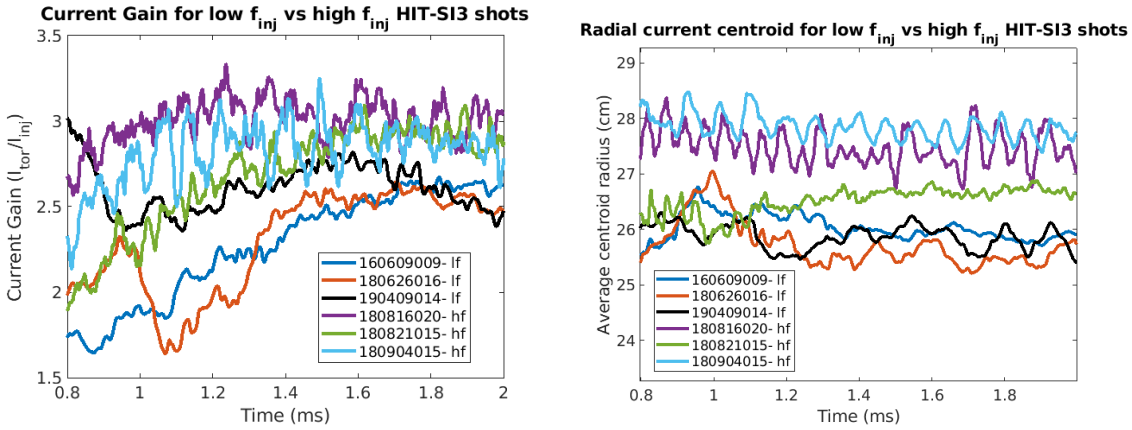

(a) Current gain ($\frac{I_{tor}}{I_{inj}}$) of several low and high frequency shots.

(b) Current centroid (magnetic axis) position of several low and high frequency shots.

Figure 4.1: Comparison between high performance low and high frequency shots using experimentally measured current gain (a) and radial centroid position (b).

ing β with injector frequency, as seen in Figure 4.2. Detailed study of the set of simulations revealed that not only current gain, but also various quantities such as individual heating terms (i.e, Ohmic vs viscous) and the impedance of the helicity injectors (defined $Z_{inj} = \frac{V_{inj}}{I_{inj}}$) all have a dependence on the injector frequency (more data from HIT-SI will be presented in following sections that shall corroborate these findings).

Additional simulations of HIT-SI were performed using the MHD simulation software PSI-Tet by T.E. Benedett and A.A. Kaptanoglu using both single and two-temperature MHD models, and some of these trends were reproduced using the fully 3D PSI-Tet software. Prior to this work, a detailed frequency scan study of HIT-SI3 from startup in NIMROD has not been performed. To fill the potential knowledge gap and provide useful numerical data for extrapolation of experimental data, a series of simulations of HI-SI3 was performed using injector frequencies f_{inj} of 5, 15, 30, 45, 60, and 75 kHz. To isolate the effects of different injector frequencies on the magnetic field structure without the influence of particle

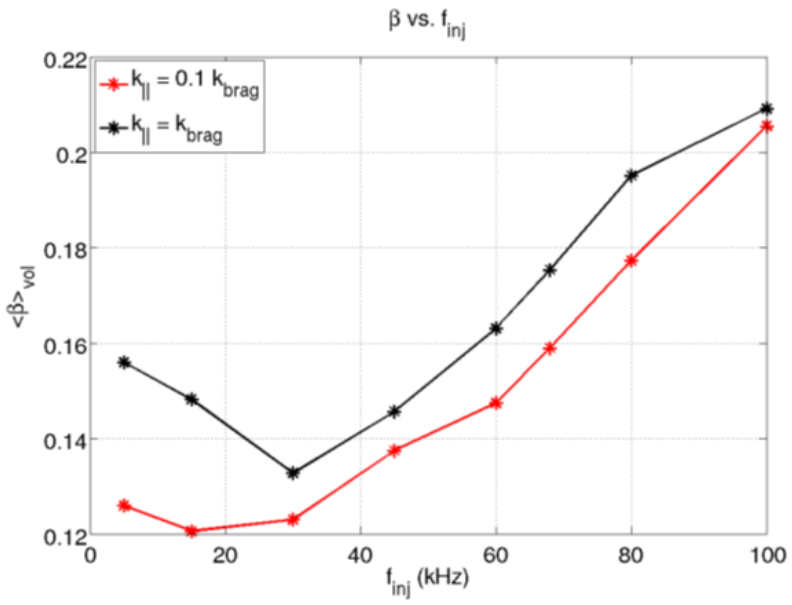

Figure 4.2: Average β as a function of injector frequency from NIMROD simulations of HIT-SI performed by K. Morgan, from [42].

(pressure and temperature effects), both zero-β and finite-β MHD models were used, and within finite-β both the single and two-temperature models were used to determine if any new effects would be caused by allowing the electron temeprature to evolve as a separate quantity.

This study is meant to compliment both the previous computational studies done on HIT-SI and HIT-SI3 as well as the experimental data from both devices. Due to the differences in the computational models (3D axisymmetric simulation on a 2D grid using Fourier modes in NIMROD vs. fully 3D tetrahedral grid), and the fact that the PSI-Tet simulations were performed using the HIT-SI operational frequencies and not the same frequencies as the NIMROD scans, only comparisons with the past NIMROD simulations will be made in this work; comparison of NIMROD to PSI-Tet is one area suggested for future work (see Chapter 5).

4.2 Simulation Parameters

Simulations of HIT-SI3 discharges were performed in the zero-β, single temeprature, and two-temperature models of NIMROD; as the purpose of this scan is to examine the differences in physical properties between spheromaks formed with different SIHI frequencies, the use different physics models can help suggest which properties (magnetic/current structure, temperature profile, pressure, etc) are most affected at different drive frequencies. Aside from frequency and temperature model, all parameters were kept as close in value across all simulations as possible. These parameters are listed in Table 4.1. The injector parameters were adjusted until the observed current and flux matched what is considered "high power" (shots of at least 5 MW, usually with $I_{inj} > 20$kA), since only the normal magnetic and tangential electric field strengths are directly set by the input, not the injector current or flux.

The timestep is listed as a range rather than a single value due to instability in high-frequency simulations that would develop as the result of too large a time advance could result in unphysically low densities which destabilize the Hall term used in the magnetic field advance. This is also the case for the hyperdiffusivity; it was increased it during the relaxation periods of some simulations to smooth-out very small discontinuities, during which small-scale instabilities would develop that ended up crashing the simulations via time-step minimization.

4.3 Zero-β, Single, and Two-temperature Model Comparison

4.3.1 Toroidal current gain and centroid

The first results that are compared are those that vary across all three sets of simulations, namely magnetic/electric current activity (as the zero-β model does not evolve density or temperature). Important parameters used in analyzing experimental HIT-SI3 discharges are the total toroidal current as measured by the Rogowski loop formed by the poloidal surfae probe arrays, and the current gain (again defined by $I_{gain} = I_{tor}/I_{inj,quad}$). These quantites

Table 4.1: The parameters used for the frequency scan simulations of HIT-SI3, including derived injector quantities.

parameter	value
timestep Δt (ns)	2.5 - 5
injector current (kA)	20
injector flux (mWb)	1.05
injector λ (m^{-1})	21
wall density (m^{-3})	3 x 10^{19}
wall temperature (eV)	3
viscosity ν (ms^{-2})	300
diffusivity (ms^{-2})	200
$\delta_{0,i}$, $\delta_{1,i}$	0.667, 2.70
$\delta_{0,e}$, $\delta_{1,e}$	3.77, 14.79
$\gamma_{0,i}$, $\gamma_{1,i}$	2.64, 2.00
$\gamma_{0,e}$, $\gamma_{1,e}$	11.92, 4.66
k_{par} coefficienct	1
k_{perp} coefficient	1
Hyperdiffusivity ($m^2 s^{-4}$)	1e-4 -1e-2

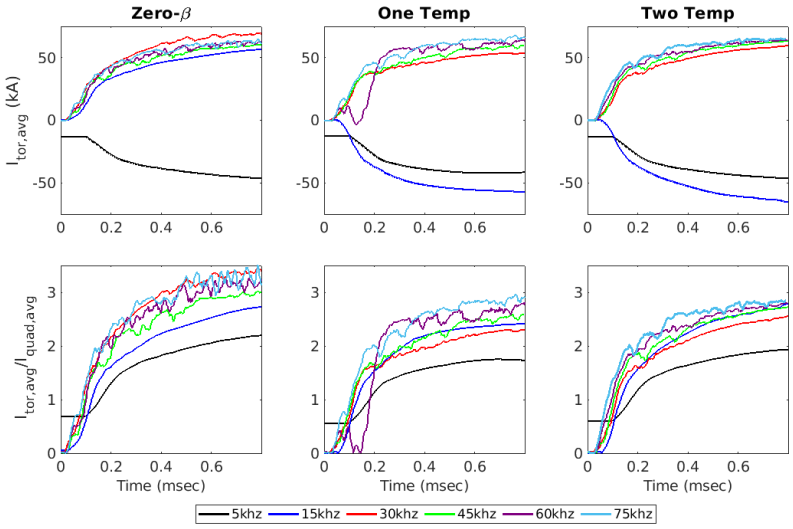

Figure 4.3: The toroidal current (top) and current gain I_{tor}/I_{inj} (bottom), smoothed over time using a moving average over the injector period for zero β (left), single (middle), and two-temperature NIMROD simulations from the HIT-SI3 frequency scan.

are displayed in Figure 4.3. In addition to the total magntitude of the toroidal current, the "sign" representing the direction of the toroidal current with respect to the injectors (aligned in the A-B-C order the injectors are fired in or anti-aligned) is also reflected in the plots of toroidal current; there is some thinking (which will be discussed further) that the sign of toroidal current may reflect additional underlying differences between discharges. It is important to note that across all three temperature models, frequencies of 30 kHz or higher were all "positive" toroidal current shots, and that 5 kHz was in the "negative" direction. The 15 kHz driving frequency was the only one that saw a difference in toroidal current sign between the zero-β and finite-β models. In general it appears the current gain I_{gain} increases with driving frequency for nearly-identical injector conditions, a result seen in HIT-SI3; again though a difference appears between the zero-β and finite-β models, with the 30 kHz simulation having higher gain than even the 75 kHz simulation in zero-β whereas 30 kHz actually achieved the second-lowest gain in the single and two temperature simulations.

Comp. Model	Alven transit time	Injector period
zero-β	19.7 μs	33.3 μs
one-temp	24.7 μs	33.3 μs
two-temp	23.2 μs	33.3 μs

Table 4.2: The toroidal Alfvén transit time in the zero-β, single, and two-temperature NIMROD simulations of HIT-SI3 at 3 kHz.

The interesting behavior at 30 kHz is reflected in the toroidal current centroid position, a measurement of the approximate "center" of the spheromak's toroidal current via weighed surface probe measurements of the poloidal magnetic field as short in Equation 3.5.

The calculated radial and vertical centroid positions from all the simulations are shown in Figure 4.4, with the standard deviations of the positions in Figure 4.5. When the calculated radial and vertical positions of the current centroid for each simulation are compared, the 30 kHz driven spheromak has the highest vertical and most inward radial center position of all the zero-β simulations. In the finite-β models, the 30 kHz simulation is comparable in position to the other higher frequency simulations and the 15 kHz simulation. In all simulations, the 5 kHz-driven spheromak exhibits the greatest radial shift.

The interesting behavior of the 30 kHz simulation suggests a possible "transition frequency" as the injector period begins to become shorter than the toroidal Alfvén transit time, $\tau_A = \frac{2\pi R}{v_A}$. The toroidal Alfvén transit time, calculated using the average toroidal field measurement during sustainment, for each of the 30 kHz simulations is displayed in Table 4.2 compared to the injector period, in microseconds.

It's interesting to note that the zero-β simulation's Alfvén transit time is furthest from the injector period and yet exhibits the most activity in the toroidal current, compared to the finite-β simulations. The link between a "transition" injector frequency and toroidal Alfvén transit time, the possible stabilizing effect of finite-β, and toroidal current activity

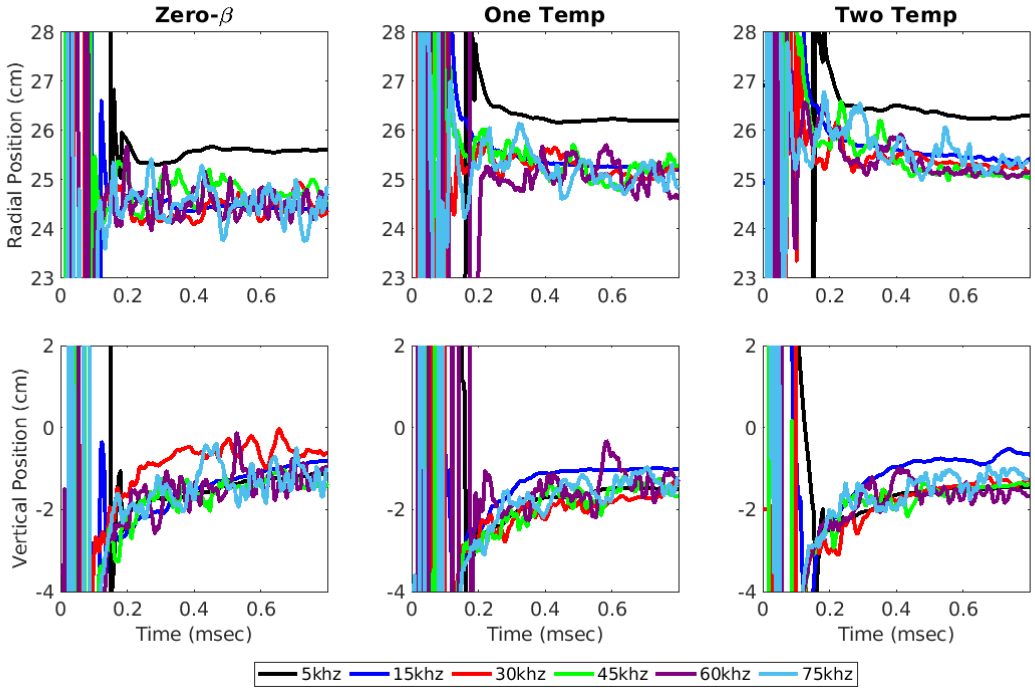

Figure 4.4: The current centroid radial (top) and vertical (bottom) positions for the zero-β, single-temperature, and two-temperature NIMROD simulations in the HIT-SI3 frequency scan.

will be invesitgated in more depth in future works.

4.3.2 Synthetic Surface Probe Mode Analysis

Synthetic magnetic signal data is sampled from NIMROD at the two sets of sixteen gridpoints corresponding to the positions of the Mirnov probes on the midplane of the HIT-SI3 experiment that are are used to resolve the toroidal Fourier spectrum from magnetic field data of up to 8 modes ($n = 0$ to $n = 7$). Figure 4.6 displays the location of the sampling on the NIMROD finite-element grid. The proportion of the first three nonaxisymmetric ($n = 1, 2, 3$) magnetic field modes of the zero-β, single temperature, and two temperature models are presented in Figure 4.7; this is a ratio taken with respect to the $n = 0$ magnetic

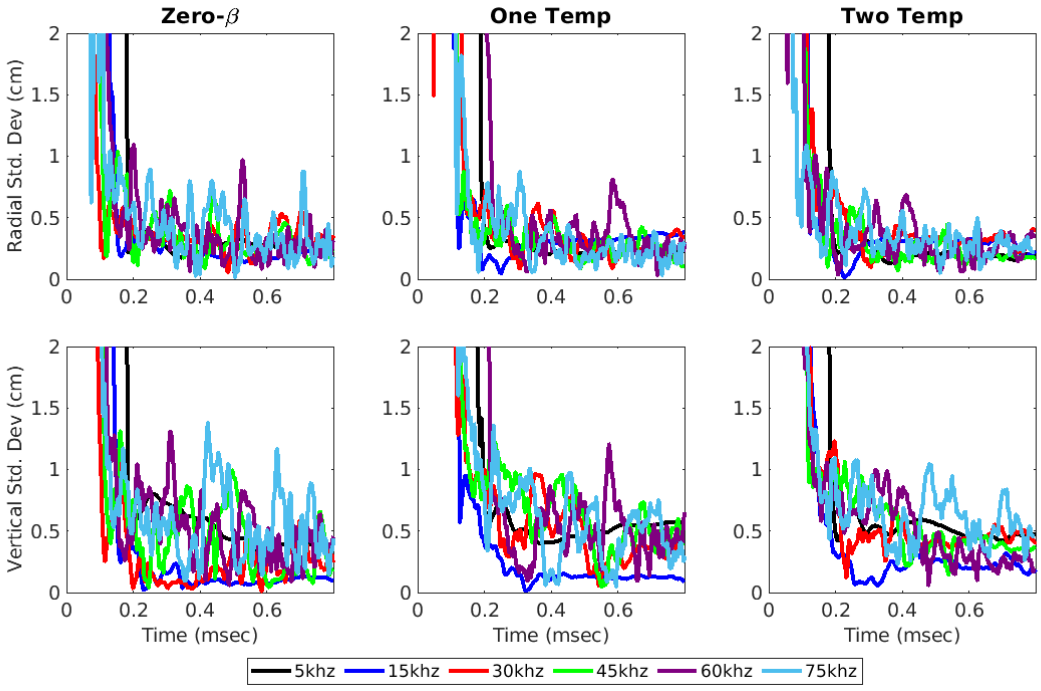

Figure 4.5: Standard deviation of current centroid radial (top) and vertical (bottom) positions for the zero-β, single, and two-temperature NIMROD simulations in the HIT-SI3 frequency scan.

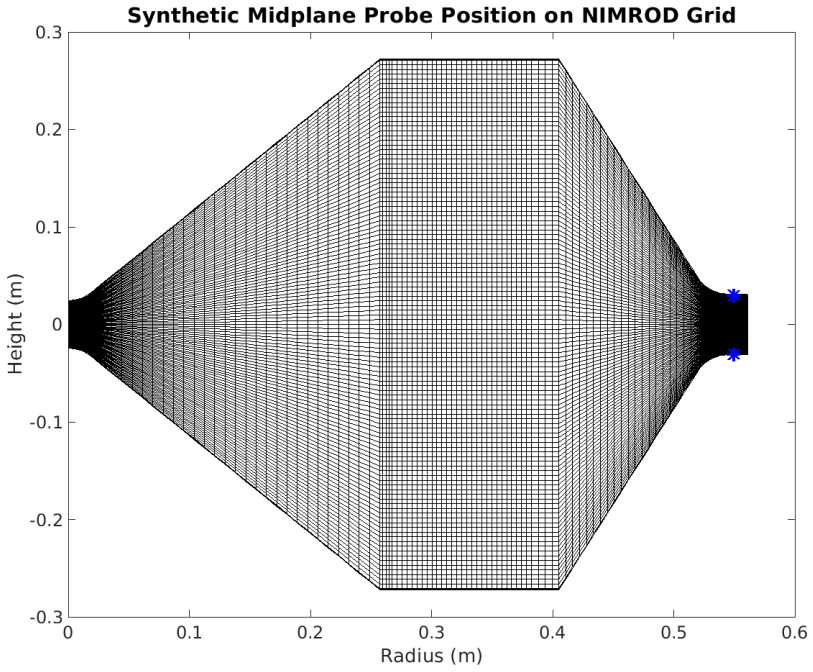

Figure 4.6: The finite-element grid used in NIMROD simulations of HIT-SI3 with the positions of the midplane Mirnov probes marked with blue stars.

fields as measured on the edge, and so isn't representative of the internal magnetic modes of the spheromak, but provides insight to the interaction between the edge of the spheromak equilibrium and the injector fields. The lower frequency simulations, 5 and 15 kHz, have higher proportions of $n = 1$ than higher frequencies, and vice versa for the $n = 3$ fields. All simulations show a relatively large proportion of $n = 2$ field, which is expected as $n = 2$ is the predominate imposed mode from the phasing of the injectors that was chosen (0-120-240).

The increased energy associated with certain Fourier modes can indicate the presence of major instabilities ($n = 1$ kink, $n = 2$ pressure-driven mode), however the helicity injectors impose a diverse spectrum of Fourier modes on the spheromak plasma. To gain more insight into the plasma-generated effects from the different injector fields imposed at each frequency, Biorthogonal Decomposition-derived empirical modes associated with the injectors and the

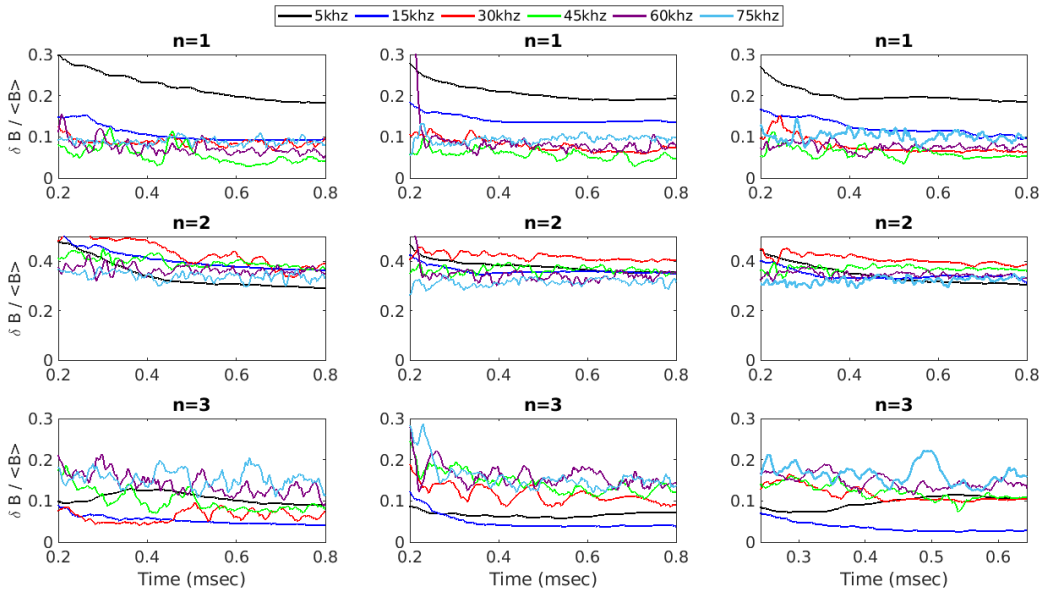

Figure 4.7: The modes for $n = 1$ (top), $n = 2$ (middle), and $n = 3$ (bottom) modes for the zero-β (left), single-temperature (middle), and two-temperature (right) simulations from the HIT-SI3 frequency scan generated from synthetic midplabe Mirnov probe signals.

spheromak equilibrium can be isolated and subtracted off. This BD substraction has been covered and demonstrated extensively in previous chapters and will not be strictly reviewed, but has been applied to the sythetic surface probe data from the zero-β, single-temperature, and two-temperature NIMROD frequency scan simulations. The nonaxisymmetric $n = 1$, $n = 2$, and $n = 3$ fields, after the subtraction of the injector and spheromak fields, is presented in Figure4.8. The reduction in the $n = 1$ field proportion is immediately obvious and corroborates the findings of the BD study done both on HIT-SI data confirming stability to $n = 1$ and follow-up study done on HIT-SI3 low frequency data.[10]

There are more interesting dynamics in the plasma-generated n=2 activity on the edge in higher frequency simulations (especially 60 and 75 kHz). Fluctuations with magnitudes of $10 - 20\%$ of the equilibrium edge field are generated by plasma activity not part of the injectors or spheromak, which could indicate an $n = 2$ instability of some sort growing and then decaying. The largest fluctuations appear to occur at semi-regular intervals, as was seen in the experimental HIT-SI3 high frequency shots examined in the previous Chapter, with periods of 100-200 microseconds. Notably, the $n = 2$ activity in the two-temperature simulations settle at the simulations progress, with the exception of the 75 kHz simulations. The included presence of electron temperature dynamics separate from the ion temperature clearly has some influence on the generation of this activity, however what exactly that influence is will not be clear until the mechanism behind the $n = 2$ activity is identified.

Some n=3 activity is present after subtracting injector and equilibrium fields; as the injectors do not directly impose an $n = 3$ field, the mode originates primarily from ther spheromak equilibrium and interactions between the injectors and equilibrium that might produce non-linear mode growth. The $n = 3$-like shape of the injector mouths within the spheromak might account for this mode's presence in real life, but the axisymmetric domain of the NIMROD simulations exlcudes this. Unlike the $n = 2$ energy, there does not appear to be any major variation in the magnitude of plasma-generated $n = 3$ with frequency.

Revisitng the plasma-generated $n = 2$, it's interesting to note across all three models that the 5 and 15 kHz simulations have substantially lower magnitude that all the simulations

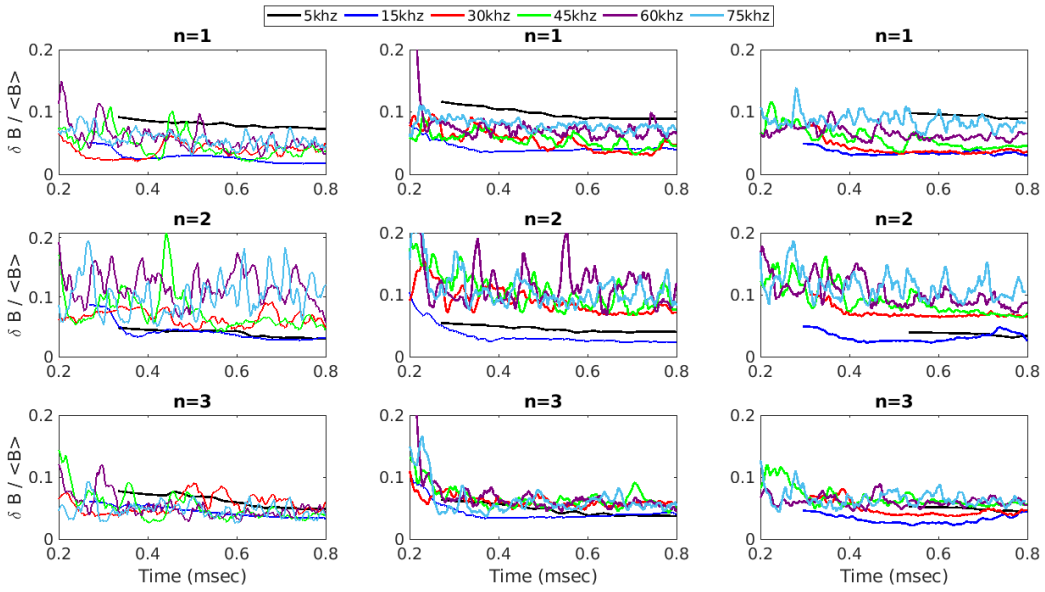

Figure 4.8: The plasma-generated $n = 1$ (top), $n = 2$ (middle), and $n = 3$ (bottom) modes for the zero-β (left), single-temperature (middle), and two-temperature (right) simulations from the HIT-SI3 frequency scan.

at 30 kHz and above. As noted with the toroidal currents and the centroid position motion, this may suggest some transition activity. The substantial differences between zero-β, single-temperature, and two-temperature simulations suggest that not only does including temperature and density evolution appear to influence the dynamics, the inclusion of electron temperature advance definitely affects the magnetic field dynamics and may have some stabilizing effect. The next section will focus on examining the differences between the single and two-temperature simulations.

4.4 Trends Identified with Frequency in Finite-β

Temperature and density are evolved when "finite"-β MHD models are employed. Both computational and experimental data from HIT-SI has indicated that the ratio between particle pressure and magnetic pressure, β, increases with increasing injector frequency.[13] This set of simulations using the HIT-SI3 injector configuration in NIMROD provides an opportunity to further investigate the trend, at least computationally.

4.4.1 β and temperature

Figure 4.9 displays the volumetric averaged ion and electron temperature, thermal energy, and volume-averaged β for the single and two-temperature HIT-SI3 NIMROD simulations (in the case of the single-temperature simulation, the electron temperature used is the MHD single-temperature once again). While in both sets ion temperature appears to increase steadily as a function of frequency, the ion temperatures in the two-temperature simulation are nearly twice as high as in the single-temperature. As one of the primary differences between the models is the use of inter-species heat exchange, one explanation is the energy transfer from the electrons to the ions is providing additional heating. Indeed, even the electron species temperature is slightly higher than the standard MHD temperature from the single-temperature model. This may indicate the increased importance of modelling electron dynamics to properly capture the Ohmic heating in simulations of HIT-SI3. The single-temperature simulations show the β obtained from each injector frequency converging

to a relatively steady value within one percent of one another except for the noticeably lower 5 kHz simulation. In contrast, the calculated β from the two-temperature simulations increase with increasing injector frequency, with the 75 kHz simulation having the highest β value over time, and 15 kHz having the lowest β, slightly breaking the frequency trend. In spite of this discrepancy with the lowest frequencies, the trend of increasing β with increasing frequency from HIT-SI has been verified for the two-temperature HIT-SI3. The fact that this trend becomes apparent in the two-temperature simulation and not the single-temperature may highlight the importance of accurately modeling energy deposition and transfer between the Ohmically-heated electrons and the viscously-heated ions, and overall the importance of using a two-temperature MHD model to simulate SIHI devices as opposed to the standard single-temperature fomulation.

4.4.2 Heating power terms

Rapidly changing fields due to reconnection between the injectors and the speromak plasma causes a substantial amount of viscous heating ($P_{visc} = \int \nu(\nabla u)^T \Pi dV$) as ions are accelerated. In previous NIMROD simulations of HIT-SI, it was discovered that viscous heating of the ions increased substantially as injector frequency increased, and contributed and overall greater fraction of the power compared to Ohmic heating ($P_{Ohm} = \int_V \eta j^2$). The calculated power from the single and two-temperature NIMROD simulations of HIT-SI3 verify this trend in the three injector machine as well. The viscous ion heating power and ohmic heating power are plotted over time for in 4.10 for each frequency and show that for both models the viscous heating power increases with increasing injector frequency; conversely, the Ohmic heating increases much more weakly with increasing frequency. The ratio of the powers is plotted for both models in 4.10, showing a steady increase in the ratio of viscous heating power to ohmic in the two-temperature model, however this ratio flat-tops in the single temperature model. This, along with the previous temperature results, once again highlight the importance of capturing electron behavior that may not be present in the standard MHD model and the possible utility of the two-temperature model.

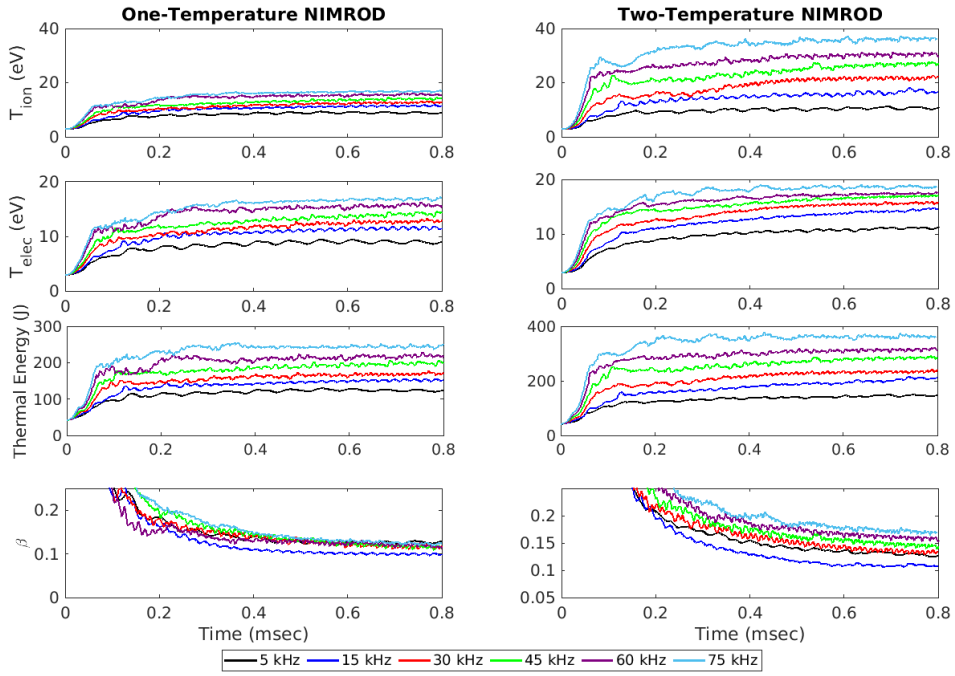

Figure 4.9: Evolution of the temperature for both ions and electrons, total thermal energy, and volume-averaged β, calculated using $\frac{2\mu_o<P>}{<B^2>}$ for single and two-temperature NIMROD frequency scan simulations of HIT-SI3.

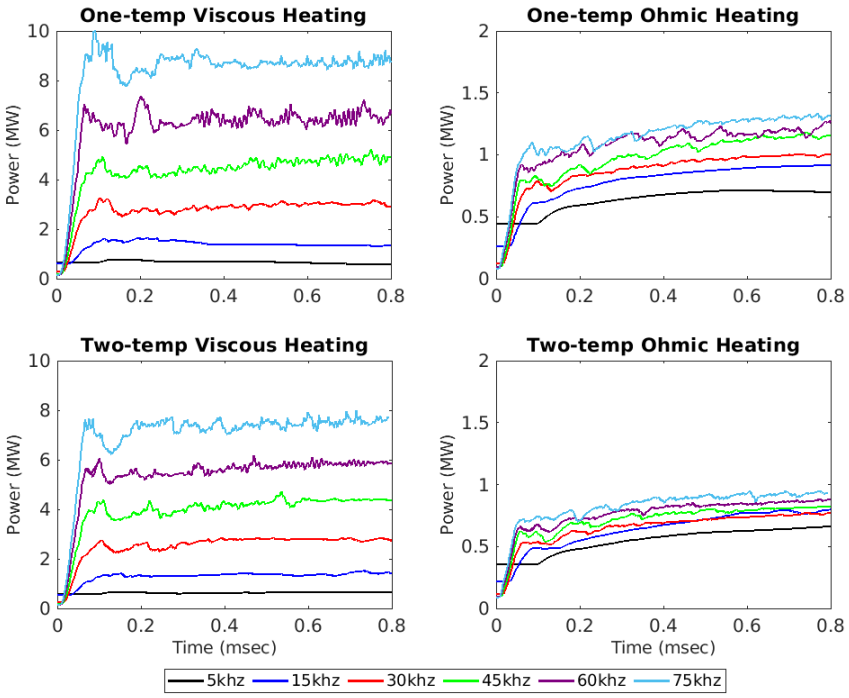

Figure 4.10: The viscous heating (left plots) and Ohmic heating (right plots) from single (top plots) and two-temperature (bottom plots) NIMROD as a function of time.

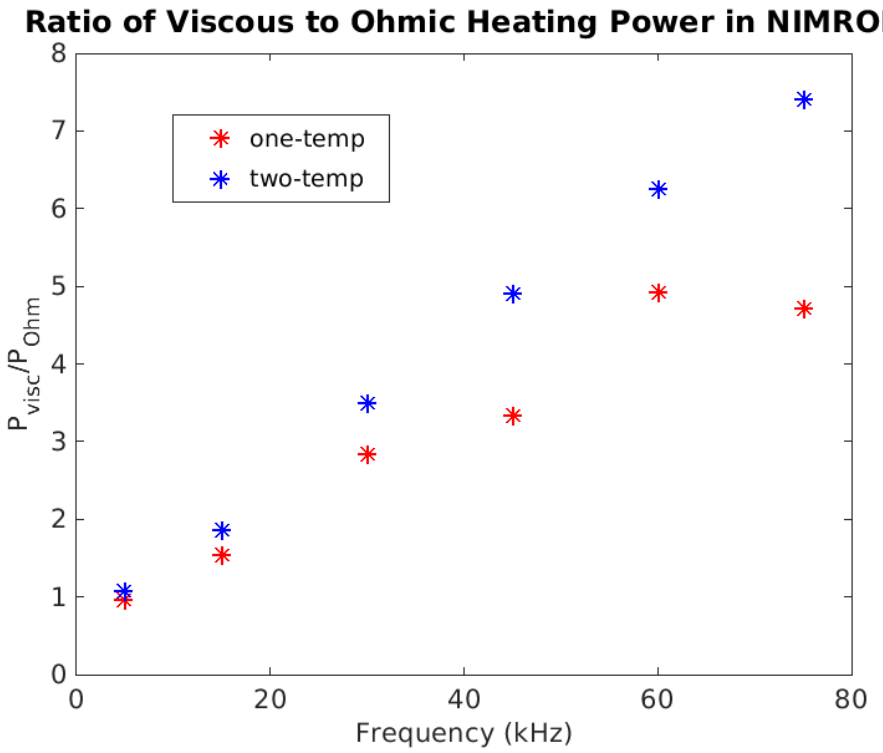

Figure 4.11: Ratio of the Viscous heating power term to the Ohmic heating power term, plotted as a function of frequency for single and two-temperature NIMROD.

4.4.3 Injector impedance

The use of power balance using the injector voltage and current [31][32], as well as fitting to experimental data, has yielded a rough empirical formula for the impedance ($\frac{V_{inj}}{I_{inj}}$) of the injectors that has a dependence on frequency:

$$Z_{inj} = C_1 \frac{\mu_o R_o}{\pi} \left(\frac{\lambda_{inj} I}{8 \lambda_{spher} a^3 ne} + \frac{2 C_2 \omega_{inj}}{a \lambda_{spher}} \right) \tag{4.1}$$

where R, a are the major and minor radii, respectively, λ_{spher} is the spheromak λ,λ_{inj} is the injector λ, I is the spheromak current, n is the density, e is the electron charge, and most relevant ω_{inj} is the angular injector frequency, $2\pi f_{inj}$.The formula includes a term that is dependent on the injector frequency, so it's expected that a linear dependence on injector frequency would appear as impedance is plotted against frequency. Figure 4.12 is such a plot, taking the average injector impedance from each of the zero-β, single-temperature, and two-temperature simulations. A linear interpolation of the data is also plotted alongside the individual points as a comparison for how well the injector frequency fits a linear trend.

The injector impedance from NIMROD was calculated indirectly, due to the lack of full injectors in the axisymmetric domain that would allow loop integral calculations for the voltage. The injected power is first found by integrating the total power in the domain (the time-derivative of the thermal, magnetic and kinetic energy terms) and subtracting the heat fluxes to the wall and the energy lost to resistive decay:

$$P_{inj} = \sum_s \int_V \frac{d}{dt} \left(\frac{B^2}{2\mu_o} + \frac{k n T_s}{\gamma - 1} + \frac{1}{2} \rho u_s^2 \right) - \oint_s q_{wall,s} - \int_V \eta j^2 \tag{4.2}$$

with the electron and ion species s being summed together in two-temperature simulations. The injected power P_{inj} is then divided by the known injector current according to the formula $P = VI$ to find the injector voltage. The injector voltage can then be divided again by the current to find the real impedance (or just taking the power and dividing by I^2). Figure 4.12 shows a strong linear dependence of the injector impedance on the injector frequency, with the average impedance values closely aligning with the linear fit. The

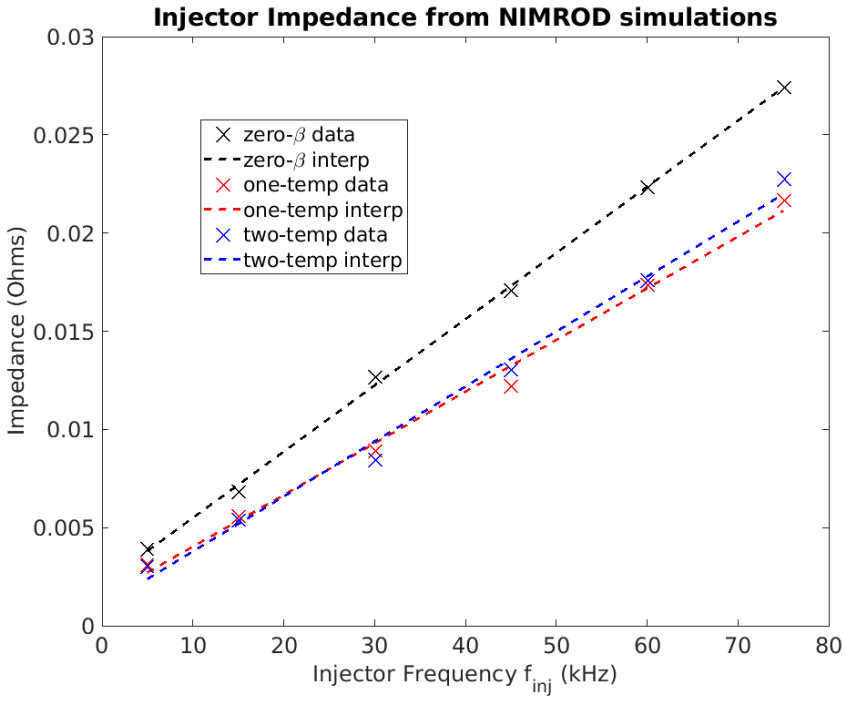

Figure 4.12: The average injector impedance plotted as a function of frequency for zero-β, single-temperature, and two-temperature NIMROD simulations of HIT-SI3, with interpolated linear functions (dashed lines).

zero-β impedance is slightly higher, and upon inspection this is due to the zero-β simulation having higher voltage, likely a consequence of static density and temperature and thus lower loss terms. Direct fitting to the IDCD-derived impedance equation is not presented in this section; instead a modified version that allows comparison to other simulation data sets will be presented in the following section.

4.5 Comparisons to HIT-SI Trends

The ultimate end goal of the HIT-SI3 experiment, and the HIT device program, is to produce a functional fusion reactor based around a SIHI-driven spheromak. Different iterations of experiments are required to derisk single aspects and new approaches at a time, so discovering trends and common behaviors between generations of HIT devices is imperative to understanding the possible behavior of a fusion reactor-scale HIT device. Just like the HIT-SI3 scan performed in this study, a scan of HIT-SI was performed by K. Morgan using finite-β NIMROD, the main difference being the HIT-SI simulations were "sustainment" simulations starting with a developed spheromak equilibrium; the HIT-SI3 simulations were all performed from startup. Nonetheless, the HIT-SI simulations provide an additional data set for determining trends related to frequency, and the next section will compare the most pertinent data sets from the HIT-SI frequency scan simulations to those from HIT-SI3 frequency scan.

4.5.1 Current gain and kinetic energy

Some of the most straightforward trends that can be compared are the trend of increasing gain with injector frequency and increasing total kinetic energy with frequency. The former trend is readily observed in experiment and should be reflected in the simulation data, whereas the latter would be a straightforward consequence of increased viscous heating activity. Figure 4.13 displays the current gain $I_{gain} = \frac{I_{tor}}{I_{inj}}$ sampled from the end the HIT-SI3 finite-β simulations using single and two-temperature NIMROD to the HIT-SI simulations performed using $k_{par} = k_{perp}$, which matches the settings in the HIT-SI3 frequency

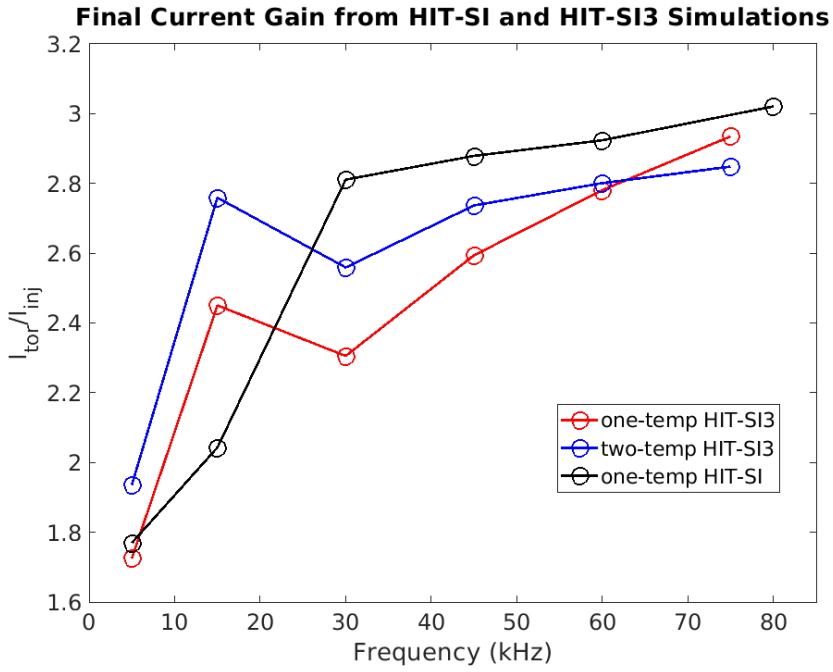

Figure 4.13: Current gain values from the end of finite-β simulations of HIT-SI and HIT-SI3 plotted as a function of frequency.

scan. All three sets of simulations yielded the lowest gain at $f_{inj} = 5$ kHz, and see a steady increase in gain as injector frequency increases from 45 kHz. Interesting behavior is once agin noted at 30 kHz - the dip in current gain at 30 kHz before once again rising with frequency is more apparent and curiously is not reflected in the HIT-SI simulation data, which instead suddenly jumps in β value at 30 kHz. Overall, HIT-SI has higher simulated current gain than HIT-SI3, however too many other parameters vary between the simulations for this observation to be a meaningful result.

Figure 4.14 displays the average kinetic energy from the simulations done in finite-β to the HIT-SI simulations. Surprisingly, while both HIT-SI and HIT-SI3 show the average total kinetic energy rising with frequency, the average kinetic energy in HIT-SI3 is much higher. This could partially be due to the formation process being included in the HIT-SI3 simulations, however relaxation still occurs in the spheromaks sustained from equilibrium

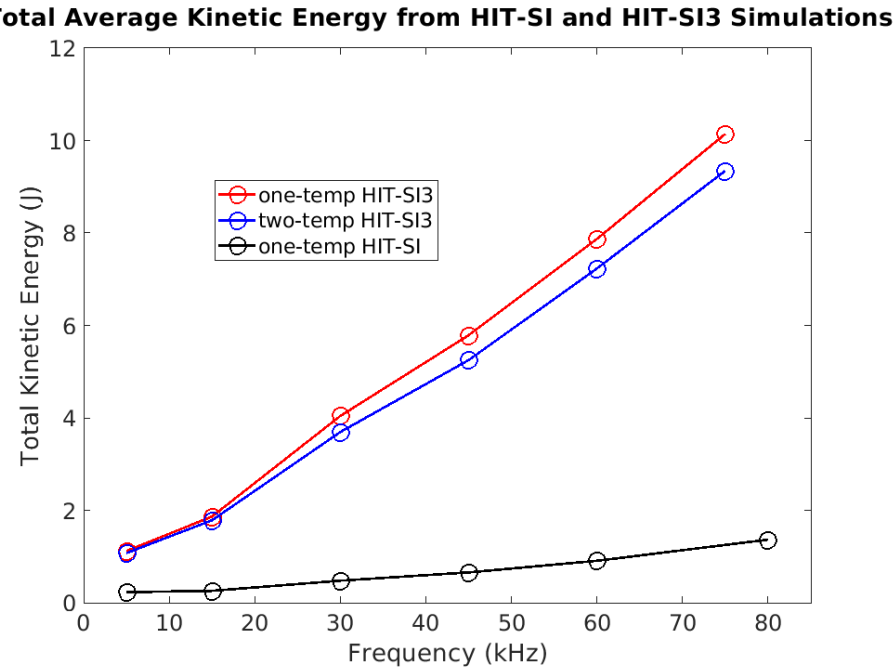

Figure 4.14: Average kinetic energy as a function of frequency for single-temperature NIMROD simulations of HIT-SI and single and two-temperature simulations of HIT-SI3.

and would contribute to the kinetic energy. Another possibility is the lack of balanced forces in HIT-SI3; HIT-SI had injectors directly opposed to one another, but the asymmetric injector configuration in HIT-SI3 could lead to more net kinetic energy being imparted onto the plasma fluid by the injectors in each period.

4.5.2 Increasing β with frequency

The trend of β increasing with frequency was postulated from experimental measurements of HIT-SI and was observed in NIMROD simulations of HIT-SI, as seen in Figure 4.2.[13] Verifying this in HIT-SI3 is of great interest, especially as since previously covered exceeding β limits may trigger instabilities. Figure 4.15 displays the total volume-averaged β (electron plus ion, or ion plus ion in the case of single-temperature simulations) at the end of each simulation after the spheromak has reached steady state. HIT-SI has a higher sampled β

than either HIT-SI3 data set, with the HIT-SI3 two-temperature closer to HIT-SI in value and slope in the linearly increasing portion of beta vs frequency. Rather than the dip at 30 kHz that HIT-SI exhibits, consistent with previously postulated activity associated with that injector frequency, the volume-averaged β dips at 15 kHz and rises linearly from there in HIT-SI3, and this is mostly in the two-temperature simulations. In fact, the β from single-temperature NIMROD simulations of HIT-SI3 hardly increases with frequency, dipping once again at the 60 kHz simulation. Though this simulation experienced a later relaxation, the β was sampled from the end of the simulation after the spheromak reaches steady state, making this not an issue that could affect the trend. It would also not explain the 5 kHz β value being higher than the 75 kHz simulation, a complete reversal of the trend predicted from HIT-SI single-temeprature and HIT-SI3 two-temperature. This suggests the single-temperature simulations may have some deficiency in modeling the heating and confinement in HIT-SI3 compared to two-temperatures, rather than casting doubt on the trend of β generally increasing with frequency; as mentioned previously, this is a trend not only confirmed by multiple sets of simulations but also from experimental measurements of low frequency vs high frequency spheromaks in HIT-SI.

4.5.3 Injector impedance

Comparing the injector impedance between HIT-SI and HIT-SI3 is a relatively straightforward task, as it simpling involved getting the real part of the impedance Z by dividing the real injector voltage by the quadrature injector current (the derivation of the injector) voltage was covered in the previous initial section on impedance). Because of the previously presented data sets, only the single-temperature simulation from HIT-SI3 will be compared to HIT-SI due to the similarity in physical model - the deviation from the zero-β and two-temperature values is not as significant as in other quantities. The time-averaged injector impedance from HIT-SI and HIT-SI3 simulated in single-temperature NIMROD is plotted by frequency in Figure 4.16. Compared to HIT-SI3, the linear trend in HIT-SI is not as strong in lower frequencies, and the values are higher overall, but again as the simulations

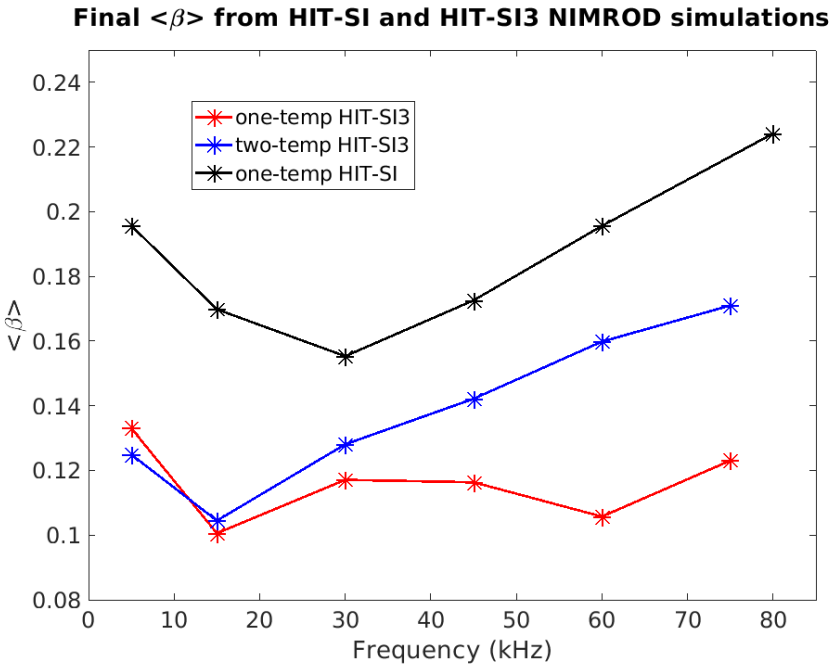

Figure 4.15: The final value for volume-averaged $\beta = \frac{2\mu_o < P >}{< B^2 >}$ in single-temperature HIT-SI, and single and two-temperature HIT-SI3, plotted as a function of frequency.

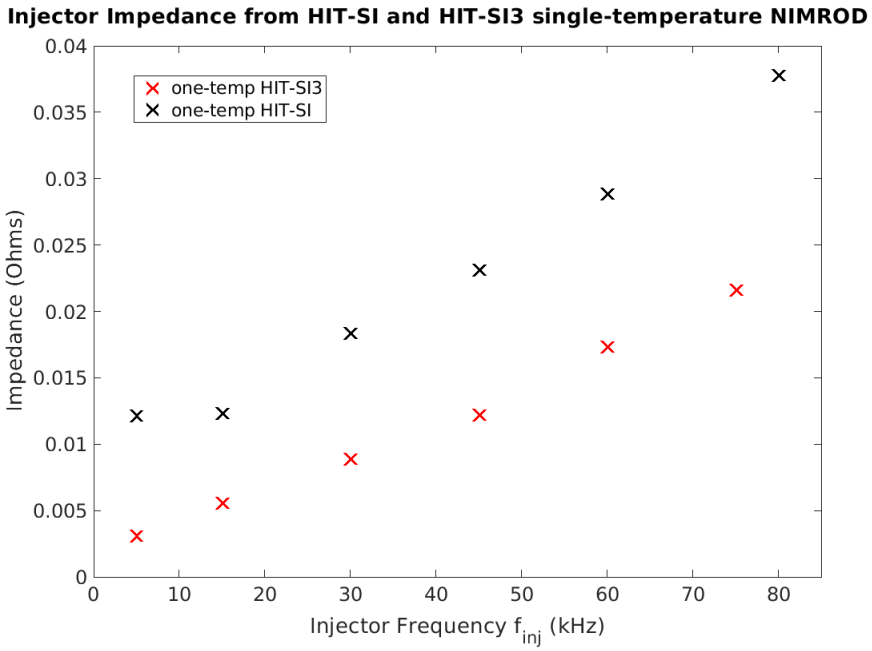

Figure 4.16: The time-averaged injector inpedance value from HIT-SI and HIT-SI3 single-temperature NIMROD simulations plotted as a function of frequency, showing a linear trend.

were not performed using identical values (nor were they intended to be), the second result could be a result of parameter variation.

Though extensive comparison to PSI-Tet simulations will not be discussed, an addition straightforward method of comparison to HIT-SI is to compare the value of fitting constants derived from simulation data using the impedance equation mentioned in the previous section. A frequency scan of HIT-SI was performed in two-temperature PSI-Tet by A. Kaptanoglu across the experimental frequencies of 14.5, 36.5, 53.5, and 68.5 kHz. In the resulting publication from that study, a simplication to the linear IDCD-derived impedance formula was used to fit experimental data.[9] Starting from the original formula

$$Z_{inj} = C_1 \mu_o R_o \left(\frac{1}{8\pi e a^3} \frac{\lambda_{inj}}{\lambda_{sph}} \frac{I_\phi}{n}\right) + 2\pi C_2 f_{inj} \tag{4.3}$$

the frequency-based term was assumed to have a greater dominance in PSI-Tet, and when the front constant $C_1\mu_o R_o$ is multiplied against each term and the multiplied constants are collapsed into one constant $C = C_1C_2$, the formula is simplied to

$$Z_{inj} = 2\pi\mu_o C R_o f_{inj} \tag{4.4}$$

Figure 4.17a is from the referenced work by A. Kaptanoglu that plots the constant C derived using the formula in Equation 4.4, showing a relatively large constant with a reported average across frequencies of $C = 1.9$. This is an order of magnitude higher than the constant reported using impedances from NIMROD simulations, $C = 0.18$ (again reference Alan's paper). Figure 4.16 b displays the constants as calculated from each of the three models of NIMROD used in HIT-SI3. The average constant for the zero-β model was $C = 0.11$, whereas both finite-β models yielded a constant of $C = 0.09$. Just like the HIT-SI simulations also performed in NIMROD, this constant is substantially lower than what is found using PSI-Tet, however the constant is also smaller than in HIT-SI by a factor of 2 in finite-β.

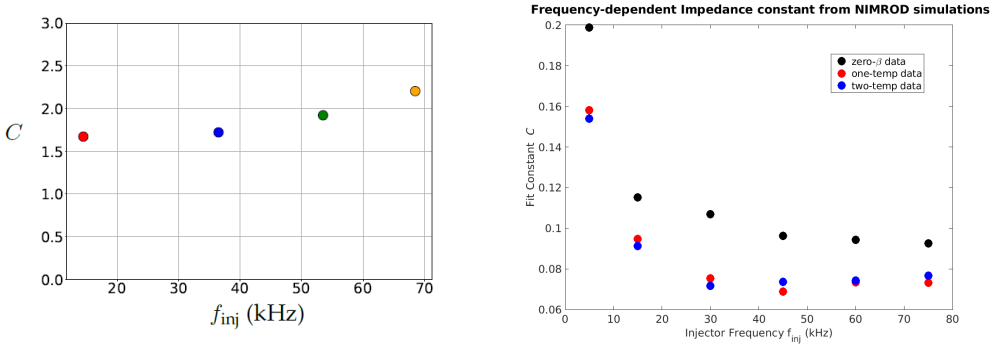

(a) (b)

Figure 4.17: (a) A constant derived from fitting the injector impedance to the simplified formula in Equation 4.4, for HIT-SI simulations performed in the MHD software PSI-Tet (taken from [9]) (b) The same constant derived from all three HIT-SI3 simulation sets.

4.5.4 Formation dynamics at high-frequency

A final noteworthy area of comparison is between the early formation of HIT-SI simulations vs HIT-SI3. While simulations in the HIT-SI frequency scan were carried out as "sustainment" simulations from a high-gain initial equilibrium, simulations from startup were performed using experimental frequencies including the 68.5 kHz frequency that was the highest frequency used in HIT-SI. This allowed a detailed look into the formation dynamics of the spheromak at high frequency, which displayed radically different behavior from the $n = 1$ dominated relaxation that is associated with spheromaks formed with a Marshall gun and in spheromaks formed using low injector frequencies in HIT-SI. Simulations of HIT-SI from startup at high-frequency experience a period before relaxation (when the spheromak $n = 0$ energy overtakes the non-axisymmetric components) during which the $n = 2$ energy is dominant, as can be seen in Figure 4.18 which was taken from [42]. The magnetic energy from a low-frequency HIT-SI simulation started from formation is also shown, displaying the typical buildup of $n = 1$ energy seen in other spheromak experiments before relaxation.

Visualizations of the vertical magnetic field B_Z of the finite-β high-frequency HIT-SI simuation during formation were made using the software Visit and are displayed in Figure 4.19, also take from [42]. These visualizations show B_Z initially taking on a shape resembling the injectors before merging into a single coherent field in the spheromak. The B_Z field, which is both from the field component imposed by injectors and a component of the poloidal magnetic field, shows a state of injector-dominance before the spheromak relaxes and is then donimanted by the poloidal fields.

Based on the geometry of the HIT-SI3 injectors, one would expect a similar period in high injector frequency HIT-SI3 spheromak formation in which the $n = 3$ energy is dominant. When the volumetric energies across all three models and all frequencies are examined however, there is no such period of $n = 3$ dominance. The magnetic energy for the first five Fourier modes for the two-temperature 60 kHz NIMROD during the relaxation of the spheromak is plotted in Figure 4.20. Instead, the $n = 1$ and $n = 2$ energy run about equal

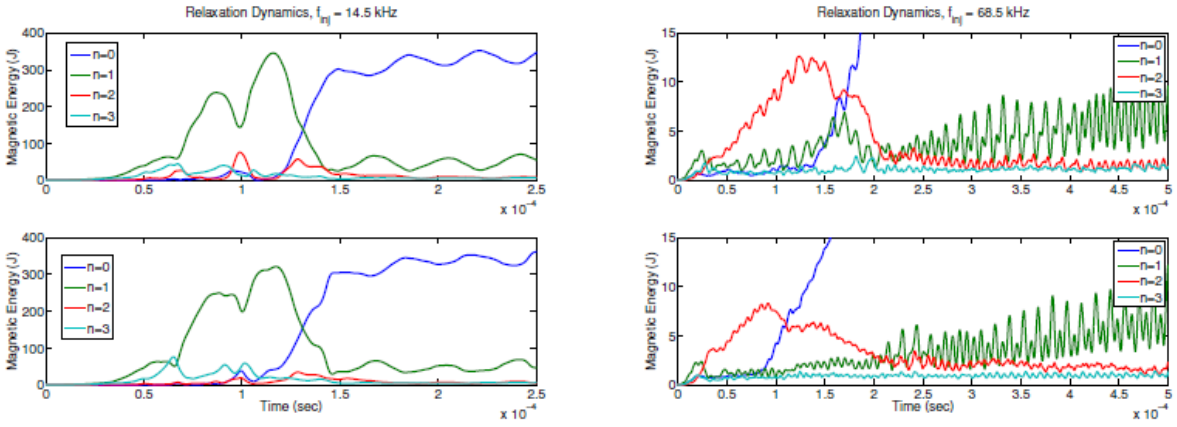

Figure 4.18: Plots of the volume-integrated energy of different Fourier modes in the magnetic fields from a NIMROD simulation of 15 kHz HIT-SI (left) and 60 kHz HIT-SI (right). Before spheromak relaxation and the the $n = 0$ energy becomes dominant, the $n = 1$ is dominant in the low frequency and $n = 2$ is dominant in high frequency. Taken from [42]

in magnitude before relaxation when the $n = 0$ energy starts growiing exponentially. The $n = 3$ energy remains at a relatively low magntiude before and during the relaxation.

In spite of the the lack of substantial $n = 3$ energy volumetrically, examination of the magnetic field during the relaxation event still reveals a structure aligned with the injectors analagous to HIT-SI. Figure 4.21 shows the vertical magnetic field B_Z across each injector cycle from 17 μsec to 100 μsec, covering the relaxation process (in steps of approximately 17 μsec corresponding to the injector period at 60 kHz) at the $n = 0$ energy becomes dominant. Before the $n = 0$ energy becomes dominant, the magnetic field structure possesses three clear maxima and two obvious minima, almost resembling the injector mouth orientation. This field quickly merges into the main $n = 0$ poloidal field of the spheromak after the $n = 0$ energy starts to become dominant around 50-60 μsec into the simulation.

The analagous formation process to HIT-SI that is seen in HIT-SI3 simulations may

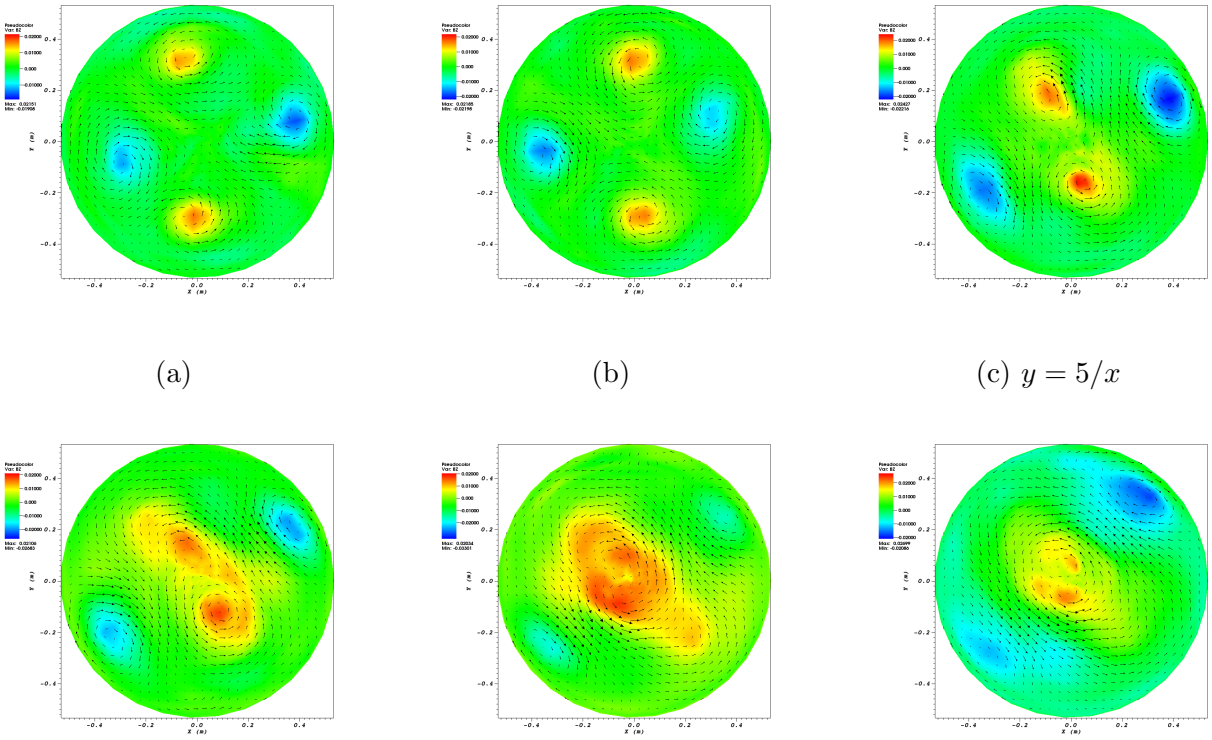

(a) (b) (c) $y = 5/x$

(d) (e) $y = 3sinx$ (f)

Figure 4.19: Heat map of the vertical magnetic field B_Z during the formation period of 68.5 kHz HIT-SI in NIMROD, displaying a $n = 2$ shaped structure initially aligned with the injector mouths.

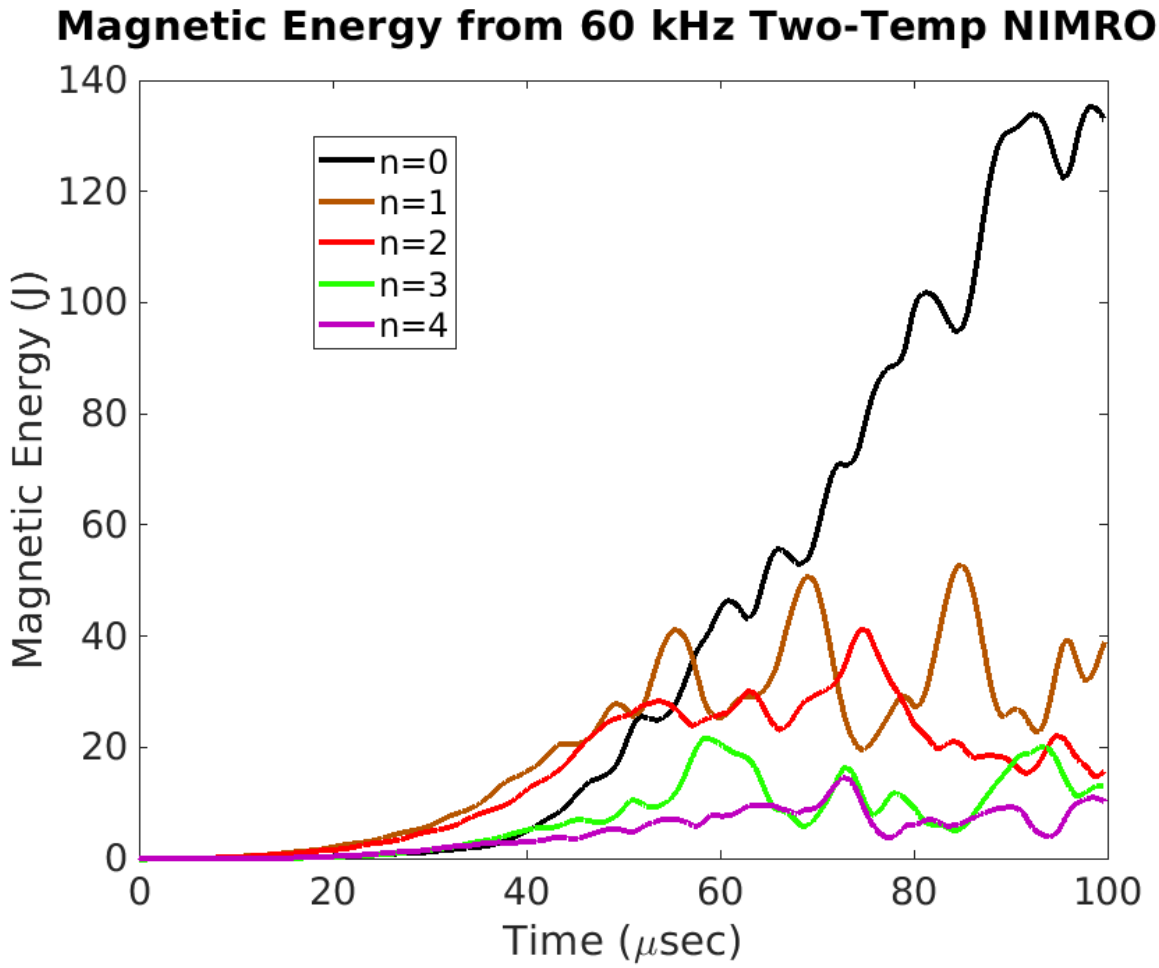

Figure 4.20: The volume-integrated energy of the first five Fourier modes from the two-temperature 60 kHz NIMROD simulation of HIT-SI3, displaying about equal $n = 1$ and $n = 2$ energy, with relatively little $n = 3$ and $n = 4$, before relaxation and the growth of the $n = 0$ energy.

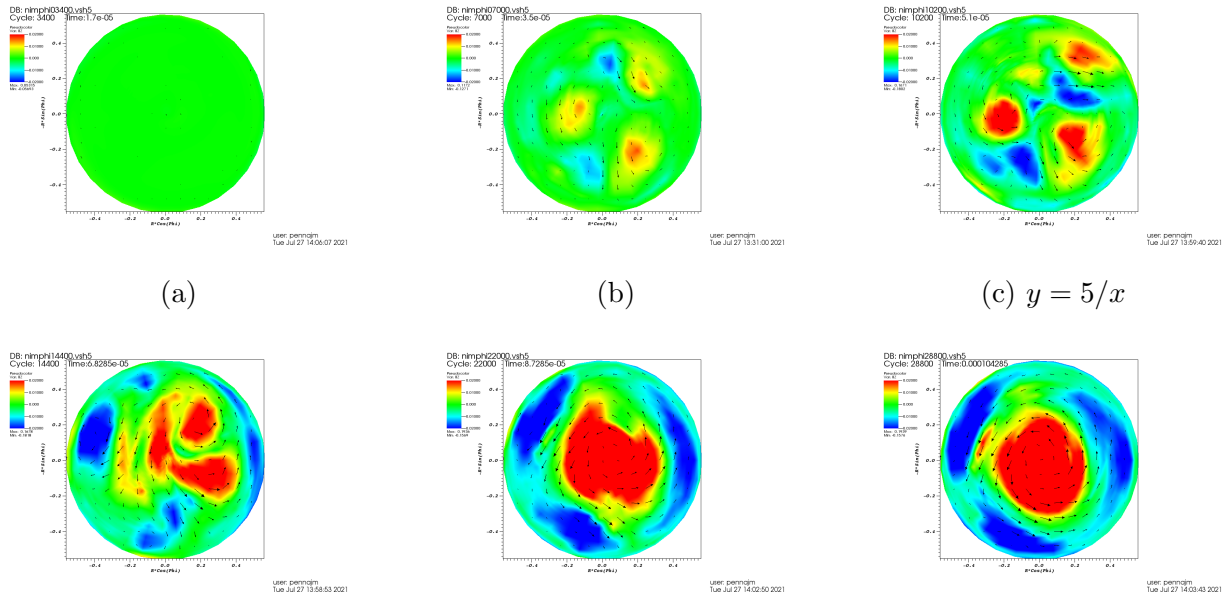

(a) (b) (c) $y = 5/x$

(d) (e) $y = 3sinx$ (f)

Figure 4.21: Heat map of B_Z in HIT-SI3 from the two-temperature NIMROD simulation, displaying the first six or so injector cycles during the spheromak formation and relaxation process. Despite the lack of $n = 3$ energy, a shape vaguely reminiscent of the injectors is present before relaxation.

end up proving a feature of high-frequency spheromaks that could be taken advantage of in future devices, perhaps for higher efficiency startup as higher injector frequencies have higher current gains. The lack of corresponding $n = 3$ energy matching the injector structure, as an analog to the $n = 2$ energy from the two injector HIT-SI; this partially goes to show that the spectrum is still being primarily influenced by what is imposed by the injectors and the plasma response. How well the formation may end up describing the actual activity in the experiment is another matter, and the next section will focus on establishing the degree of agreement between experiment and simulation.

4.6 Comparison of Simulation to Experiment

One of the goals of this frequency scan is to determine if any observed trends from the simulation data can be applied to explain experimental trends. This inevitably involved the comparison of quantities measured in experiment to data from sythetic diagnostics sampling NIMROD simulations. Unfortunately, due to the the vast range of parameters that make every experimental shot on HIT-SI3 unique, direct comparison is nearly impossible, or meaningless. However, one quantity that has been used as a fairly reliable metric for comparison is the current centroid location as measured by the surface probes. This derived quantity is useful because it can be applied even to zero-β simulations. Historically, poor disagreement between the simulated centroid position and the experimentally measured position makes this diagnostic a prime target for examination. In addition, the newly installed multichord interferometer allows the examination and comparison of density from radial several locations in the experiment, and provides another diagnostic for comparison with the evolved-density simulations. Similarities in the simulated traces to the experimental density traces could indicate simular dynamics driving the flow and plasma pressure evolution.

4.6.1 Current centroid comparison

The HIT-SI3 shot 210616015 was a negative current spheromak taken during the high power Spring 2021 campaign at f_{inj} =16.4 kHz, which displayed similar toroidal current

evolution and magntiude to the NIMROD simulations (see Figure 4.22). With the single and two-temperature NIMROD simulations resembling this shot, it was suitable to use the current centroid data from the experimental shot for comparison agains the three 15 kHz simulations. The radial and vertical positions of the current centroid from shot 210616015 and the three 15 kHz NIMROD simulations of HIT-SI3, calculated according to the formula in Equation 3.5, are plotted in Figure 4.23. The solid lines represent the calculated average position, whereas the shaded regions around each line represent the standard deviation of the position. The radial position of the zero-β simulation suffers from the worst agreement, being a full centimeter away from the experiment position chosen for comparison. The single-temperature simulation begins approaching the same position, and the two-temperature centroid is only a few millimeters from the experimentally measured position.The convergence between the two-temperature simulation's radial position and the experimental shot after the initial activity is interesting, as such close agreement has not yet been observed in the radial position. Indeed, it appears that as terms are added to more accurate replicate the plasma physics in the spheromak (going from constant temperature and density to evolving temperature and density, to separating the evolution of electron and ion density), the agreement in radial position gets better. The vertical position, shown in the bottom plot of Figure 4.23, shows worse agreement compared to the simulations, with the characteristic downard displacement of the spheromak much less pronounced in all simulations than in experiment.

The 58.5 kHz shot 180821015 was chosen for comparison to the 60 kHz NIMROD simulations, however the toroidal currents are not comparable (about 20 kA average peak value in the experiment vs 60 kA in the simulations), and this is due to the difference in injector power. The higher injector frequencies could not be run at the same high powers used in the low frequency of the campign due to the higher impedance that those frequencies, but in the simulation this is not an issue. The comparison therefore cannot be exact, however the phasing, frequency, and toroidal current sign still indicate some similar dynamics. The radial and vertical current centroid positions of the three 60kHz simulations and shot 180821015 are plotted in Figure 4.24. The radial position of the experimental shot appears to be over

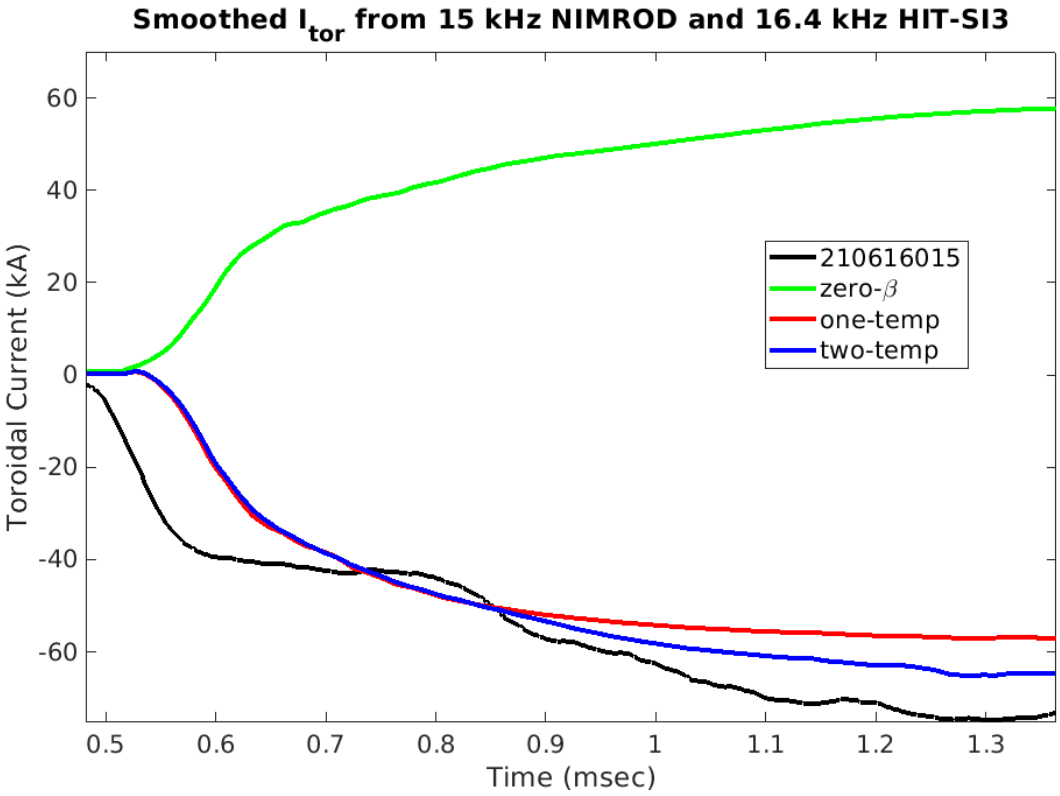

Figure 4.22: Plot of the relative (including current sign relative to the injectors) toroidal current from 15 kHz NIMROD simulations in zero-β, single, and two-temperature, compared to shot 210616015.

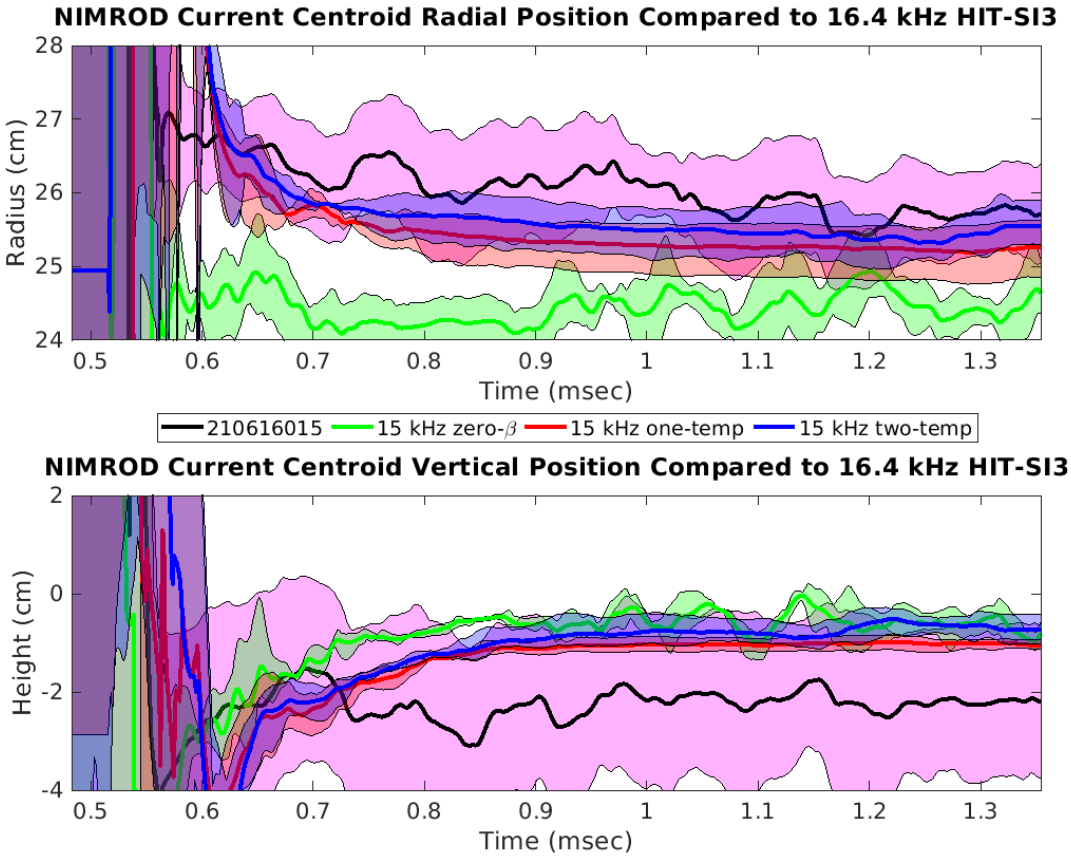

Figure 4.23: Current centroid radial (top plot) and vertical position (bottom) from all three 15 kHz NIMROD simulations compared to 16.4 kHz HIT-SI3 shot 210616015. Lightly shaded-in areas represent the standard deviation of the plotted average position.

a centimeter farther out from even the two-temperature simulation centroid radius. This is in stark constrast to the low frequency simulation, which saw better and even converging agreement in the radial position. Looking at the vertical position, the opposite situation from the low frequency comparison is once again observed, with the vertical position of the experimental centroid in near agreement with the zero-β and single-temperature high frequency simulations, and the two-temperature simulation only disagreeing by tens of millimeters. Despite the disparity in injector power and toroidal current magnitude between simulation and experiment, the NIMROD-generated centroid seems to be nearly experimentally accurate. As noted above, there is also a chance that this merely indicates the injector force on the spheromak is underestimated by NIMROD, and that the injector dynamics must be examined to ensure the proper force is being applied compared to the experiment.

4.6.2 Comparison of Chord-Averaged Densities

During the Spring of 2021, a four-chord, two-color interferometer was brought online by A. Hossack and the HIT team, and measurements using all four chords were taken on some of the last experimental shots. Though the density measured from each chord is line-averaged, like the previously mentioned FIR, the use of four chords at varying impact parameters across the radius of the flux conserver offers the opportunity to get a sense of the radial density variation over time in future experiments. Due to the disparity in the magnitude of the NIMROD simulation density and the experimental densities during this campaign ($3 \times 10^{19} m^{-3}$ vs $\approx 2 \times 10^{20}$), the choice was made to use a "normalized" density, dividing the experimental trace by the maximum value of the density as found during that time period. These normalized densities from experiment and the finite-β 15 kHz simulations are displayed for all four chords in Figure 4.25. The anomolous drop to zero in chord 4 from experiment is from the densisty during that interval being measured as negaitve due to equipment malfunction. The overall behvaior of the line-averaged experimental densities is fairly different from the simulation-derived quantites. In both the single and two-temperature simulations, the densities along each chord show fairly uniform magnitude, without regular

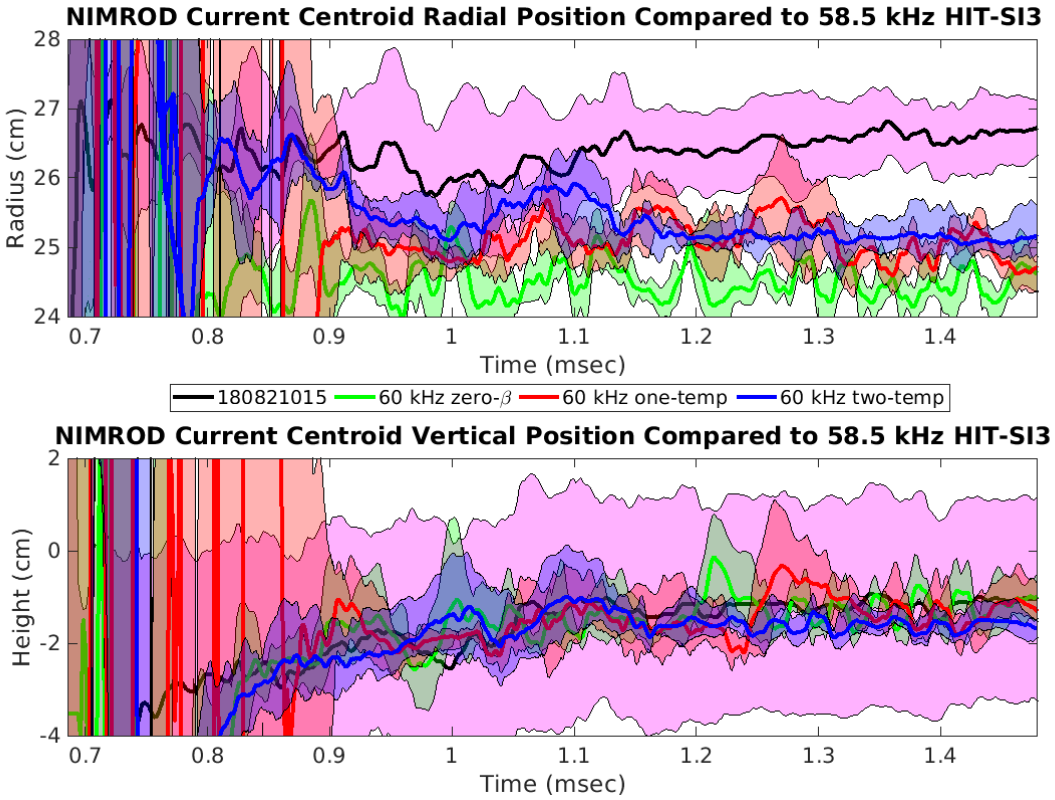

Figure 4.24: Current centroid radial (top) and vertical position (bottom) from all three 60 kHz NIMROD simulations compared to 58.5 kHz HIT-SI3 shot 180821015, a positive current shot of simular gain.

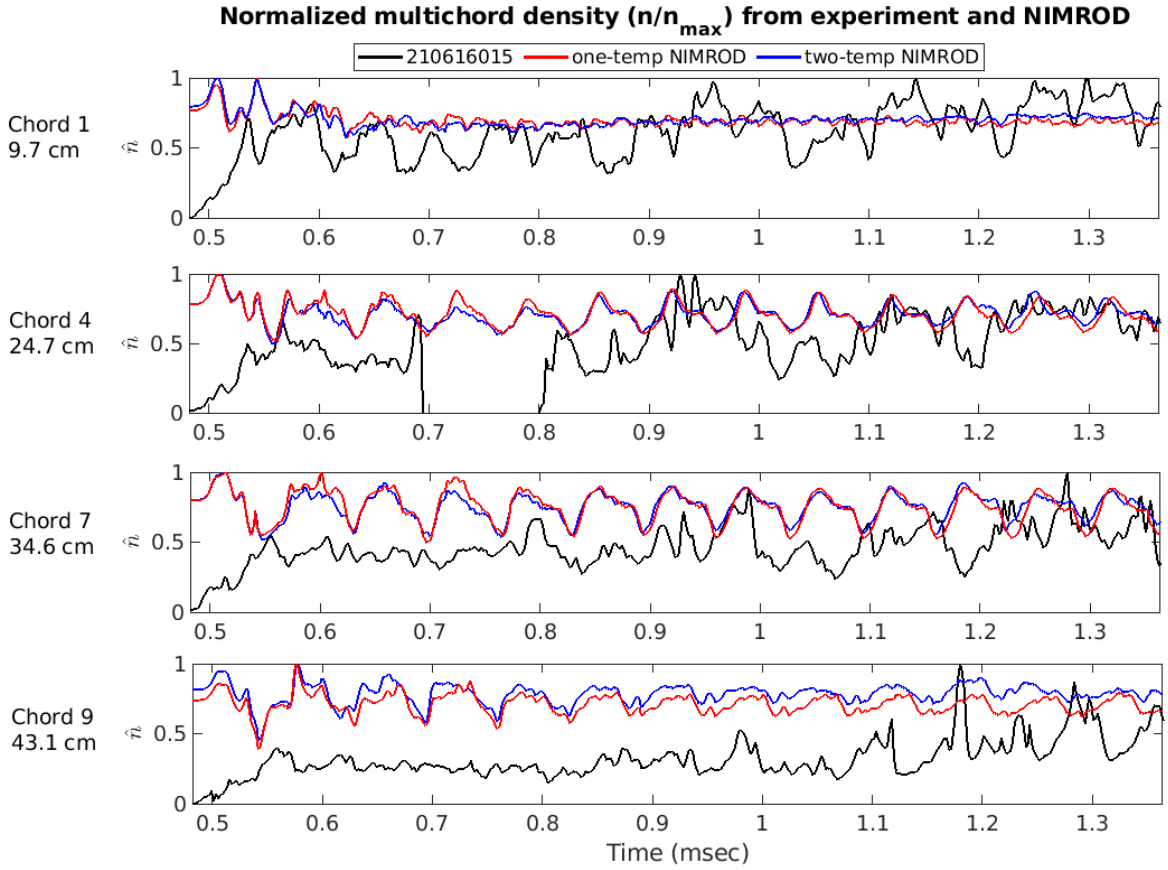

Figure 4.25: The experimentally measured line-averaged density from each of the four chords in the multichord interferometer from HIT-SI3 shot 210616015 and from single and two-temperature NIMROD.

changes, and display a visible injector-frequency oscillation. The injector frequency is largely obscured by random fluctuations in the experimental traces, with the exception of the chord 1 trace close to the inboard edge of the spheromak.

4.7 Comments on Limitations of Simulations

4.7.1 Density evolution and artificial diffusivity

An inescapable flaw of the fluid model used in NIMROD, or any computational model used for HIT-SI and HIT-SI3 so far, is the reliance on artificial diffusivity within the continuity equation to prevent the growth of instabilities which might occur during the numerical advance. In addition to the artificial diffusivity, as mentioned before there is a "hyperdiffusivity" term that allows stabilization of the density at very fine grid scales. This hyperdiffusivity is usually several orders of magnitude smaller than the artificial diffusivity but is comparable in magnitude to the square of the finest spatial grid scale used. These terms turn the density continuity equation in MHD from

$$\frac{\partial n}{\partial t} + \vec{\nabla} \cdot (n\vec{V}) = 0 \tag{4.5}$$

to

$$\frac{\partial n}{\partial t} + \vec{\nabla}\dot{(}n\vec{V}) + D_n \nabla^2 n + \nabla^2 D_{hyp} \nabla^2 n = 0 \tag{4.6}$$

The choice of diffusivity is more than just a practical choice for stabilizing the computation; it can have an effect on the physical dynamics of simulations. Shot 160609009 was simulated by K. Morgan as an example of a high current gain low frequency shot (for the experimental campaign at the time). Figure4.26 shows synthetic FIR traces for three simulations of this shot, one done using diffusivity of 1000 m^2/s and the other two using $D = 50m^2/s$. Large (varying by a factor of 50-100%, especially in low-frequency discharges) oscillations in the magnitude of the FIR-measured density are a characteristic of experimental measurements and were not initially captured in the earliest, high-diffusivity simulations of HIT-SI3. The later runs performed by the author using a much lower diffusivity, in constrast, show these large oscillations and more accurately resemble the measured experimental dynamics. The physical effects of the artificial diffusivity terms appear to extend to calcu-

lated quantities such as $< \beta >$ - in Figure 4.27 there is a marked difference in the magnitude of $< \beta >$ between the $D = 1000 m^2/s$ simulation and the $D = 50^2/s$ simulation. Given the reduction in the oscillations of density seen with increased diffusivity, the increased $< \beta >$ could be a consequence of density not being advected as greatly and not being able to transfer energy via loss terms as efficiently. It is therefore with care that the diffusivity value must be set, since a needlessly high value can affect the experimental dynamics; it is in the best interest of physically accuracy to set the diffusivity and hyperdiffusivity as low as possible. However, in some simulations, in particular high frequency simulations, setting values for diffusivity comparable in value to the viscosity (50-200 m^2/s) can result in the simulations crashing. This is also true with hyperdiffusivity, as it has been necessary in some simulations using high f_{inj} to increase the hyperdiffusivity during startup periods, to the maximum value appropriate for the grid scale being used.

Luckily, there is evidence that there is a limit to how low the diffusivity can be set before there are diminishing returns in the density dynamics. The simulations of high-frequency shot 180816020 presented in the previous chapter were run using two diffusivity values, $D = 250\ m^2/s$ and $D = 150\ m^2/s$. Figure 4.28 shows the synthetic FIR traces from these simulations in single-temperature NIMROD compared to the experimental FIR trace from shot 180904015. Though the higher diffusivity simulation exhibits some differences. the magnitude of the oscillations of the simulations and experiment are roughly the same. Therefore, the diffusivity should be set as low as possible for accuracy compared to the experimental dynamics, but still not so low that the simulation becomes numerically unstable. While results similar to experimental data can be obtain from simulation with careful choice of numerical parameters, it must not be forgotten that on some level, these artificial terms do have some effect that prevent true fidelity with experimental data from ever being achieved.

4.7.2 Centroid dynamics and heating

Another area of persistent disagreement between simulation and experiment is the position of the current centroid as measued by the surface probe. As covered previously, the

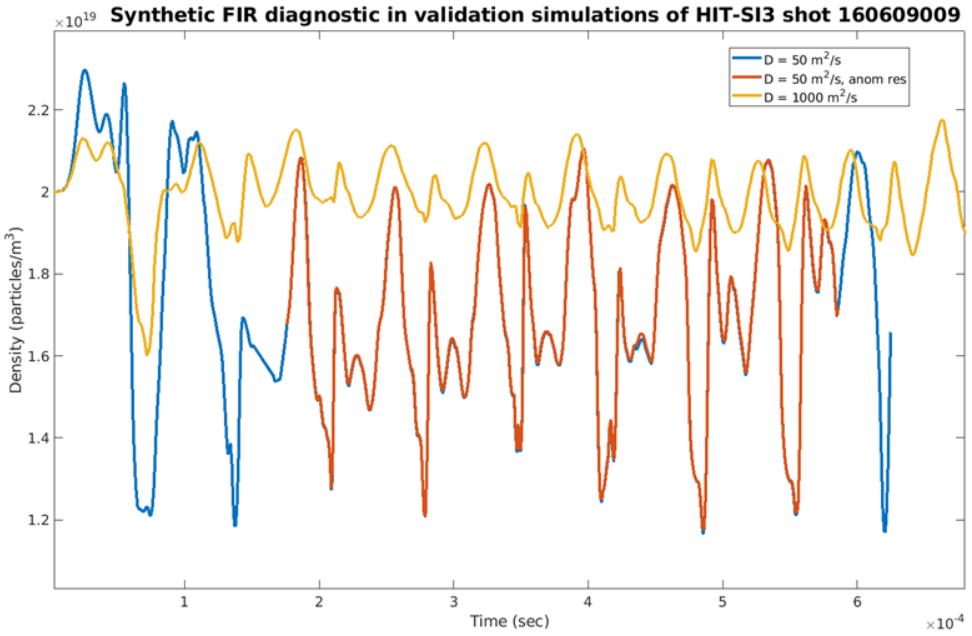

Figure 4.26: A plot of the synthetic FIR-measured density from one $D = 1000m^2/s$ (yellow) and two $D = 50m^2/s$ (blue, orange) NIMROD simulations of 14.5 kHz NIMROD shot 160609009.

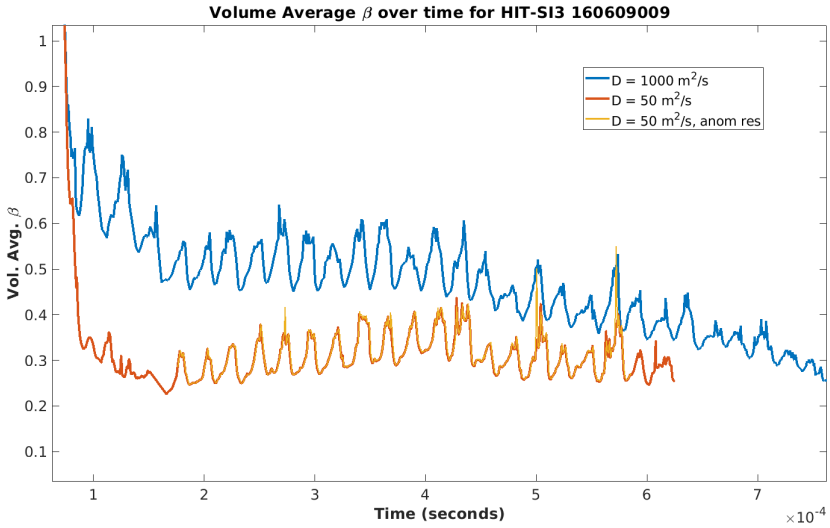

Figure 4.27: A plot of volume-averaged $\beta = \frac{2\mu_o<P>}{<B^2>}$ one $D = 1000\ m^2/s$ (bluee) and two $D = 50\ m^2/s$ (orange,yellow) NIMROD simulations of 14.5 kHz NIMROD shot 160609009.

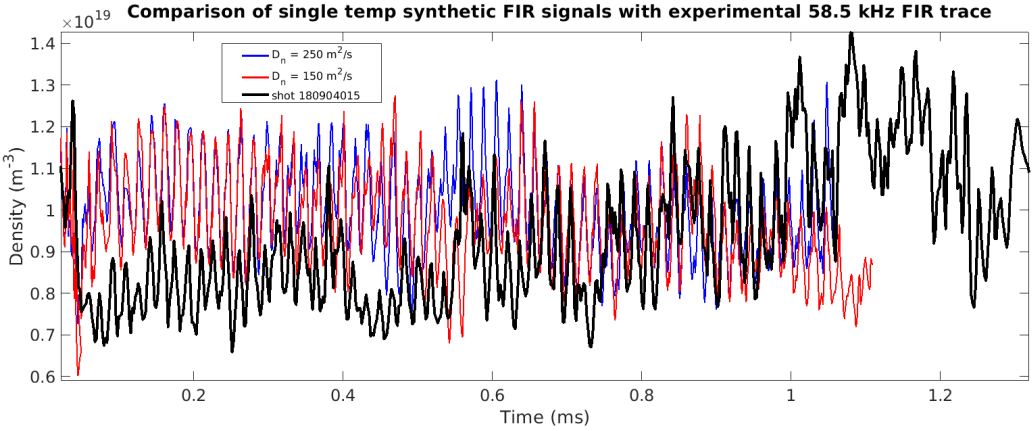

Figure 4.28: The FIR-measured density from HIT-SI3 shot 180904015 compared to the synthetic FIR measurements from single-temperature NIMROD simulations performed with diffusivity values of $D = 150\ m^2/s$ (red) and $D = 250\ m^2/s$ (blue).

centroid is the weighted-average between all of the surface probes to give the radius and vertical position of the center of the signals. In the Chapter 3, Figure 3.34 displays a good example of the disagreement between experiment and simulation, in particular the fact that the experimental centroid radius and vertical position are substantially higher than what is captured in the simulation. The first impression given is that the simulations are missing some dynamics that increase the plasma pressure in the experiment and cause the spheromaks to push out more substantially against the $J \times B$ force imposed by the injectors. What these dynamics could be, however, is not immediately clear. There is some thought that heat conduction could be improperly modeled; a rather pessimistic model is currently used, in which the parallel heat conduction is set using the more pessimistic ion mass, and the perpendicular heat conduction is set using the electron. Running simulations with adjusted heat conduction could result in more heating, greater plasma pressure, and more accurate centroid, but studies done by K. Morgan suggest the value of the heat conduction constants my not matter within an order of magnitude or so. More optimistic is the explanation that the confinement is better than what is predicted by simulation, and that long, organized magnetic field lines are able to confine plasma for long enough for it to heat.

4.8 Conclusion

The scan across injector frequencies in NIMROD simulations of HIT-SI3 has yielded several interesting results. Quantities calculated using spheromak currents alone such as current gain and current centroid motion suggest significant differences not only across frequencies but in different physical models. In particular, the two-temperature simulations seem to stabilize the movement in radial position and minimize the fluctuations in $n = 2$ energy. Important trends, such as β and injector impedance with increasing f_{inj}, and behavior such as the shape of the magnetic field during formation, from HIT-SI have been replicated in HIT-SI3 simulations. While these simulations do disagree with experiment in sometimes significant ways, evidence of increasing agreement with experiment when using a more physically-realistic model gives a possible route for more accurate simulations. For

now, the frequency scan provides an important data set along with experimental studies that will allow several generalizations of HIT-SI3 to be made in the next and final Chapter.

Chapter 5

CONCLUSIONS AND FUTURE WORK DISCUSSION

5.1 Conclusions

The overall conclusion of this work is that the evolution of HIT-SI3 spheromaks is primarily influenced by the injector frequency (with significant influence from choice of phasing as well) and that differences in helicity injector parameters are the primary driver in steady-state properties. This is a new and significant contribution to previous work as not only the first exhaustive study done detailing the variation in spheromak properties with frequency in HIT-SI3, but also as a study which compared trends in injector frequency between HIT devices (HIT-SI and HIT-SI3) that could result in useful knowledge for operation of future HIT experiments. The conclusions of this thesis not only include the results from the various studies done on experimental and simulation data, but also implications for how NIMROD itself should be used and impoved as well as implications for sustaining and controlling spheromaks driven using SIHI injectors based on the common trends between HIT-SI and HIT-SI3.

5.1.1 Discussion of results

The experimental data reviewed from HIT-SI3 qualified and quantified important differences between low and high injector frequency, one of the most pertinent being the disparate amounts of plasma-generated $n = 2$ fields unveiled by BD subtraction. This could indicate the presence of a major instability growing and diminishing in high frequency, and while there is some evidence such as fluctuations in the FIR-measured density, this still remains speculative. The primary reason for the is the lack of diagnostic access that would allow the shape of the core spheromak fields and density profile to be determined; without these

measurement the shape and true properties of this activity cannot be determined. Fitting with the PSI-Tri equilibrium software was inconclusive, as any results indicative of such instabilities such as increasing β or fluctuating core λ are mitigated by the poor quality of the reconstructed fields. Still, simulations of experimental shots in NIMROD indicate that the $n = 2$ is a persistent, real feature of shots and is associated with some sort of density and λ profile variation. This topic is highly recommended as a topic for future research.

Extending the NIMROD study of HIT-SI3 to a set of simulations at a variety of frequencies using three different physical models yielded several important results. Referring back to the previously mentioned differences between low and high frequency HIT-SI3 experimental shots, the frequency scan simulations established a possible transition zone from low to high in the vicinity of 30-45 kHz, which is physically meaningful when the injector period is compared to the toroidal transit time of the Alfvén velocity. This is manifested in several quantities derived from synthetic diagnostics, such as current centroid radial position and plasma-generated $n = 2$ activity. One of the most important results is the discovery that the trends with injector frequency seen in HIT-SI were often repeated in HIT-SI3, in particular the increases in current gain, β, and injector impedance seen with increasing injector frequency. The formation dynamics show some similarity to high-frequency HIT-SI, though it is not immediately obvious whether this is a coincidence or some new feature of spheromaks formed at SIHI frequencies with periods close to the Alfvén transit time. The better agreement between experiment and simulations using a two-temperature MHD model compared to the standard single-temperature model may indicate that, physically, electron heating plays an important role in the experimentally observed behavior. Between the PSI-Tri fitting software and the NIMROD results, it is apparent that capturing the behavior of HIT-SI3 in numerical calculations is almost impossible to do exactly, so all results from simulation must be interepreted through the lens of being approximations, not reproductions. Some of the considerations that must be taken when using software models themselves are important as results, as will be discussed next section.

5.1.2 Implications for simulating HIT devices

The radial position of the current centroid measured from experiment has been used as a metric for comparison to simulations, and the discrepancy between the simulation-derived centroid radius and experiment has been a long-standing area of disagreement. The presented results from Chapters 3 and 4, such as Figure 3.34 and Figure 4.23, suggest that this disagreement is minimized when using the two-temperature finite-β MHD model as the centroid radii experience the greatest outward shift compared to zero-β or single-temperature. The exact cause of this mechanism is not known and should be thesisined in future NIMROD simulations, but nonetheless it is a consistent feature. This may suggest, that when time and resources are available, that NIMROD's two-temperature MHD model be used to simulate HIT devices in finite-β when a numerical model for comparison to experiment is required. Minimizing the density diffusivity (as low as possible before the density advance becomes destabilized) is another important factor in improving agreement between the density dynamics observed in experimented vs those sampled from simulations. While it is not necessarily the goal of MHD software to accurately replicate the dynamics of a given experiment, having better agreement between simulation and experiment will enable greater insight into physical causes of experimentally observed phenomena.

5.1.3 Implications for running HIT devices

The results regarding frequency and plasma-generated $n = 2$ activity manifest to sufficient degree in experiment in both HIT-SI and HIT-SI3 that it's worthwhile to make a brief statement regarding experimental operation, especially considering the up and coming HIT-SIU experiment (discussed further below). The frequency dependence observed in HIT-SI and HIT-SI3 of many of experimentally important quantities, such as viscous heating power, injector impedance, and others discussed previously, offers a potential "knob" for device operators to vary in current and future HIT devices. The potential advantages of running at high frequency (increased heating from viscous ion motion, increased toroidal

current for similar injector current, high β and therefore fusion power) may be outweighed if pressure-driven $n = 2$ instabilities are excited. The absence of these instabilities and reduced centroid motion at low frequency would make that range desirable for different reasons. The investigation of the $n = 2$ activity along with the simulation of future devices should be among some of the most important topics of future research.

5.2 Suggested Future Work

5.2.1 Further analysis of the $n = 2$ activity

The presence of the $n = 2$ activity unassociated with the spheromak equilibrium or the injectors could be indicative of instabilities associated with pressure crashes, as noted in Woodruff et al., and an in-depth study of the connection between this mode and experimental pressure would be needed to determine if this is the case in HIT-SI3. This work could and should be started with existing experimental data; in particular the Ion Doppler Spectroscopy (IDS) diagnostic that was used to measure ion velocity. Measurements from this diagnostic were considered for use in studying the spatial variation of the ions as $n = 2$ events were occurring, however the time resolution of the measurements was too poor for practical use at high frequency, and the diagnostic was not revisited between the time of discovering intermittent $n = 2$ activity in low-frequency HIT-SI3 and the conclusion of this work. A more experienced operator of the diagnostic would be most capable of reviewing and interpreting this data correctly. The 3D emission tomography system that was employed on HIT-SI3 between 2018 and 2019 is another such diagnostic, and with appropriate expertise behind analyzing the data, the emission signals could be translated into some sort of profile that sheds light on the activity.

Numerical studies would also be a part of this effort, as they were a part of this work. In particular, the use of the PSI-Tri equilibrium fitting code, or some other fitting code, should be revisited. MHD stability studies such as those done by Gautier and Jardin, but using experimental data and PSI-Tri would make it clear if a β limit were being reached and

pressure-driven instabilities were being induced. A way to incorporate more complicated flux profile functional forms might help generate fits with fields that can match the subtle spatial variation seen in the experimental IMP measurements. The accuracy of these fits, however, would still be impeded by the force of the injectors that is applied from the top of the spheromak, tending to cause a downward vertical displacement a few centimeters from the midplane. A method of accounting for this displacement must be implemented in any equilibrium fitting attempt before the results can be used to make statements about the experiment.

5.2.2 Extended simulations of HIT-SI3

NIMROD or a similar MHD simulation software must be used to simulate the advance through time, and as mentioned above a two-temperature model is recommended if improved agreement with a particular experiment is sought. A feature which could yield improved agreement is the inclusion of neutral gas dynamics, which are important at the electron plasma temperatures estimated and purported to be measured in HIT-SI3 by C. Everson in [33] and the neutral fractions measured in HIT-SI (and by extension HIT-SI3).[22] Adding neutral gas evolution to MHD models was performed in the past by D. Sutherland [45] in the PSI-Tet 3D MHD software and is being finalized by S. Taheri in the NIMROD software, working under U. Shumlak. Performing simulations incorporating neutrals and comparing the results to experiment, zero-β, single-temperature, and two-temperature simulations will not only shed light on the role of neutrals in HIT plasmas; it would provide an additional tool in simulations for greater fidelity with the physical world, which will be increasingly important as new HIT devices are built and simulations are performed.

5.2.3 Simulations of Next-Generation HIT Devices Employing Manifolds

At the time of writing, the HIT lab at the University of Washington has shut down the HIT-SI3 experiment and is focused on assembling the next generation HIT device, HIT-SIU (Helicity Injected Torus - Steady Inductive Upgrade). This device will employ an injector

manifold with four mouths opening into the flux conserver volume from the top, where there HIT-SI3 injectors are currently located. Simulations of this device have already been performed before its operation, already providing preliminary results.[4] However, as HIT-SIU is operated and phenomena are inevitably discovered that need explanation, new simulations incorporating more physical aspects like electron temperature and neutrals will be needed to formulate explanations when diagnostic data is not sufficient or available.

The end goal of this projected simulation work, and the work of the HIT program, is to generate larger and larger stably-sustained spheromaks until one capable of sustaining fusion conditions is designed, built, and operated to generate clean energy for the entire world.[23]

BIBLIOGRAPHY

[1] C. Akcay. *Extended Magnetohydrodynamic Simulations of the Helicity Injected Torus (HIT-SI) Spheromak Experiment with the NIMROD Code*. University of Washington, 2013.

[2] H. Alfven. Existence of electromagnetic-hydrodynamic waves. *Nature*, 150, 1942.

[3] P. M. Bellan. *Magnetic Helicity, Spheromaks, Solar Corona loops, and Astrophysical Jets*. World Scientific, 2018.

[4] T. Benedett. *Effects of Nonaxisymmetry in Equilibria and MHD Evolution of Spheromaks*. University of Washington, 2020.

[5] A.H. Boozer. Ohm's law for mean magnetic fields. *Journal of Plasma Physics*, 35, 1986.

[6] S.I. Braginskii. Transport processes in a plasma. *Reviews of Plasma Physics*, 1, 1964.

[7] D.P. Brennan. Nonlinear simulations of elms with nimrod. In *Proceedings of the 46th Annual APS Division of Plasma Physics Meeting*. nimrodteam.org, 2004.

[8] T.G. Cowling. The magnetic field of sunspots. *Monthly Notices of the Royal Astronomical Society*, 94, 1934.

[9] A. Kaptanoglu et. al. Two-temperature effects in hall-mhd simulations of the hit-si experiment. *Physics of Plasmas*, 2020.

[10] A.C. Hossack et. al. Plasma response to sustainment with imposed-dynamo current drive in hit-si and hit-si3. *Nuclear Fusion*, 52, 2012.

[11] A.C. Hossack et al. Derivation of dynamo current drive in a closed-current volume and stable current sustainment in the hit-si experiment. *Physics of Plasmas*, 24, 2017.

[12] A.C. Hossack et. al. Overview of the hit-si3 spheromak experiment. *APS Division of Plasma Physics Meeting*, 2017.

[13] B.S. Victor et. al. Sustained spheromaks with ideal $n = 1$ kink stability and pressure confinement. *Physics of Plasmas*, 21, 2014.

[14] B.S. Victor et. al. Development of validation metrics using biorthogonal decomposition for the comparison of magnetic field measurements. *Plasma Physics and Controlled Fusion*, 57, 2015.

[15] C. Akcay et. al. Validation of single-fluid and two-fluid magnetohydrodynamic models of the helicity injected torus spheromak experiment with the nimrod code. *Physics of Plasmas*, 20, 2013.

[16] C. Hansen et. al. Equilibrium reconstruction with 3d eddy currents in the lithium tokamak experiment. *Plasma Physics and Controlled Fusion*, 57, 2015.

[17] C. Hansen et. al. Simulation of injector dynamics during steady inductive helicity injection current drive in the hit-si experiment. *Physics of Plasmas*, 22, 2015.

[18] C. Mercier et. al. A necessary condition for hydromagnetic stability of plasma with axial symmetry. *Nuclear Fusion*, 1, 1960.

[19] C.E. Kessel et. al. The aries advanced and conservative toamak (act) power plant study. *Princeton PLasma Physics Laboratory*, 2014.

[20] C.J. Everson et. al. Fir interferometry and thomson scattering on hit-si3. *Exploratory Plasma and Fusion Research Workshop*, 2017.

[21] C.R. Sovinec et. al. Nonlinear magnetohydrodynamics with high-order finite elements. *Journal of Computational Physics*, 195, 2004.

[22] D. Elliot et. al. Two-photon lif on the hit-si3 experiment: Absolute density and temperature measurements of deuterium neutrals. *Review of Scientific Instruments*, 2016.

[23] D.A. Sutherland et. al. The dynomak: An advanced spheromak reactor concept with imposed-dynamo current drive and next-generation nuclear power technologies. *Fusion Engineering and Design*, 89, 2014.

[24] E.B. Hooper et. al. Sustained spheromak physics experiment (sspx): design and physics results. *Plasma Physics and Controlled Fusion*, 54, 2012.

[25] K.D. Morgan et. al. Validation of extended magnetohydrodynamic simulations of the hit-si3 experiment using the nimrod code. *Physics of Plasmas*, 24, 2017.

[26] M.N. Bussac et. al. Low-aspect-ratio limit of the toroidal reactor: the spheromak. *International Conference on IAEA Plasma Physics and Controlled Nuclear Fusion Research*, 7, 1978.

[27] P. Gautier et. al. Numerical study of the ideal-mhd stability limits in oblate spheromaks. *Nuclear Fusion*, 21, 1981.

[28] S. Woodruff et. al. Observation of a pressure limit in a gun-driven spheromak. *Physics of Plasmas*, 13, 2006.

[29] S.C. Jardin et. al. Ideal magnetohydrodynamic staabilit of the spheromak configuration. *Nuclear Fusion*, 22, 1982.

[30] T.R. Jarboe et al. Spheromak formation by steady inductive helicity injection. *Physical Review Letters*, 97, 2006.

[31] T.R. Jarboe et. al. Imposed-dynamo current drive. *Nuclear Fusion*, 52, 2012.

[32] T.R. Jarboe et al. A mechanism for the dynamo terms to sustain closed-flux current, including helicity balance, by driving current which crosses the magnetic field. *Physics of Plasmas*, 22, 2015.

[33] C. Everson. *Experimental assessment of confinement and heating on the HIT-SI3 spheromak*. University of Washington, 2020.

[34] J. Freidberg. *Plasma Physics and Fusion Energy*. Cambridge University Press, 2007.

[35] J. Freidberg. *Ideal MHD*. Cambridge University Press, 2014.

[36] H. Grad and H. Rubin. Hydromagnetic equilibria and force-free fields. *Proceedings of the 2nd UN Conf. on the Peaceful Uses of Atomic Energy*, 31, 1958.

[37] C. Hansen. *MHD Modeling in Complex 3D Geometries: Towards Predictive Simulation of SIHI Current Drive*. University of Washington, 2014.

[38] E.B. Hooper. Physics issues of a spheromak refluxing scenario. *Plasma Physics and Controlled Fusion*, 53, 2011.

[39] V. Izzo. *Three-dimensional Magnetohydrodynamics simulations of the HIT-SI spheromak experiment*. University of Washington, 2004.

[40] T.R. Jarboe. Review of spheromak research. *Plasma Physics and Controlled Fusion*, 36, 1994.

[41] N. Kutz. *Data Driven Modeling and Scientific Computation*. Oxford University Press, 2013.

[42] K. D. Morgan. *Finite-beta simulations of HIT-SI and HIT-SI3 using the NIMROD code.* University of Washington, 2018.

[43] J.B. O'Bryan and C.R. Sovenic. Simulated flux-rope evolution during non-inductive startup in pegasus. *Plasma Physics and Controlled Fusion*, 56, 2014.

[44] V.D. Shafranov. Plasma equilibrium in a magnetic field. *Reviews of Plasma Physics*, 2, 1966.

[45] D. Sutherland. *Measurements of neutral particles and simulations of plasma-neutral dynamics in the HIT-SI3 experiment.* University of Washington, 2019.

[46] J.B. Taylor. Relaxation and magnetic reconnection in plasmas. *Reviews of Modern Physics*, 58, 1986.

[47] B.S. Victor. *Effects of density control on internal plasma dynamics and current drive in HIT-SI.* University of Washington, 2012.

[48] L. Woltjer. A theroem on force-free magnetic fields. *Proceedings of the National Academy of Sciences of the USA*, 1958.

[49] J. Wrobel. *A Study of HIT-SI Plasma Dynamics Using Surface Magnetic Field Measurements.* University of Washington, 2011.

Appendix A

INJECTOR RAMP INPUT GENERATION AND DATA FOR SHOT 180816020

A.1 Ramp file generation script

```
## Imports
import sys
import numpy as np
import matplotlib.pyplot as plt
from scipy.interpolate import interp1d
from scipy.optimize import leastsq
import scipy.io as sio
import os
## Constants
mu0 = np.pi*4.E-7
## Setup
pOffset = 0.              # Added phase offset for "controlling" current direction
nramp = -20               # Number of interpolation points for amplitude
nphase = 4                # Number of interpolation points for phase
noffset = 0               # Number of interpolation points for offset, currently not use
inj_freq = 58.5E3         # Injector frequency
inj_flux = 1.E-3          # Injector flux scale (used by PSI-TET 'flux_mag')
inj_curr = 1.25E-2        # Injector current scale (used by PSI-TET 'volt_mag')
phase0 = 0.               # Starting guess for injector initial phase
prefixes = ['ainj','binj','cinj']  # Injector prefix (used to read data files of form 'p
```

```
mag_start = False          # Allow finite amplitude for flux at breakdown
shot = '180816020'
exp_file = '../sp_imp_den'+shot+'.mat' # Experimental data file

#Remove the file if we intend to create it
if os.path.isfile(shot + '.ramp'):
os.remove(shot + '.ramp')

## Helper functions
# Unpack coefficients
def unpack_cofs(cofs, nramp, nphase, noffset, t, t1=None):
# Unpack and form amplitude ramp
if mag_start:
mag_tint = np.linspace(0.,t[-1],nramp)
mag_cofs = np.r_[cofs[1:nramp+1]]
else:
mag_tint = np.linspace(0.,t[-1],nramp+1)
mag_cofs = np.r_[0.,cofs[1:nramp+1]]
# Unpack and form offset ramp
if nphase == 0:
if t1 != None:
phase_tint = np.r_[0.,t1]
else:
phase_tint = np.r_[0.,t[-1]]
phase_cofs = np.r_[0.,0.]
else:
if t1 != None:
phase_tint = np.linspace(0.,t[-1],nphase)
```

```
phase_tint = np.insert(phase_tint,1,t1)
else:
phase_tint = np.linspace(0.,t[-1],nphase+1)
phase_cofs = np.r_[0.,cofs[nramp+1:nramp+nphase+2]]
# Unpack and form offset ramp
if noffset == 0:
if t1 != None:
offset_tint = np.r_[0.,t1]
else:
offset_tint = np.r_[0.,t[-1]]
offset_cofs = np.r_[0.,0.]
else:
if t1 != None:
offset_tint = np.linspace(0.,t[-1],noffset)
offset_tint = np.insert(offset_tint,1,t1)
else:
offset_tint = np.linspace(0.,t[-1],noffset+1)
offset_cofs = np.r_[0.,cofs[nramp+nphase+2:]]
# Return ramps
return mag_tint, mag_cofs, phase_tint, phase_cofs, offset_tint, offset_cofs

# Compare drive waveform to experimental data (for fitting)
def fun_comparison(cofs, inj_freq, phase0, nramp, nphase, noffset, t, y, t1=None):
# Interpolate ramps
phase0 = cofs[0]
mag_tint, mag_cofs, phase_tint, phase_cofs, offset_tint, offset_cofs = unpack_cofs(cofs,
ramp = interp1d(mag_tint, mag_cofs)
phase = interp1d(phase_tint, phase_cofs)
```

```
offset = interp1d(offset_tint, offset_cofs)
# Compute error
err = np.sin(2.*np.pi*inj_freq*t + phase0 + phase(t))*ramp(t) + offset(t) - y
return err

# Compute drive waveform (for plotting)
def fun_eval(cofs,  inj_freq, phase0, nramp, nphase, noffset, t, t1=None):
# Interpolate ramps
phase0 = cofs[0]
mag_tint, mag_cofs, phase_tint, phase_cofs, offset_tint, offset_cofs = unpack_cofs(cofs,
ramp = interp1d(mag_tint, mag_cofs)
phase = interp1d(phase_tint, phase_cofs)
offset = interp1d(offset_tint, offset_cofs)
# Compute waveform
y = np.sin(2.*np.pi*inj_freq*t + phase0 + phase(t))*ramp(t) + offset(t)
return ramp(t), phase(t)+phase0, offset(t), y

# Perform fitting
def fit_waveform(t, y, inj_freq, phase0, nramp, nphase, noffset, t1=None):
# Fit amplitude and base phase
cofs = np.r_[phase0,np.ones(nramp)]
cofs = leastsq(fun_comparison, cofs, args=(inj_freq, phase0, nramp, 0, 0, t, y, t1))
# Full fit
cofs = np.r_[cofs[0],np.zeros(nphase),np.zeros(noffset)]
cofs = leastsq(fun_comparison, cofs, args=(inj_freq, phase0, nramp, nphase, noffset, t,
# Unpack and get waveform
cofs = cofs[0]
phase0 = cofs[0]
```

```
ramp, offset, phase, ya = fun_eval(cofs, inj_freq, phase0, nramp, nphase, noffset, t, t1
mag_tint, mag_cofs, phase_tint, phase_cofs, offset_tint, offset_cofs = unpack_cofs(cofs,
phase = interp1d(phase_tint, phase_cofs)
offset = interp1d(offset_tint, offset_cofs)
if mag_start:
nsamp = nramp
else:
nsamp = nramp+1
prof = np.concatenate((mag_tint.reshape(1,nsamp), mag_cofs.reshape(1,nsamp), phase(mag_t
return phase0, prof, ya

## Run fitting
# Read in data
data = sio.loadmat(exp_file, squeeze_me=True, struct_as_record=False)
mat_int = data['int']
# Compute breakdown time
inj_curr_amp = np.maximum(abs(mat_int.iainj),abs(mat_int.ibinj),abs(mat_int.icinj))
i = np.argwhere(inj_curr_amp > 2.E3)
ts = mat_int.time[i[0]]
tBreakdown=ts[0]
t1=mat_int.time[i[-1]][0] - 1./inj_freq
# Compute default number of ramp periods (1 per cycle)
if nramp < 0:
        nramp = int((t1 - tBreakdown)*inj_freq)
print "Time window = [{0:E}, {1:E}] ({2:d})".format(tBreakdown,t1,nramp)

for prefix in prefixes:# Get desired injector waveforms
        if prefix=='ainj':
```

```
        data = np.vstack((mat_int.time,mat_int.psiainj,mat_int.iainj))
        elif prefix=='binj':
        data = np.vstack((mat_int.time,mat_int.psibinj,mat_int.ibinj))
        elif prefix=='cinj':
        data = np.vstack((mat_int.time,mat_int.psicinj,mat_int.icinj))
# Mask time window
        mask = np.logical_and(np.greater(data[0,:],tBreakdown),np.greater(t1,data[0,:]))
        t = data[0,mask]-tBreakdown
# Print info
        print "======================================================="
        print "Fitting linear ramps to injector waveform: ", prefix
        print "  INJ-Freq = {0:e}".format(inj_freq)
        print "  t0       = {0:e}".format(tBreakdown)
        print "  t1       = {0:e}".format(t1)
        print "  nRamp    = {0:e}".format(nramp)

## Compute flux waveform
        print "Computing flux fit"
        print "  Scale factor = {0:e}".format(inj_flux)
        y = data[1,mask]/inj_flux
# Perform fit
        flux_phase0, flux_ramp, ya = fit_waveform(t, y, inj_freq, phase0, nramp, nphase,
        if flux_ramp[1,-1] < 0.:
        flux_ramp[1,:] = abs(flux_ramp[1,:])
        flux_phase0 = flux_phase0 + np.pi
        print '  Phase0 = {0:e}'.format(flux_phase0)
# Plot comparison
        plt.figure(1)
```

```
        scal_fac = inj_flux*1.E3
        plt.plot(t*1E3,y*scal_fac,'r')
        plt.plot(t*1E3,ya*scal_fac,'b')
        plt.xlabel('Time [ms]')
        plt.ylabel('Injector Flux [mWb]')
        plt.grid('on')

## Compute current waveform
        mag_start = False
        print "Computing current fit"
        print "  Scale factor = {0:e}".format(inj_curr)
        y = data[2,mask]*mu0/inj_curr
# Perform fit
        curr_phase0, curr_ramp, ya = fit_waveform(t, y, inj_freq, phase0, nramp, nphase,
        if curr_ramp[1,-1] < 0.:
        curr_ramp[1,:] = abs(curr_ramp[1,:])
        curr_phase0 = curr_phase0 + np.pi
        print '  Phase0 = {0:e}'.format(curr_phase0)

## Plots
# Plot comparison
        plt.figure(2)
        scal_fac = inj_curr/(mu0*1.E3)
        plt.plot(t*1E3,y*scal_fac,'r')
        plt.plot(t*1E3,ya*scal_fac,'b')
        plt.xlabel('Time [ms]')
        plt.ylabel('Injector Current [kA]')
        plt.grid('on')
```

```
# Plot Lambda comparison
        plt.figure(3)
        lam = curr_ramp[1,:]*inj_curr/(flux_ramp[1,:]*inj_flux)
        plt.plot(curr_ramp[0,:],lam)
        plt.xlabel('Time [ms]')
        plt.ylabel('Injector Lambda [1/m]')
        plt.grid('on')


## Save injector ramps
        f = open(shot + '.ramp','a')
        if prefix=='ainj':
         f.write('{0}\n'.format(flux_ramp.shape[1]))
# Flux ramp
        f.write('# {0} Flux ramp: t, mag, phase (scale = {1})\n'.format(prefix,inj_flux)
        for vals in flux_ramp.transpose():
        f.write('{0:E} {1:E} {2:E}\n'.format(vals[0],vals[1],vals[2]+flux_phase0+pOffset
# Current ramp
        f.write('# {0} Current ramp: t, mag, phase (scale = {1})\n'.format(prefix,inj_cu
        for vals in curr_ramp.transpose():
        f.write('{0:E} {1:E} {2:E}\n'.format(vals[0],vals[1],vals[2]+curr_phase0+pOffset
        f.close()
        print "Ramps saved to '{0}.ramp'".format(shot)
# Show plots
        plt.show()
```

A.2 Waveform data for 180816020 injector flux and current

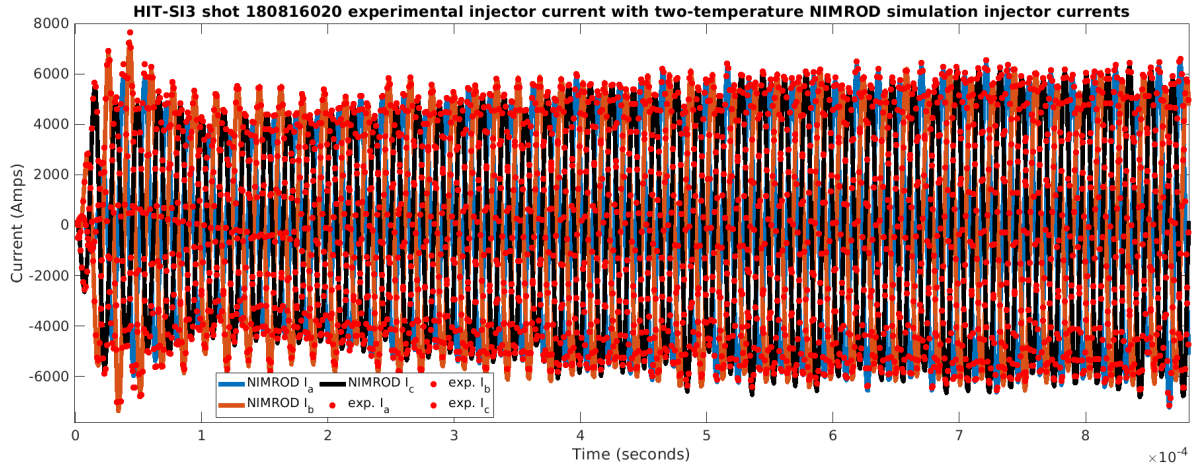

Figure A.1: Plot of the HIT-SI3 experimental injector current (red dots) sampled from the data system, with the corresponding interpolated waveform used in the NIMROD simulation. Note the over and undershoot of the waveform in NIMROD compared to the experiment at some times, which is usual for these simulations as the current is noisier.

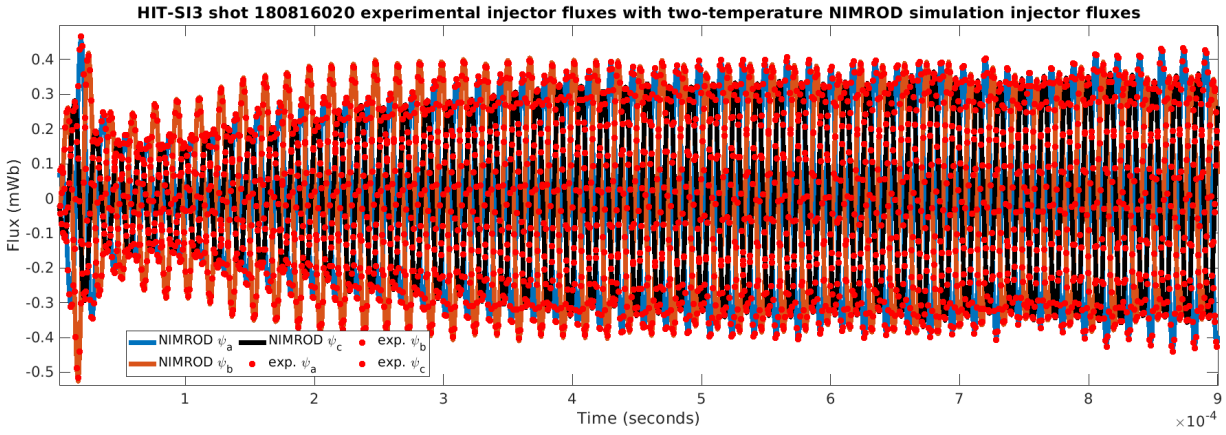

Figure A.2: Plot of the HIT-SI3 experimental injector flux (red dots) sampled from the data system, with the interpolated waveform for the flux used in the NIMROD simulation. The interpolated flux waveform fits the data to a better degree.

VITA

James Penna hold a Bachelor's Degree in Physics from the Massachusetts Institute of Technology. He has been studying plasma physics in the HIT laboratory at the University of Washington since 2015.

After graduation he can be reached via `pennajm.mit@gmail.com`. Don't expect fast responses, he'll be busy.